# Phase Diagram of the Anisotropic Heisenberg Spin Ladder

A thesis submitted for the degree of

Master of Science (MSc)

by

Tyler Hewitt

School of Physical Sciences

University of Kent

Canterbury

UK

2017

# Declaration

I declare that this thesis has been comprised solely by myself and that it has not been submitted, in whole or in part, at any other institution for any other degree. The work presented here is entirely my own and any work that has been used, that was composed by others, has been clearly referenced or acknowledged throughout this document.

# Acknowledgements

I would like to thank my supervisor Dr. Sam Carr for the endless guidance and patience he has shown me throughout this project and thesis. In addition he has taught me the fruitfulness of curiosity and that there is richness even in the smallest areas of physics. His understanding and intuition of physics always leaves me in awe.

A thank you as well to the University of Kent for allowing me to undertake this degree and the physics department for giving me the space to work.

I'd also like to thank my mom for the support she has shown me in every aspect of this journey, and constantly reminding me that one needs to balance hard work with a bit of fun. In addition I'd like to thank my cousin Craig for teaching me that if one is going to do something, do it right and do it to the best of your ability, anything less is a waste of time. I would never have attempted these studies, both this thesis and the preceding undergraduate degree, without this philosophy. And lastly to my late grandfather "Papa" who was always happy to see me home from my travels.

I would also like to thank my friends for their generosity and for keeping me sane through this endevour. And in particular the trinity $\triangle$, always there to carry each other home. I owe much gratitude to the misfits and degenerates of Kent Stags Lacrosse club for being the messiest and truest of friends, whether it was simply to play lacrosse or to blow off steam, they have been there.

# Abstract

In this thesis, we deal with 1-dimensional anisotropic spin models more specifically with the chain and ladder geometries. These models are fundamental to the study of condensed matter theory and quantum magnetism because of their simplicity. Research into the chain model dates back to 1930s with Hans Bethe. One method to study these systems is through numerical analysis including renormalization group techniques. These allow for the diagonalization of the Hamiltonian without sacrificing computation to a large virtual Hilbert space.

In this thesis, we present results for both the spin chain and spin ladder geometries in open boundary conditions. This work uses the density matrix renormalization group technique to calculate system energy. Initially we will present a study into the spin energy gap of the spin-½ anisotropic (XXZ) Heisenberg chain in open boundary conditions (OBCs). The energy gap is shown to be reduced to half in the ground sector when compared to periodic boundary conditions (PBCs) due to edge effects. Secondly, a full phase diagram for the spin-½ anisotropic Heisenberg ladder is presented which shows the emergence of a rich schematic with a variety of phases. Lastly, weak coupling limit maps are compared to quantum field theory phase transition predictions. This research was motivated by the lack of comprehensive phase diagram results for ladders and by real materials being investigated at the University of Kent.

# Contents

# Chapter 1

# Introduction

Low dimensional magnetism has become an increasingly popular area of research in both the theoretical and experimental disciplines. Quantum spin systems provide good models to study the fundamental aspects of magnetic materials. These 'spins' are particle-like magnets that are localized to lattice points and interact with each other via quantum mechanics. Spin systems often provide good demonstrations of quantum phases and the transitions between them. By studying the properties of these systems we find deeper understandings of the mechanisms of nature.

Spin ladder geometries are an interesting model to study because they act as a crossover between the limits of a true 1-dimensional chain and a 2-dimensional plane. The anisotropic Heisenberg ladder provides a rich area of research that is becoming of greater interest due to the novel results from experiments and theories probing these low-dimensional systems and materials.

### Outline

This thesis aims to enlighten the reader to the properties of spin-½ systems in the form of Heisenberg chains and 2-leg ladders.

Firstly Chapter 2 gives the reader an essential introduction to the fundamental concepts of 1-dimensional spin systems and the quantum mechanical methods used to understand them. The content in this chapter is very well known and can be found in a myriad of textbooks, lecture notes and papers [1, 2, 3, 4]. Chapter 3 gives an overview of the DMRG algorithm, the numerical method used to solve the systems in this thesis. The reader is taken through a single step of this renormalization group technique to demonstrate the calculation. Chapters 4-6 comprise the results and discussion of the research, making up the bulk of the thesis.

Chapter 4 is devoted to the anisotropic Heisenberg chain. At the beginning of this project the spin-

½ XXZ Heisenberg chain was to act as a confirmation of algorithm integrity and analysis techniques before moving to the main topic of the research, the 2-leg ladder. However interesting results arose pertaining to the nature of the effects of open boundary conditions on such a system. While it is a well known phenomenon that open boundary conditions creates effects in the system it isn't well documented, typically only worthy of a short comment. Investigating these effects became an important section of the research. Here we review and provide a basic understanding on how open boundary conditions affect the energy of a system and discuss the emergent effects of boundary conditions.

The discussion about the 2-leg Heisenberg ladder is split into two parts, the isotropic and anistropic models. Chapter 5 introduces the ladder model, more specifically the isotropic leg coupling case. An examination reveals the effects of open boundaries and the emergence of edge states in this system. The following chapter (Chapter 6) is the main focus of the research, delving into the phase diagram of the anistropic ladder which is shown to have a very rich phase diagram.

An XXZ anisotropy is introduced on both the legs and the rungs of the ladder opened a rich and extensive parameter space. Using the spin energy gap between states we investigate the phases of the ladder, both in a strong rung coupling regime and a weak coupling regime. Quantum field theory equations provide phase transition lines that can we use to compare theoretical predictions to the weak coupling experimental results.

# Chapter 2

# 1D Physics

This chapter will introduce the basics of quantum spin systems and their physics. This will lead into the physics of chains, one of the most fundamental models in condensed matter theory. The following section will deal with the physics of spin ladders, highlighting fundamental results that provide background for the main research topic of this thesis, spin ladder phase diagrams.

## 2.1 Quantum spin systems

In quantum spin systems we are concerned with the physics of interacting particles on a regular lattice geometry. The geometry of a system sets the foundational structure which the model builds on top of with interactions, dimerizations and frustrations. In practice the energy $\varepsilon$ of spin angular momentum interaction between two particles is given as,

$$\varepsilon = \alpha \vec{S}_1 \cdot \vec{S}_2 + \beta S_1^z S_2^z \tag{2.1.0.1}$$

Equation (2.1.0.1) factors in Heisenberg exchange interaction ($\vec{S}_1 \cdot \vec{S}_2$) and a spin anisotropy originating from the spin-orbit interaction ($S_1^z S_2^z$). The exchange interaction is typically only short-range as it is dependent on the overlap of atomic wavefunctions. This equation calculates the energy of the interaction between spins as a function of $\alpha$ and $\beta$, where $\vec{S}_n$ is a spin vector of cartesian dimensions ($S^x$, $S^y$, $S^z$). We define the constant $J$ as the value of the interaction coupling between the spins where $J < 0$ represents an interaction that prefers parallel alignment of the spins. In contrast, $J > 0$ favors an antiparallel alignment. It is therefore energetically favorable to have parallel alignment when $J < 0$ and an antiparallel alignment when $J > 0$. Parallel alignment is known as ferromagnetism ($\uparrow\uparrow\uparrow\uparrow$ or $\downarrow\downarrow\downarrow\downarrow$) and antiparallel alignment is known as antiferromagnetism ($\uparrow\downarrow\uparrow\downarrow$). Having $\alpha = J$, $\beta = 0$ gives the Heisenberg interaction in which

there is no favored axis of alignment. $\alpha = 0$, $\beta = J$ is the Ising interaction where alignment is favored on the $z$-axis.

All particles are assigned quantum numbers to describe their properties and classifications. The angular momentum quantum number $l$, has half-integer values for fermions and integer for bosons. To further describe the eigenstates of these particles we have the spin quantum number $m$, where $m = -l, -l+1, \ldots, l-1, l$. An electron (i.e. fermion) will have $l = \frac{1}{2}$ so that $m = -\frac{1}{2}, \frac{1}{2}$. These are more commonly known as spin-down and spin-up, respectively. A boson (i.e. photons) with $l = 1$ has eigenstates $m = -1, 0, 1$.

For a single spin-½ particle, quantized along the $S^z$ axis, the eigenstates can we represented by simple kets. As this thesis deals almost exclusively with spin-½ particles it will be easier to establish a shorthand notation for the values of $m$. Since the conversation is about spin, an intuative notation is arrows ($\uparrow$ or $\downarrow$), representing these values as follows,

$$\begin{aligned} \left|\frac{1}{2}\right\rangle &\equiv |\uparrow\rangle \\ \left|-\frac{1}{2}\right\rangle &\equiv |\downarrow\rangle \end{aligned} \tag{2.1.0.2}$$

These eigenstates are Hermitian making them normalized and orthogonal, forming a complete set such that,

$$\begin{aligned} \langle\uparrow|\uparrow\rangle = \langle\uparrow|\downarrow\rangle = 1 \\ \langle\uparrow|\downarrow\rangle = 0 \end{aligned} \tag{2.1.0.3}$$

From this an arbitrary spin state, known as a spinor, can be written,

$$\psi = \alpha\,|\uparrow\rangle + \beta\,|\downarrow\rangle = \begin{pmatrix} \alpha \\ \beta \end{pmatrix} \tag{2.1.0.4}$$

When discussing spin systems the main observable is typically the cartesian coordinates of the spin ($x$, $y$, $z$). Conventially these are the self-adjoint operators, $S^x$, $S^y$, $S^z$ whose spectrum of eigenvalues are the possible values one might get if that component of the spin is measured. These values are given by $\hbar m$, such that a measurement $\delta$ on an arbitrary cartesian axis is,

$$\delta(S^i) = m_i\hbar | m_i = m = -l, -l+1, \ldots, l-1, l \tag{2.1.0.5}$$

Each spin operator has a normalized eigenvector to correspond to each eigenvalue $|S_i, m_i\rangle$, such that

if the system is in state $|\psi\rangle$ the probability of measuring eigenvalue $m_i\hbar$ of spin component $i$ is,

$$\left|\langle S^i, m_i|\psi\rangle\right|^2 \tag{2.1.0.6}$$

We use this arbitrary state to build the spin-½ operators which calculate the spin state observables, noticing these are the Pauli matrices ($\sigma_x$, $\sigma_y$, $\sigma_z$) with an additional factor of ℏ/2. By choosing to quantize the z-axis these operators become,

$$\begin{aligned} S^x &= \frac{\hbar}{2}\begin{pmatrix} 0 & 1 \\ 1 & 0 \end{pmatrix} = \frac{\hbar}{2}\sigma_x \\ S^y &= \frac{\hbar}{2}\begin{pmatrix} 0 & -i \\ i & 0 \end{pmatrix} = -\frac{\hbar}{2}\sigma_y \\ S^z &= \frac{\hbar}{2}\begin{pmatrix} 1 & 0 \\ 0 & -1 \end{pmatrix} = \frac{\hbar}{2}\sigma_z \end{aligned} \tag{2.1.0.7}$$

As it will be convenient later, we introduce the notation for creation and annihilation operators $S^+$ and $S^-$.

$$S^+ = \begin{pmatrix} 0 & 1 \\ 0 & 0 \end{pmatrix} \quad S^- = \begin{pmatrix} 0 & 0 \\ 1 & 0 \end{pmatrix} \tag{2.1.0.8}$$

where,

$$\begin{aligned} S^+ &= S^x + iS^y \\ S^- &= S^x - iS^y \end{aligned} \tag{2.1.0.9}$$

Operating on a spin state gives,

$$\begin{aligned} S^z|\uparrow\rangle &= \frac{1}{2}\hbar|\uparrow\rangle = \frac{1}{2}|\uparrow\rangle \\ S^z|\downarrow\rangle &= -\frac{1}{2}\hbar|\downarrow\rangle = -\frac{1}{2}|\downarrow\rangle \\ S^+|\uparrow\rangle &= 0 \qquad S^-|\downarrow\rangle = 0 \\ S^+|\downarrow\rangle &= |\uparrow\rangle \qquad S^-|\uparrow\rangle = |\downarrow\rangle \end{aligned} \tag{2.1.0.10}$$

### 2.1.1 Interacting spin-$\frac{1}{2}$ particles

The interactions between particles in a given system is the most important factor for understanding the emergent properties of that system. This section will introduce the basics of interacting spin-½ particles by examining and calculating the energy of a simple two spin system.

Classically, angular momentum (i.e. spin) is treated as a vector. Therefore the energy of the interaction of the spin vectors is dependent on the angle between them.

$$\begin{aligned} E_{classical} = \vec{S}_1 \cdot \vec{S}_2 &= S_1 S_2 \cos\theta \\ &= \frac{1}{4}\cos\theta \end{aligned} \tag{2.1.1.1}$$

Here $S_1 = S_2 = \frac{1}{2}$, such that the energy can takes continuous values between -¼ and ¼. However quantum mechanically the energy spectrum is discrete rather than continuous. We are therefore interested in the energy eigenstates of the system, those states that remain unchanged when operated on by the Hamiltonian equation. This derivation examines the ground state and elementary excitations this means the system is at zero temperature ($T = 0$). The system is described by a basis which is then used to build a Hamiltonian matrix, $H$, to calculate the energy eigenstates.

$$|\uparrow\uparrow\rangle, |\uparrow\downarrow\rangle, |\downarrow\uparrow\rangle, |\downarrow\downarrow\rangle \tag{2.1.1.2}$$

For an isotropic Heisenberg interaction,

$$\hat{H} = J\vec{S}_1 \cdot \vec{S}_2 = \frac{J}{2}(S_1^+ S_2^- + S_1^- S_2^+) + JS_1^z S_2^z \tag{2.1.1.3}$$

$$\begin{aligned} \hat{H}\,|\uparrow\uparrow\rangle &= \frac{1}{4}J\,|\uparrow\uparrow\rangle \\ |\uparrow\downarrow\rangle &= -\frac{1}{4}J\,|\uparrow\downarrow\rangle + \frac{1}{2}J\,|\downarrow\uparrow\rangle \\ |\downarrow\uparrow\rangle &= -\frac{1}{4}J\,|\downarrow\uparrow\rangle + \frac{1}{2}J\,|\uparrow\downarrow\rangle \\ |\downarrow\downarrow\rangle &= \frac{1}{4}J\,|\downarrow\downarrow\rangle \end{aligned} \tag{2.1.1.4}$$

$$\hat{H} = J\begin{pmatrix} \frac{1}{4} & 0 & 0 & 0 \\ 0 & -\frac{1}{4} & \frac{1}{2} & 0 \\ 0 & \frac{1}{2} & -\frac{1}{4} & 0 \\ 0 & 0 & 0 & \frac{1}{4} \end{pmatrix} \tag{2.1.1.5}$$

| state | explicit form | 'picture' | $S_T$ | $S_T^z$ | E | Degeneracy |
|---|---|---|---|---|---|---|
| $\psi_1$ | $\|\uparrow\uparrow\rangle$ | $\uparrow\uparrow$ (FM) | 1 | 1 | $\frac{J}{4}$ | |
| $\psi_2$ | $\frac{1}{\sqrt{2}}(\|\uparrow\downarrow\rangle + \|\downarrow\uparrow\rangle)$ | $\rightarrow\rightarrow$ (FM) | 1 | 0 | $\frac{J}{4}$ | triplet |
| $\psi_3$ | $\|\downarrow\downarrow\rangle$ | $\downarrow\downarrow$ (FM) | 1 | -1 | $\frac{J}{4}$ | |
| $\psi_4$ | $\frac{1}{\sqrt{2}}(\|\uparrow\downarrow\rangle - \|\downarrow\uparrow\rangle)$ | $\uparrow\downarrow$ (AFM) | 0 | 0 | $-\frac{3J}{4}$ | singlet |

Table 2.1: Comprehensive table detailing the states of a 2-spin system. From Parkinson and Farnell [1].

Diagonalization of this matrix gives 4 eigenstates, comprised of a triplet and a singlet state.

$$\psi_1 \equiv \begin{pmatrix} 1 \\ 0 \\ 0 \\ 0 \end{pmatrix} \quad \psi_2 \equiv \begin{pmatrix} 0 \\ \frac{1}{\sqrt{2}} \\ \frac{1}{\sqrt{2}} \\ 0 \end{pmatrix} \quad \psi_3 \equiv \begin{pmatrix} 0 \\ 0 \\ 0 \\ 1 \end{pmatrix} = \frac{J}{4} \qquad (2.1.1.6)$$

$$\psi_4 \equiv \begin{pmatrix} 0 \\ \frac{1}{\sqrt{2}} \\ -\frac{1}{\sqrt{2}} \\ 0 \end{pmatrix} = -\frac{3J}{4}$$

These solutions reveal a triplet of degenerate states with an eigenvalue identical to the classical case. However, the singlet state has a different energy than the classical case which means there is a quantum effect occurring. The triplet states all have total 'spin-1' configurations and the singlet state is a 'spin-0' configuration. The triplet states are differentiated by their $S_T^z$ values. Due to the Heisenberg uncertainty principle all spin components can not be known so the $S^z$ is chosen as the quantized axis.

| | |
|---|---|
| $S_T = S_1 + S_2$ | $J > 0$ $g.s. = AFM$ |
| $S_T^z = S_1^z + S_2^z$ | $J < 0$ $g.s. = FM$ |

This 2-spin system, while important for understanding small systems, gives a limited view of the true dimensions of reality. A magnetic crystal consists of a macroscopic number of atoms in a regular array. The goal then is to extend the model to the thermodynamic limit where the number of atoms in the array, N, increases to infinity. Such a limit better describes realistic systems.

For a spin-½ particle system the Hamiltonians can be summed up simply, starting with the most general case,

a. Full Anisotropic Heisenberg (XYZ) $\sum_{i=1}^{N}[J^x S_i^x S_{i+1}^x + J^y S_i^y S_{i+1}^y + \Delta S_i^z S_{i+1}^z]$

b. Heisenberg (XXX) $J\sum_{i=1}^{N} S_i \cdot S_{i+1}$

c. Ising $J\sum_{i=1}^{N} S_i^z S_{i+1}^z$

d. (XY) $J\sum_{i=1}^{N}(S_i^x S_{i+1}^x + S_i^y S_{i+1}^y)$

e. Anisotropic Heisenberg (XXZ) $J\sum_{i=1}^{N}[(S_i^x S_{i+1}^x + S_i^y S_{i+1}^y) + \Delta S_i^z S_{i+1}^z]$

Often times when dealing with spin models, the differentiation between degrees of freedom is noted using X,Y, and Z to represent the three couplings in the system. The most general form is the XYZ type with separate exchange couplings for each coordinate axis. The limiting cases include the pure isotropic and Ising models with crossover models like the XXZ and XY.

### 2.1.2 Spin-$\frac{1}{2}$ chain

The chain is one of the most fundamental lattice geometries that can be studied. Its arrangement appears in more complex geometries, therefore understanding the chain will provide knowledge of more complex models. For a linear chain the simplest state is the fully aligned state. This means all of the spins are pointed in the same direction, all up $|\uparrow\rangle$ or all down $|\downarrow\rangle$. This state is the ground state for the ferromagnetic (FM) interaction.

$$\begin{aligned} &|\uparrow\uparrow\uparrow\uparrow\uparrow\uparrow\uparrow \ldots \uparrow\uparrow\uparrow\uparrow\rangle \\ &|\downarrow\downarrow\downarrow\downarrow\downarrow\downarrow\downarrow \ldots \downarrow\downarrow\downarrow\downarrow\rangle \end{aligned} \tag{2.1.2.1}$$

Taking these as the simplest states, an elementary excitation consists of flipping one of the spins such that it is misaligned with all of the others. In actuality these states of excitation are linear combinations of many of these single excitation states. However for this calculation we will observe, non-linear combination states.

The basis for a chain system is built from all possible states of the system, which in this case is $2^N$ states, where $N$ is the number of spins in the chain. It is easy to see that this basis gets very large with comparatively few spins, becoming unwieldy for exact diagonalization algorithms. We begin the derivation by finding the eigenstates for this basis, given the following model Hamiltonian $\hat{H}$, total spin

$S^z_{tot}$ and commutation relations,

$$\begin{aligned} \hat{H} &= J\sum_{i=1}^{N}[\frac{1}{2}(S_i^+ S_{i+1}^1 + S_i^- S_{i+1}^+) + S_i^z S_{i+1}^z] \\ S^z_{tot} &= \sum_j S_j^z \end{aligned} \tag{2.1.2.2}$$

Commutations,

$$\begin{aligned} [S^z_{tot}, S_i^z S_{i+1}^z] &= 0 \\ [S^z_{tot}, S_i^+ S_{i+1}^-] &= S_i^+[S_T^z, S_{i+1}^-] + [S_T^z, S_i^+]S_{i+1}^- = 0 \\ [S^z_{tot}, S_i^- S_{i+1}^+] &= 0 \\ [S^z_{tot}, \hat{H}] &= 0 \\ [S^2_{tot}, \hat{H}] &= 0 \end{aligned} \tag{2.1.2.3}$$

Notice that the Hamiltonian describes an interaction between the first and last spins in the chain. This creates a 'periodic' boundary such that the wavefunction of the system is periodic and is simpler to solve. The boundary conditions are a very important property of the system especially the low energy states, as will be detailed in a later chapter. We have chosen the eigenstates of $\hat{H}$ to be simultaneous eigenstates of both $S_T^z$ and $S_T^2$ because they commute with the Hamiltonian. In this way the energy and spin observables can be measured simultaneously without uncertainty.

Focusing on the $S_T^z = N\frac{1}{2}$ aligned state, we show this state is an eigenstate of $\hat{H}$.

$$|A\rangle = |\uparrow\uparrow\uparrow\uparrow\uparrow\uparrow\uparrow \ldots \uparrow\uparrow\uparrow\uparrow\rangle \tag{2.1.2.4}$$

$$\begin{aligned} \hat{H}\,|A\rangle &= J\sum_{i}^{N}[\frac{1}{2}(S_i^+ S_{i+1}^- + S_i^- S_{i+1}^+) + S_i^z S_{i+1}^z]\,|A\rangle \\ &= J\sum_{i}^{N}[0 + \frac{1}{4}]\,|A\rangle = N\frac{J}{4}\,|A\rangle \end{aligned} \tag{2.1.2.5}$$

Therefore state $|A\rangle$ is an eigenstate of $\hat{H}$ with energy $E_A = N\frac{J}{4}$. From here it is easy to see that for $J < 0$ (FM alignment) $|A\rangle$ is the ground state with energy $E_A$, same as the classical case. This holds true for a state of all down-spins. Conversely, for $J > 0$ (AFM alignment) $|A\rangle$ is the state of highest energy, which is still an eigenstate.

Here we have calculated the eigenstates for the aligned states of the fully Heisenberg model. The next step would be to calculate the eigensets for a single excitation state, then for two excitation states, for

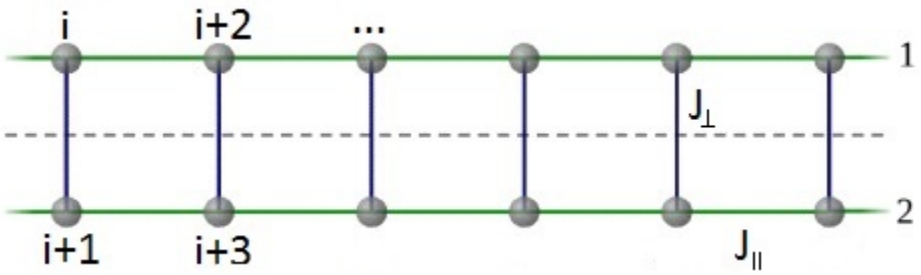


Figure 2.1: Diagram of ladder geometry with leg and rung couplings ($J_{\parallel}$ and $J_{\perp}$ respectively) with site counter.

three, and etc. However as this thesis focuses on the anisotropic Heisenberg model, we will conclude this derivation here and note that the fully Heisenberg model is a solved exactly via the Bethe ansatz [5], a readily available derivation.

The spin-½ anisotropic Heisenberg XXZ chain can exist in a number of phases as a function of its couplings $\left|\frac{J_z}{J_{xy}}\right| > 1$. In the regime $\left|\frac{J_z}{J_{xy}}\right| < -1$ the chain exists in an Ising ferromagnetic phase and is not a Luttinger liquid. At the point the ratio is equal to $-1$ the chain is an Heisenberg ferromagnet. In the XY-phase ($\left|\frac{J_z}{J_{xy}}\right| < 1$) these chains are Luttinger liquids, with the elementary excitations described by spin waves. A solid treatment of the XY chain with open boundary conditions was done by Mikeshi [6]. These excitations are gapless and the system displays power-law decay of spin correlation functions. For $\left|\frac{J_z}{J_{xy}}\right| > 1$ the chain phase transitions to the Néel state that has gapped excitations and the spin correlations decay exponentially [2].

## 2.2 Ladder physics

By adding an additional chain and couplings, it is possible to create a ladder-like arrangement of spins, see figure 2.1. The Hamiltonian of such a geometry can have up to nine separate couplings including intra- (leg) and interchain (rung) parameters, leading to a variety of isotropic and anisotropic models.

The ladder presents a more difficult model to solve but much more rich environment to explore. Notably it can function as a crossover between spin-½ systems and spin-1 systems as well as going from 1D to 2D models.

$$\begin{aligned}\hat{H} = \sum_{j,n=1,2} J_{\parallel}^{xy}(S_{j,n}^{+}S_{j+1,n}^{-} + S_{j,n}^{-}S_{j+1,n}^{+}) + J_{\parallel}^{z}S_{j,n}^{z}S_{j+1,n}^{z} \\ + \sum_{j} J_{\perp}^{xy}(S_{j,1}^{+}S_{j,2}^{-} + S_{j,1}^{-}S_{j,2}^{+}) + J_{\perp}^{z}S_{j,1}^{z}S_{j,2}^{z}\end{aligned} \tag{2.2.0.1}$$

An isotropic $J_{\perp}$ (rung) coupling allows for the model range from two decoupled spin-½ chains to an

effective spin-1 chain. Setting $J_\perp = 0$ results in two decoupled, independent spin-½ chains. If $J_\perp$ is large and ferromagnetic ($J_\perp < 0$), the chains are tightly coupled. However due to the ferromagnetic character, the rungs form, in essence, a two spin chain combining to form a triplet state. As described above this triplet state is a spin-1 particle, which results in an effective spin-1 chain. Such a chain exhibits the characteristics of a spin-1 chain, including the Haldane gap [7]. However, as will be demonstrated in a later section, the system is sensitive to boundaries in this state. Thus we can test our methods against a variety of known results including a stock spin-1 chain and decoupled spin-½ chains.

On the other side of the spectrum, making $J_\perp$ antiferromagnetic ($> 0$) results in a system of rung singlets. As $J_\perp$ is large, the rung singlet system exhibits a spin excitation gap. Here we have laid out understanding of the ladder system for the zeroth, large ferro- and large antiferromagnetic limits.

The weak coupling limit was solved by Shelton, Nersesyan and Tsvelik [8] through bosonization and related techniques. They showed that a spin gap opens immediately for $J_\perp \neq 0$ regardless of the sign. The gap in this limit has been shown to come from the confinement of quasiparticles known as spinons [9]. These spinons represent the spin component of an elementary excitation of a fermion system. The spinons cannot propagate through the system due to the relatively large leg couplings, resulting in their confinement.

Ladders have been shown to be sensitive to boundary conditions (periodic, open, etc). Lecheminant and Orignac [10] showed that the effect of a boundary was very different for each sign. The ferromagnetic rung coupling produces spin-½ edge states. Conversely such edge states are absent in the AFM phase. The edge state phase is known as a topological phase, while the AFM state is a non-topological phase. In the large FM rung limit the system is similar to the spin-1 chain, as shown previously, which, under these boundary conditions, causes the emergence of spin-½ states to appear at the ends (edges) of the legs. This result is explained by the AKLT model [11], an extension of the 1D quantum Heisenberg spin model with a valence bond solid ground state that describes a good approximation to the ground state of the spin-1 chain. The transition across the $J_\perp = 0$ point between a topological and non-topological phase is a much discussed topic in spin-ladder research.

The trouble with materials is they, more often than not, have fixed interaction strengths. So accessing the theoretically possible phases requires some external input. Mazo et al [12] proposed using voltage gates to induce changes in a bilayer graphene system and tune exchange couplings. This setup creates a system isomorphic to the low energy dynamics of spin-½ ladders. The effective spin ladder has

a helical nature which opens it to spin-correlation probing techniques. More importantly for this thesis, the authors of the paper develop, using bosonization and field theory, a framework for calculating the phase boundaries for the anisotropic ladder. Theoretical phase transition lines will be drawn from these equations and compared to density maps in results section of this thesis.

There has been a few studies examining portions of the ladder phase diagram using varying parameter regimes however the overlap is minimal. This thesis provides much better coverage of the parameter space to give a consistent phase diagram, uniting the portions of the phase space already researched. Quite recently Li et al [13] took a page from quantum information science by utilizing a tensor network algorithm to calculate the fidelity of groundstates of the fully anisotropic Heisenberg spin ladder to create a phase diagram. From quantum information science the concept of fidelity is the measure of the similarity of two states. It is typically used to compare the setup of an experimental quantum state to the ideal state. Then it is natural to use this to characterize acute changes in quantum states as they transition between phases [14]. This study uses a fully anisotropic XXZ model such that the $z$-couplings are decoupled from the $xy$-couplings on both axes. The analysis indicates a variety of phases in this parameter space including the pure FM, striped-FM, $xy\pm$, Haldane and others. The full diagram indicates 9 phases, see figure 2.2a.

An examination of the ground state phase diagram was done by Hijii et al [15] for an isotropic rung and anisotropic leg model. This study found a total of 8 phases for a $\Delta_{leg}$ spanning both the ferro- and antiferromagnetic regimes, see figure 2.2b. The phase boundaries between the $XY$ phases and the Haldane and rung-singlet phases was investigated closely using level spectroscopy and twisted boundary condition methods. This study also examines the phase boundaries themselves, calculating their rough locations using variational approaches for some transitions and unitary transformations for others. Notably this paper confirms the existence of two separate $XY$ phases, which had been questioned up to this point. As a whole this research calculated the boundaries between all of the phases on the diagram using one method or another, making sure to examine the multicritical points and determine the $XY$ phases.

Using DMRG techniques Ramos and Xavier [16] made precise numerical estimations for the ground state energy per site for a number of ladder types in the thermodynamic limit, including odd and even number of legs, and integer and half-integer spins. Up to this point there were very few studies of ladders with spin $S > 1/2$ for more than one leg. Using extrapolation the ground state energy was estimated up to the thermodynamic limit for spins up to $5/2$. More significantly this study also calculates estimations for the spin gap $\Delta_s$, values typically not found in the literature except in a few cases. For the 2-leg spin

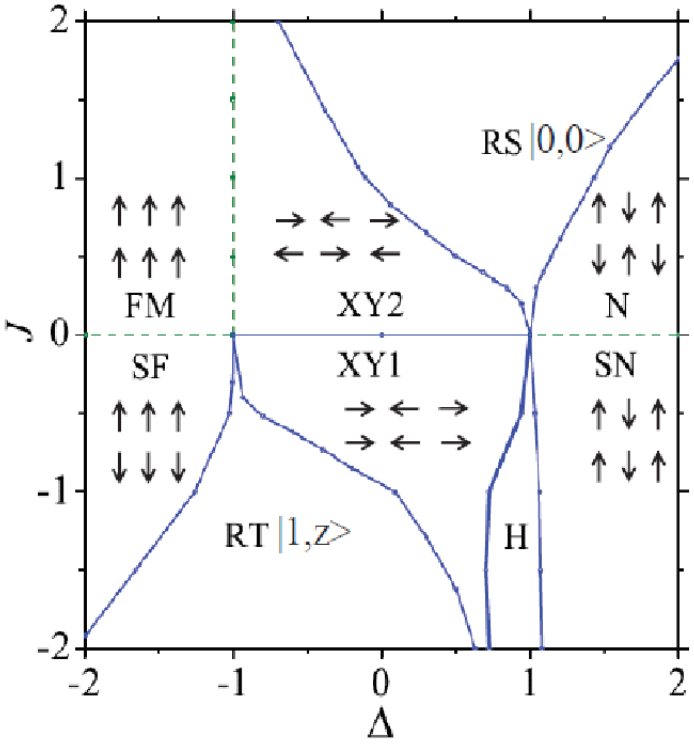


(a) Phase diagram for the 2-leg spin-½ XXZ spin ladder from the work of Li et al [13] showing 9 phases. These include FM=ferromagnetic, SF=striped-ferromagnetic, XY1 and XY2 as XY phases, RT=rung-triplet, RS=rung-singlet, H=Haldane, N=Néel and SN=stripe-Néel.

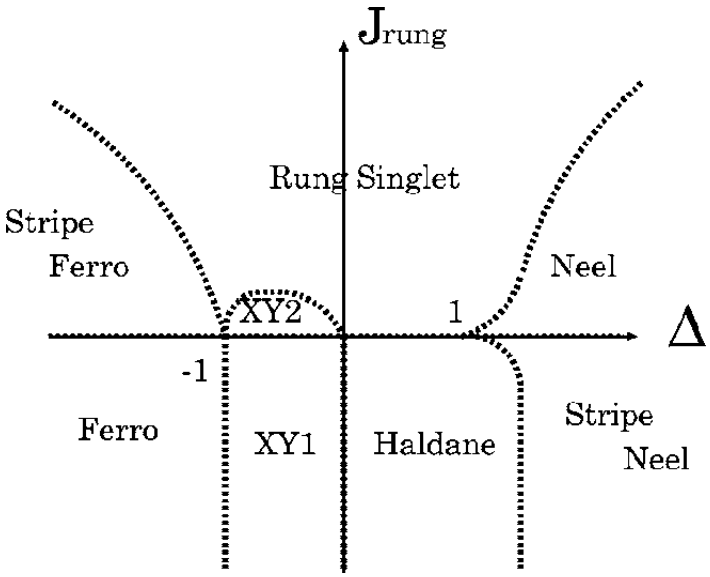


(b) Phase diagram for the 2-leg spin-½ XXZ spin ladder showing 8 phases from the work of Hijii et al [15]. The phases in this diagram include ferro- and striped-ferromagnetic, XY phases (XY1 and XY2), rung-singlet, Haldane, Néel and striped-Néel.

Figure 2.2: 2-leg spin-½ anisotropic Heisenberg spin ladder phase diagrams by Li et al and Hijii et al.

$S = 1/2$ case this value is $\Delta_s = 0.5011$, a value that can be used as a baseline to check the algorithms being used in this thesis. Importantly this work also confirms the Haldane conjecture [7] of a gap for integer spin chains and zero gap for half-integer spin chains as well as the Sénéchal-Sierra [17, 18] conjecture that states spin excitations are gapless for an odd number of legs and gapped for an even number of legs.

Similarly Barnes et al [19] used Lanczos and Monte Carlo techniques to model a Heisenberg 2-leg ladder, calculating ground state energy and singlet-triplet energy gap as a function of the leg-rung coupling anisotropy. The study gives numerical values for a number of anisotropies concluding that the ladder is gapped for all rung couplings $J_\perp > 0$, suggesting the model is very sensitive to small $J_\perp$ perturbations. The excitation states, in this case spin-triplets, form a band of energies determined mostly by the leg coupling $J$. The singlet-triplet gap however is a function of both the leg and rung couplings. The numerical results in this study provided a good reference point for comparison with out data.

In summary ladders are a rich arena of research. A spin-½ ladder with an even number legs has a gapped excitation spectrum, while an odd number of legs can be mapped to a spin-½ chain and therefore has a gapless excitation spectrum. In the limit of decoupled chains ($J_\perp = 0$) the system takes on the characteristics of the individual chains, in this case the excitations are gapless. A gap opens up immediately for $J_\perp \neq 0$, for either sign. This excitation gap is easy to see in the strong rung limit ($J_\perp > J_\parallel$). For antiferromagnetic $J_\perp$ the ground state consists of a series of rung singlets with an excitation promoting a singlet to the higher energy triplet state costing energy $J_\perp$. When $J_\perp$ is large and ferromagnetic the ladder gives an effective spin-1 chain which should exhibit the Haldane gap. Conversely when $J_\perp$ is antiferromagnetic the system consists of a series of gapless rung singlets, as previously stated. Ladders systems are quite sensitive to boundaries.

Introducing boundaries at the edges of a ladder results in the emergence of spin-½ edge states for ferromagnetic rung couplings. These states are absent in the antiferromagnetic regime. The phase diagram of the 2-leg ladder has been surveyed along a few regimes, reiterating the existence of a rich phase diagram that includes XY, rung-singlet and rung-triplet, Néel and striped-Néel, Haldane and ferromagnetic phases. Most of the surveys have been done with a degree of leg-rung coupling interdependence.

This thesis will present results for full XXZ anisotropies on both the leg and rung axes without any interdependence. The subsequent phase diagrams will confirm many of these known results but more importantly will survey a much larger parameter space, filling in many of the gaps missed by other recognized studies. In this way a better comprehensive understanding of the phases of the spin-½ will be gained.

### 2.2.1 Ladder materials

The variety of spin ladder phases and their properties make ladder materials a prime interest to the condensed matter community. Quite recently experimental realizations of spin ladders have been achieved and measured. Some of these compounds include vanadyl pyrophosphate $(VO)_2P_2O_7$ and the cuprate series $Sr_{n-1}Cu_{n+1}O_{2n}$ [20]. However a major issue with real materials is the fixed coupling strengths, making access to various phases difficult. A tunable structure would be ideal for accessing quantum phase transitions in real materials.

Neutron scattering and muon spin resonance experiments have shown short range spin order in the above materials along with a spin gap, measured via nuclear magnetic resonance. The cuprate series is also known to be a superconductor under high pressure [21], making it an intriguing material to study as the search for high temperature superconductors continues. Nagata et al showed that under high pressures and low temperatures, the ladder compound $Sr_{2.5}Ca_{11.5}Cu_{24}U_{41}$ undergoes a phase transition and begins superconducting along the legs.

Within the last few years there have been proposals to build tunable ladder models using low-dimensional materials and voltage gate systems. Mazo et al [12] put forth a method involving bilayer graphene sheets connected to a split-double-gate voltage system that would create a tunable spin ladder system. The model exploits helical quantum hall edge states and applied voltages to 'tune' the parameters of the ladder. This allows the user to access a given phase region at will by simply changing the voltage of the gates.

An interesting spin-½ ladder candidate is $(C_7H_{10}N)_2CuBr_4$, known colloquially as DIMPY [22]. This compound in particular shows strong leg characteristics with similar compounds showing strong rung properties. This chemical is of interest here because it was part of the motivation for this project and is being researched by chemists at the University of Kent.

# Chapter 3

# DMRG

In principle calculating the energy of a spin system is a fairly straight forward process, exactly diagonalize the Hamiltonian matrix. In practice however such a calculation would be exceedingly difficult or near impossible for any thermodynamic limit results. The difficulty lies with the Hilbert space, which grows to some degree, with each additional site added to the system, quickly reaching computational limits. There are many techniques to work around this problem, notably numerical methods including Lanzcos and renormalization.

This chapter will focus on a technique called DMRG which works by controlling the size of the "virtual" Hilbert space while the system grows and renormalizing the basis to ensure stability of the system. The following sections review the overall process and take the reader through a single DMRG step.

## 3.1 Density Matrix Renormalization Group

For 1-dimensional spin systems Density Matrix Renormalization Group (DMRG) is a popular and powerful algorithm for understanding the low energy physics of a quantum many-body system. DMRG provides a method to maintain a consistent virtual Hilbert space dimension while increasing the size of the system. It is for this reason that the algorithm was chosen for this research project as it allows access to large system sizes without compromising the integrity of an exact solution. The exact algorithm used was provided as a part of the ALPS package[1] (see Appendix B), implemented and run on the local computer cluster[2].

DMRG is an iterative numerical technique, developed by White [23], that allows the targeting of

[1] A software package that includes a variety of algorithms for physics simulations. `https://alps.ethz.ch`
[2] University of Kent, SPS Tor computer cluster

the most important states for a given system. The algorithm is based on Wilson's Numerical RG [24] technique which keeps the lowest energy eigenstates in each iteration. The idea is that the high energy states are not important for describing the low energy physics and are therefore discarded. In a typical NRG calculation the lowest energy states are kept in each iteration for the renormalization transformation. DMRG however, constructs a renormalization group transformation from the most probable eigenstates that make up a given system. Such a method allows access to much larger systems (up to a few thousand particles), leading to a better understanding of the thermodynamic limits of the system.

Solving an equally sized system explicitly using exact diagonalization would be absurdly computationally expensive as the amount of stored data increases exponentially (for a fermion chain) with each additional site. The DMRG algorithm maintains a fixed virtual Hilbert space size, the state space of the system, thus eliminating the need for a large amount of storage. The "physical" Hilbert space remains of the dimension $2^L$, where $L$ is the number of sites in the chain. The versatility of the algorithm allows for the size of the virtual Hilbert space to be chosen such that there can be a balance of calculation accuracy and computation time. For the purposes of simplicity all mentions to "the Hilbert space" refers to the virtual space, unless otherwise specified.

The stock DMRG includes the infinite and finite system algorithms, each can be broken down into a few simple steps, which are shown here. These steps will be explained in greater detail in the next section.

- Infinite System algorithm

    1. Form the block.
    2. Add a new site to the block to create the enlarged block.
    3. Couple two enlarged blocks to create the superblock.
    4. Diagonalize the superblock, calculate and diagonalize the density matrix.
    5. Transform the basis of the left enlarged block using the eigenbasis created from the density matrix. Use the $m$ largest density matrix eigenvalues.
    6. New left enlarged block becomes the left block for the next iteration.
    7. Repeat until the system has reached the desired size.

- Finite System algorithm

    1. Sweep the system once it hasw reached the desired size, calculating the most accurate results.

The advantage of the DMRG is that it truncates and renormalizes a new basis at each iteration. However, this comes with the disadvantage that the basis states are non-intuitive and a description of the states is dependent on the measurement of observables. Thus the observables also need to be transformed, meaning they also need to be stored on each iteration, along with the basis. The stock time-independent algorithms make it difficult to obtain dynamical information from DMRG because of the renormalization and transformation routines. However we won't be looking at dynamical quantities so this isn't an issue.

While there are a few different variants of DMRG (MPS, TEBD, TD-DMRG) depending on the desired calculation, for this research the stock DMRG was used, consisting of the infinite and finite system algorithms. Used in conjunction, these algorithms build the system and sweep through it finding the lowest energy and calculating other observables (correlations, magnetizations, entanglement, etc).

## 3.2 DMRG for spin systems

In this project we utilized two DMRG algorithms, the infinite and finite system algorithms. Each algorithm holds to the principles of DMRG while performing different tasks. The infinite system algorithm grows the system to the desired size from a small starting block. The finite system algorithm sweeps through a fixed size system calculating the most accurate results. In this section each algorithm will be explained by taking the reader through a single step of the algorithm.

### 3.2.1 Infinite System Algorithm

The basic idea behind this algorithm is to start with a small system, which can be solved exactly, then increase the size of the system without increasing the size of the Hilbert space. This procedure is done until the desired system size is reached, then the finite system algorithm can take over. The finite system algorithm 'sweeps' through the system, calculating the lowest energy states.

To maintain a fixed Hilbert space size, the space must be truncated back at each iteration. The truncation is broken down into 2 steps:

- The system size is increased (by adding lattice sites and placing spins on them), consequently the Hilbert space also increases due to these additional sites.
- The number of states in the Hilbert space is truncated back to a fixed size, thus remaining constant throughout the algorithm.

Following these steps the operators are renormalized to this new, truncated basis. The objective of the renormalization is to make sure that a small basis works for systems whose basis would normally be

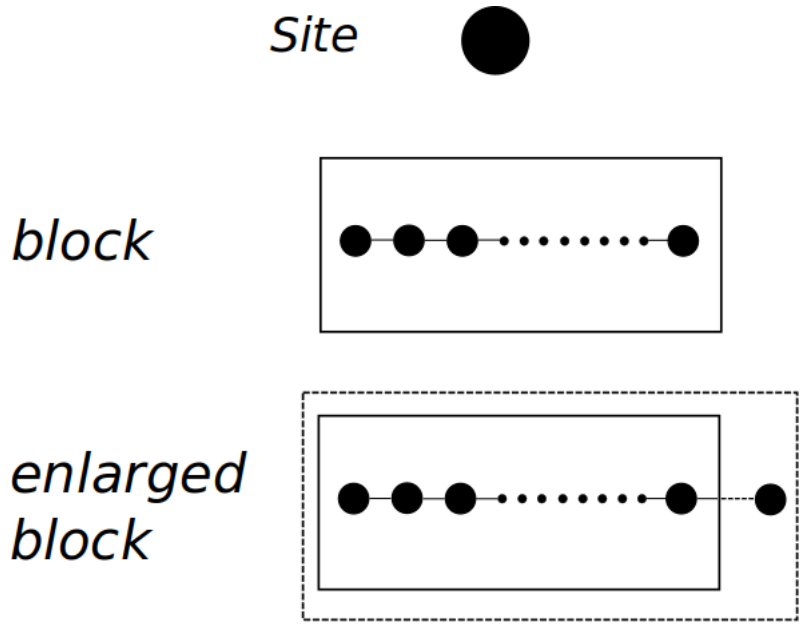


Figure 3.1: Visual representation of the basic constructs of the DMRG algorithm. The site, block, and enlarged block.

much larger. There are two important aspects that need to be done correctly for the renormalization procedure to work; growing the system by adding additional sites and deciding which states to keep in the truncation process. Here we are going to see a brief examination of these elements of the algorithm and proceed to answer the questions: how is the system grown? and how is the basis efficiently truncated?

To answer these questions we are going to walk through a single DMRG iteration for a small system.[3]. What we will show here is building the basis for each object (site, block, enlarged block and superblock, see figure 3.1) using the previous object, ultimately creating and solving the superblock Hamiltonian. The solution eigenset is then used to construct the density matrix, calculating the most probable states.

The first step in the algorithm is to construct a *block*, figure 3.1. Initially the first block will consist of a single site. A site is the elementary unit of spin systems and their state is described by $d_i$ ($i = 1, 2, \cdots, D$), where D is the dimensionality of the state. The Heisenberg model has D=2, while the Hubbard model has D=4. Since we are working in the Heisenberg model with a single spin-$\frac{1}{2}$ particle per site with quantized spin, we can then say that D=2 describes two states, an up spin ($\uparrow$) and a down spin ($\downarrow$). Therefore the block characteristics are given by $B(l, m)$, consisting of the number of sites $l$ in the block and $m$ the dimensionality of the block basis. The observables of the block are described by its Hamiltonian $H_B$.

The basis for this scenario is highly symmetric in quantum numbers ($S^z$, $N$) creating a block-diagonal matrix. The system is grown by adding a site to the block, creating an *enlarged block*, subsequently

[3]These DMRG steps follow Malvezzi's paper [25], using similar notation

enlarging the Hilbert space.

The bases of the block and the new site are described by $|b_1\rangle \cdots |b_m\rangle$ and $|d_1\rangle \cdots |d_D\rangle$, respectively. The basis of the enlarged block is then simply the direct product between the block and the new site.

$$|b_k^e\rangle = |b_i\rangle \otimes |d_j\rangle \tag{3.2.1.1}$$

$$\begin{array}{llll} |b_1\rangle = |\uparrow\rangle \;\; |d_1\rangle = |\uparrow\rangle & |b_1^e\rangle = |b_1\rangle \otimes |d_1\rangle & k = (i-1)D + j, \quad D = 2 \\ |b_2\rangle = |\downarrow\rangle \;\; |d_2\rangle = |\downarrow\rangle & \quad = |\uparrow\rangle \otimes |\uparrow\rangle = |\uparrow\uparrow\rangle & i = 1, j = 1 \quad k = 1 \\ & |b_2^e\rangle = |b_1\rangle \otimes |d_2\rangle & i = 1, j = 2 \quad k = 2 \\ & \quad = |\uparrow\rangle \otimes |\downarrow\rangle = |\uparrow\downarrow\rangle & i = 2, j = 1 \quad k = 3 \\ & \vdots \qquad\qquad \vdots & i = 2, j = 2 \quad k = 4 \end{array}$$

This gives an enlarged block basis of, $\mathrm{B^e}(2,4)$, where $k$ is a mapping to the new basis.

$$|b_1^e\rangle = |\uparrow\uparrow\rangle \qquad |b_2^e\rangle = |\uparrow\downarrow\rangle \qquad |b_3^e\rangle = |\downarrow\uparrow\rangle \qquad |b_4^e\rangle = |\downarrow\downarrow\rangle \tag{3.2.1.2}$$

With this basis we can form the Hamiltonian of the enlarged block, $H_\mathrm{e}$,

$$H_e = H_b \otimes I_d + \frac{1}{2}(S_b^+ \otimes S_d^- + S_b^- \otimes S_d^+) + S_b^z \otimes S_d^z \tag{3.2.1.3}$$

The enlarged block Hamiltonian, equation (3.2.1.3), describes the interactions between sites within in the block and the interaction between the rightmost spin of block and the new site. Calculating the direct products gives the subsequent Hamiltonian matrix is,

$$H_e = \begin{pmatrix} 1 & 0 & 0 & 0 \\ 0 & -1 & 2 & 0 \\ 0 & 2 & -1 & 0 \\ 0 & 0 & 0 & 1 \end{pmatrix} \tag{3.2.1.4}$$

In this first step we had $m = D = 2$ but as the starting block grows in size with each iteration this ratio will be $m > D$. It is trivial then to see that only the block Hamiltonian as well as the representation of the operators $S^+$, $S^-$, $S^z$ of the rightmost site in the block and the new site need to be saved. Only these pieces are needed to construct the enlarged block and therefore the superblock.

The superblock, Figure 3.2, is constructed by connecting two enlarged blocks together by their left

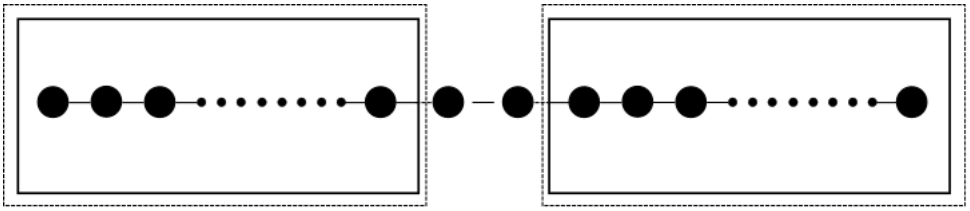

Figure 3.2: Representation of the superblock, consisting of two enlarged blocks.

and right-most sites, thus making the superblock spatially reflected. Similar to the construction of the enlarged block Hamiltonian that was constructed from the block operators, the superblock Hamiltonian is constructed from the enlarged block operators.

The enlarged bloch operators and the interations on the right-most site make up the superblock Hamiltonian, eq. (3.2.1.5).

$$H_s = H_e \otimes I_e^{'} + I_e \otimes H_e^{'} + \frac{1}{2}[(S_r^+)_e \otimes (S_d^-)_e + (S_b^-)_e \otimes (S_d^+)_e] + (S_b^z)_e \otimes (S_d^z)_e \tag{3.2.1.5}$$

where the primed operators refer to the second enlarged block used to build the superblock. The basis of the superblock is then the tensor product of the bases from the enlarged blocks.

$$\begin{pmatrix} |b_1^e\rangle \\ |b_2^e\rangle \\ |b_3^e\rangle \\ |b_4^e\rangle \end{pmatrix} \otimes \begin{pmatrix} \left|b_1^{'e}\right\rangle \\ \left|b_2^{'e}\right\rangle \\ \left|b_3^{'e}\right\rangle \\ \left|b_4^{'e}\right\rangle \end{pmatrix} = \begin{pmatrix} |\uparrow\uparrow\rangle \\ |\uparrow\downarrow\rangle \\ |\downarrow\uparrow\rangle \\ |\downarrow\downarrow\rangle \end{pmatrix} \otimes \begin{pmatrix} |\uparrow\uparrow\rangle^{'} \\ |\uparrow\downarrow\rangle^{'} \\ |\downarrow\uparrow\rangle^{'} \\ |\downarrow\downarrow\rangle^{'} \end{pmatrix} \tag{3.2.1.6}$$

This superblock basis gives 16 distinct states, however this can be reduced to six states if we exploit $S^z$ conservation and the $S^z = 0$ subspace to restrict ourselves to a smaller ground state section of the Hamiltonian matrix. Defining a new basis in the $S^z = 0$ subspace such that,

$$\begin{aligned}
\left|b_1^{s(0)}\right\rangle &\equiv |b_4^s\rangle = |\uparrow\uparrow\downarrow\downarrow\rangle \\
\left|b_2^{s(0)}\right\rangle &\equiv |b_6^s\rangle = |\uparrow\downarrow\uparrow\downarrow\rangle \\
\left|b_3^{s(0)}\right\rangle &\equiv |b_7^s\rangle = |\uparrow\downarrow\downarrow\uparrow\rangle \\
\left|b_4^{s(0)}\right\rangle &\equiv |b_{10}^s\rangle = |\downarrow\uparrow\uparrow\downarrow\rangle \\
\left|b_5^{s(0)}\right\rangle &\equiv |b_{11}^s\rangle = |\downarrow\uparrow\downarrow\uparrow\rangle \\
\left|b_6^{s(0)}\right\rangle &\equiv |b_{13}^s\rangle = |\downarrow\downarrow\uparrow\uparrow\rangle
\end{aligned} \tag{3.2.1.7}$$

The $s(0)$ superscript denotes the ground state magnetization sector ($S^z = M = 0$). The representation of the ground state sector Hamiltonian for the superblock is then,

$$H_s^{(0)} = \begin{bmatrix} 1 & 0 & 2 & 0 & 0 & 0 \\ 0 & -1 & 2 & 2 & 0 & 0 \\ 2 & 2 & -3 & 0 & 2 & 0 \\ 0 & 2 & 0 & -3 & 2 & 2 \\ 0 & 0 & 2 & 2 & -1 & 0 \\ 0 & 0 & 0 & 2 & 0 & 1 \end{bmatrix} \tag{3.2.1.8}$$

Solving this matrix gives the eigenset for the ground state where $E_0$ is the energy eigenvalue of the state and $|\Psi_0\rangle$ is the eigenvector,

$$E_0 = -\frac{1}{4}(3 + 2\sqrt{3}), \qquad |\Psi_0\rangle = \frac{1}{2\sqrt{3(2+\sqrt{3})}} \begin{pmatrix} -1 \\ -1-\sqrt{3} \\ 2+\sqrt{3} \\ 2+\sqrt{3} \\ -1-\sqrt{3} \\ -1 \end{pmatrix} \tag{3.2.1.9}$$

The elements in the eigenvector make up the non-zero elements in the ground state matrix, given by,

$$|\Psi_0\rangle = \sum_{i=1}^{mxD} \sum_{j=1}^{m'xD} a_{ij} \left|b_i^e\right\rangle \otimes \left|b_j^e\right\rangle = \begin{pmatrix} a_{11} & a_{12} & a_{13} & a_{14} \\ a_{21} & a_{22} & a_{23} & a_{24} \\ a_{31} & a_{32} & a_{33} & a_{34} \\ a_{41} & a_{42} & a_{43} & a_{44} \end{pmatrix} \tag{3.2.1.10}$$

These elements will be used to construct the reduced density matrix which tells the DMRG algorithm of the states that contribute the most to the target state (ground state in this case). The reduced density matrix describes a composition of two distinct systems A and B, in our case the left and right enlarged blocks. In the current iteration the density matrix is in the enlarged block basis.

The reduced density matrix is given by,

$$\rho_{ii'} = \sum_{j=1}^{m'xD} a_{ij} a^*_{i'j} = \frac{1}{12(2+\sqrt{3})} \begin{pmatrix} 1 & 0 & 0 & 0 \\ 0 & 11+6\sqrt{3} & -2(5+3\sqrt{3}) & 0 \\ 0 & -2(5+3\sqrt{3}) & 11+6\sqrt{3} & 0 \\ 0 & 0 & 0 & 1 \end{pmatrix} \tag{3.2.1.11}$$

Assembling the eigensets of the density matrix gives us a singlet and a triplet state, as expected for calculation of the ground state.

$$|\uparrow\uparrow\rangle = \frac{1}{12(2+\sqrt{3})} \begin{pmatrix} 1 \\ 0 \\ 0 \\ 0 \end{pmatrix}$$

$$\frac{|\uparrow\downarrow\rangle + |\downarrow\uparrow\rangle}{\sqrt{2}} = \frac{1}{12(2+\sqrt{3})} \begin{pmatrix} 0 \\ 1 \\ 1 \\ 0 \end{pmatrix} \qquad \frac{|\uparrow\downarrow\rangle - |\downarrow\uparrow\rangle}{\sqrt{2}} = \frac{21+12\sqrt{3}}{12(2+\sqrt{3})} \begin{pmatrix} 0 \\ 1 \\ -1 \\ 0 \end{pmatrix}$$

$$|\downarrow\downarrow\rangle = \frac{1}{12(2+\sqrt{3})} \begin{pmatrix} 0 \\ 0 \\ 0 \\ 1 \end{pmatrix}$$

The states are then ordered based on the eigenvalue, largest first (singlet state). This next step is key to the DMRG algorithm because it specifies and performs the truncation of the Hilbert space and constructs the necessary transformation operator. The transformation operator acts on the Hamiltonian and spin operators to transform them to the new, truncated basis.

We define the truncated basis to consist (arbitrarily in order to demonstrate the process) of the first two states of the original basis, based on their eigenvalues. These states are,

$$\frac{|\uparrow\downarrow\rangle - |\downarrow\uparrow\rangle}{\sqrt{2}}, \qquad |\uparrow\uparrow\rangle \tag{3.2.1.12}$$

The rows of the transformation matrix, $O$, are formed from these states,

$$O = \begin{pmatrix} 0 & \frac{1}{\sqrt{2}} & \frac{-1}{\sqrt{2}} & 0 \\ 1 & 0 & 0 & 0 \end{pmatrix} \tag{3.2.1.13}$$

Applying this transformation matrix to the enlarged block Hamiltonian $H_{\mathrm{e}}$, which in turn is applied to each of the spin operators, gives the Hamiltonian of the block for the next iteration.

$$H_{B(l+1,m)} = H_{B(2,2)} = OH_eO^\dagger = \frac{1}{4}\begin{pmatrix} -3 & 0 \\ 0 & 1 \end{pmatrix} \tag{3.2.1.14}$$

Similarly for the spin operators,

$$S_r^+ = O(S_r^+)_eO^\dagger = \frac{1}{\sqrt{2}}\begin{pmatrix} 0 & 0 \\ 1 & 0 \end{pmatrix} \qquad S_r^- = -\frac{1}{\sqrt{2}}\begin{pmatrix} 0 & 1 \\ 0 & 0 \end{pmatrix} \qquad S_r^z = \begin{pmatrix} 0 & 0 \\ 0 & 1 \end{pmatrix} \tag{3.2.1.15}$$

With the newly transformed operators the next iteration starts and the process repeats itself. This procedure demonstrates why DMRG is such a powerful technique despite adding a new site to the block the size of the Hilbert space hasn't changed. Additionally the states that make up the Hilbert space in each iteration will be those with the highest probability of making up the ground state on that iteration which maintains the integrity of the calculation.

The single DMRG iteration shown here was used to demonstrate the infinite size algorithm, in a practical application the truncation procedure would not begin until the number of states was significantly higher. For many of the simulations presented in later chapters the number of states was $m \geq 100$. It is also useful to calculate the severity of the truncation to better understand how the truncation of states is affecting the calculations. The truncation error is calculated by summing the discarded states from the reduced density matrix, $(1 - \sum_{\alpha=1}^{m} w_\alpha)$. This number should be as low as possible, ideally below $10^{-6}$.

### 3.2.2 Finite System Algorithm

The finite system algorithm differs from the infinite algorithm described in the previous section in that it doesn't grow the system with each iteration but 'sweeps' through a system of fixed size $L$ calculating the optimal basis. The finite system algorithm takes over when the infinite system algorithm has grown the system to the desired size. At this point the left and right enlarged blocks are of size ½.

From here the left block is grown while the right block is reduced in size, maintaining a fixed system size. The same procedures presented in the infinite system algorithm of building the Hamiltonian, calculating

the ground state eigensets, building the reduced density matrix and performing the transformations are done. When the right block is reduced to the size of a single site, the procedure is reversed so the left block is reduced while the right block is grown. One such iteration of this is called a 'sweep'. While the sweep is being performed all of the eigenset information is being stored. When the optimal, lowest energy basis is found for a specific left-right block size configuration this result is kept and used in the next iteration as a good guess of the basis for the right block.

Similar to the infinite system algorithm, the finite algorithm can be broken down in to a few simple steps,

- Finite Size algorithm

    1. Preliminary step: use the infinite system algorithm to grow the system to the desired size. Save all transformed operators to disk as they can be used later.
    2. Enlarge the left block size $l+1$ and read in a block of size $L-l-2$ from the disk for the right block.
    3. Enlarge the right block to size $L-l-1$.
    4. Form the superblock from the left and right enlarged blocks.
    5. Diagonalize the superblock, calculate and diagonalize the density matrix.
    6. Transform the basis of the left enlarged block using the eigenbasis created from the density matrix. Use the $m$ largest density matrix eigenvalues. Save the block and basis to disk.
    7. New left enlarged block becomes the left block for the next iteration.
    8. Repeat until the right block becomes a single site.
    9. When the right block is a single site, begin a new sweep with a left enlarged block of two sites.

We can visualize this process by examining the successive block sizes,

- Infinite System run: [B(1,2),B(1,2)] [B(2,4),B(2,4)] [B(3,8),B(3,8)] [B(4,16),B(4,16)] [B(5,24),B(5,24)] [B(6,24),B(6,24)] [B(7,24),B(7,24)]
- Initial sweep: [B(8,24),B(6,24)] [B(9,24),B(5,24)] [B(10,24),B(4,16)] [B(11,24),B(3,8)] [B(12,24),B(2,4)]
- Following sweeps: [B(1,2),B(13,24)] [B(2,4),B(12,24)] [B(3,8),B(11,24)] [B(4,16),B(10,24)] [B(5,24),B(9,24)] [B(6,24),B(8,24)] [B(7,24),B(7,24)] [B(8,24),B(6,24)] [B(9,24),B(5,24)] [B(10,24),B(4,16)] [B(11,24),B(3,8)] [B(12,24),B(2,4)]

The algorithm terminates when convergence is reached. In this case the convergence is defined by a null change in the energy on successive sweeps to a specified decimal place. The first few sweeps of the algorithm do not typically yield accurate results, but to allow a good set of blocks to be used in later sweeps.

### 3.2.3 Measurement of observables

Calculating the ground state energy of a given superblock is an inherent aspect to the algorithm, measuring observables is a more complicated task. The difficulty lies in the change of basis that is performed at each iteration. Since the Hamiltonian is transformed on each iteration, the energy is always accurate to the system. However since the properties of these basis states are not kept every iteration it becomes a challenge to calculate them for any given iteration. Naturally it is possible to store all of the needed information about each observable for each site, such as $\langle S^z|S^z\rangle$, but the computational cost would be unrealistic. There are however methods to calculate observables without having to store and transform information with every iteration, two of which we will review here.

The issue is the basis. With every iteration the basis is expanded well beyond any intuitive nature. The algorithm stores the operators for the rightmost and leftmost sites of the enlarged blocks at every step. However the operators on each site are not transformed with each iteration. Therefore in order to maintain the correct representation of a local operator, the matrix must be transformed and stored every time the basis changes. For example a basis change will need to be performed on $S_i^z$. Similar to the transformation steps performed prior, if $(S_i^z)_j^e$ denotes the $S^z$-operator on site-$i$ of the enlarged block with $j$ sites and $O_j$ is the transformation matrix, the changed operator is,

$$(S_i^z)_j = O_j (S_i^z)_j^e O_j^\dagger \tag{3.2.3.1}$$

The operator is then adjusted for the added site to make the enlarged block,

$$(S_i^z)_{j+1}^e = (S_i^z)_j \otimes I_d \tag{3.2.3.2}$$

These steps allow us to maintain local operators within the current basis. When the superblock is formed from enlarged blocks of equal length, the measurements can then be made by tensorizing the site with the right block and the central sites. This procedure works well for sites close to the middle of the chain, but accuracy of the measurement decreases for sites near the ends of the blocks. This is due to the number of basis changes and truncations performed on those sites.

The above procedure works for local operators but the process of calculating measurements for nonlocal operators (e.g. spin correlations, $C_s = \left\langle S_i^z S_j^z \middle| S_i^z S_j^z \right\rangle$) is more difficult. Assuming the local operators have been transformed, as above, one could simply multiply the operators for the sites when the symmetric configuration is reached. A more accurate approach involves several transformations of the nonlocal operator. To demonstrate this process we will follow a quick example given by Malvezzi [25]. Consider a given system with a symmetric configuration at $L/2 = i + 2$ and $j = i + 1$. The operators at each of these sites are,

$$\begin{aligned}(S_i^z)_{i+2}^e &= (O_{i+1}((O_i(Ib \otimes S^z)O_i^\dagger) \otimes I_d)O_{i+1}^\dagger) \otimes I_b \\ (S_j^z)_{i+2}^e &= (O_{i+1}(I_b \otimes S^z)O_{i+1}^\dagger) \otimes I_d\end{aligned} \tag{3.2.3.3}$$

This gives the spin correlation,

$$(S_i^z S_{i+1}^z)_{i+2}^e = (O_{i+1}((O_i(I_b \otimes S^z)O_i^\dagger) \otimes I_d)O_{i+1}^\dagger)(O_{i+1}(I_b \otimes S^z)O_{i+1}^\dagger) \otimes I_d \tag{3.2.3.4}$$

Unfortantely this equation suffers from accuracy issues. There is another method that offers more accuracy in the calculation, we will touch on the reason for this later, by multiplying the two operators as soon as possible. This allows the entire correlation operator to be transformed as a whole. This operation can be done when the enlarged block is of size $i + 1$, giving,

$$C_s(i, i+1)_{i+1} = O_{i+1}(((O_i(I_b \otimes S^z)O_i^\dagger) \otimes I_d)(I_b \otimes S^z))O_{i+1}^\dagger \tag{3.2.3.5}$$

While these two methods appear equivalent, the second method gives a more accurate calculation of correlations. The method leading to equation (3.2.3.4), involves truncation of states with each iteration so that instead of matrices being multiplied their projectors are. The factor $O_{i+1}O_{i+1}^\dagger$ causes the loss in accuracy. The error compounds the further apart the sites are, with each intermediary site introducing an additional $OO^\dagger$ pair into the equation.

Therefore the second method becomes the preferred calculation as it maintains accuracy. At the start of a DMRG procedure, a list of desired observables must be know so that the appropriate operators can be stored and updated. Additionally we note that measuring correlations across the blocks gives much higher errors than those calculated within the same block and the calculation is only performed once the symmetric configuration is reached. Unlike calculating the energy of the system, which has an associated truncation error, there is no known method to calculate the error of observables. Checking the stability of the results does provide a qualitative idea of the error but merely whether more states are needed for the algorithm.

# Chapter 4

# Spin-½ XXZ Chain with Open Boundary Conditions

This chapter examines and presents results for the spin-½ XXZ Heisenberg chain with open boundaries. Using the spin energy excitation gap, it is shown there is a distinct difference in the first excitation states of chains with periodic and open boundary conditions, a difference not expected to matter at the thermodynamic limit (macroscopic system). Further, an explanation for this phenomenon is found by calculating the local magnetization of the chain and mapping a solution from the tight-binding model. This solution is confirmed by calculating the magnetization of the system in an applied magnetic field. Additionally it shows the effect due to the boundary condition is isolated to the first excitation as the system then realigns with the periodic system for $M = 2$ sector excitation.

## 4.1 On boundary conditions

We will note here that this chapter will focus on the emergent effects of open boundary conditions (OBCs) and further that some conclusions about the properties and physics of the system that might be displayed here will be explored in a later chapter.

As stated previously, the calculations for the given models is most efficient and accurate when the DMRG algorithm is using OBCs. For an excellent numerical study via DMRG which highlights many of the fundamental attributes of $N$-leg spin systems in open boundary conditions see Ramos and Xavier [16]. This study produces ground state energy per site and spin gap results for a number of systems. They also mention the emergent edge effects that occur for these systems, an important property which we will examine in this chapter. An additional study by Ng, Qin and Su show results for spin gap, correlation

data, and local magnetization which presents with oscillations, a characteristic we will see later in this chapter [26].

Effects of various boundary types (open, periodic) have been studied extensively for the spin-½ chain model. See Mikeska and Kolezhuk [27] for a comprehensive chapter on Heisenberg spin chains and ladders in periodic boundary conditions. For interest, treatments of chains with periodic boundaries with an applied twist field can be found here [28] and here [29].

Typically however, these models use periodic boundary conditions (PBCs) when solved analytically. Despite this difference it was assumed the effects of BCs would only appear for finite system sizes and such finite size effects would diminish as system size increased. So the difference should be minimal for systems of a few hundred sites. Thusly the effects of boundary conditions would be negligible in the thermodynamic limit. Such an assumption would also imply that there would be a negligible difference in the observables of the system at this limit. The Hamiltonian for our XXZ spin-½ chain is given in equation (4.1.0.1).

A simple analysis of our principle investigation property, spin gap, on a spin chain shows that the numbers are distinctly different between the two cases for large $\Delta$ (eq. (4.1.0.1)), shown in Figure 4.1, but more importantly that the difference persists independent of system and state size. While this is a well known phenomenon, the reasoning involves the number of excitations or domain walls that can exist in a system given its boundaries, it is not well or explicitly published. However we will investigate it further to be clear about the origin of the phenomenon so to better understand it for the later ladder models.

We define the spin gap as the difference in energy between two states. Here the gap is calculated between the lowest three magnetization sectors, ground state, first excited and second excited.

$$\hat{H} = \frac{J}{2}\sum_{i}^{N-1}(S_i^+ S_{i+1}^- + S_i^- S_{i+1}^+) + \Delta\sum_{i}^{N-1}(S_i^z S_{i+1}^z) \tag{4.1.0.1}$$

$$\Delta_s = \frac{\pi \sinh\Phi}{\Phi}\sum_{-\infty}^{+\infty}\frac{1}{\cosh[(2n+1)\frac{\pi^2}{2\Phi}]} \qquad 0 < \Phi < +\infty \tag{4.1.0.2}$$

The data from the periodic system, matches very well with the analytical solution Eq. 4.1.0.2 (where $\phi$ is an auxilliary phase variable) developed by Cloizeaux and Gaudin [30]. For the the open boundary data, this same calculation deviates significantly with large $\Delta$ from the known solution. It is safe to conclude that the deviation of the OBC data from the known solution is due to the boundary type. Thus, there

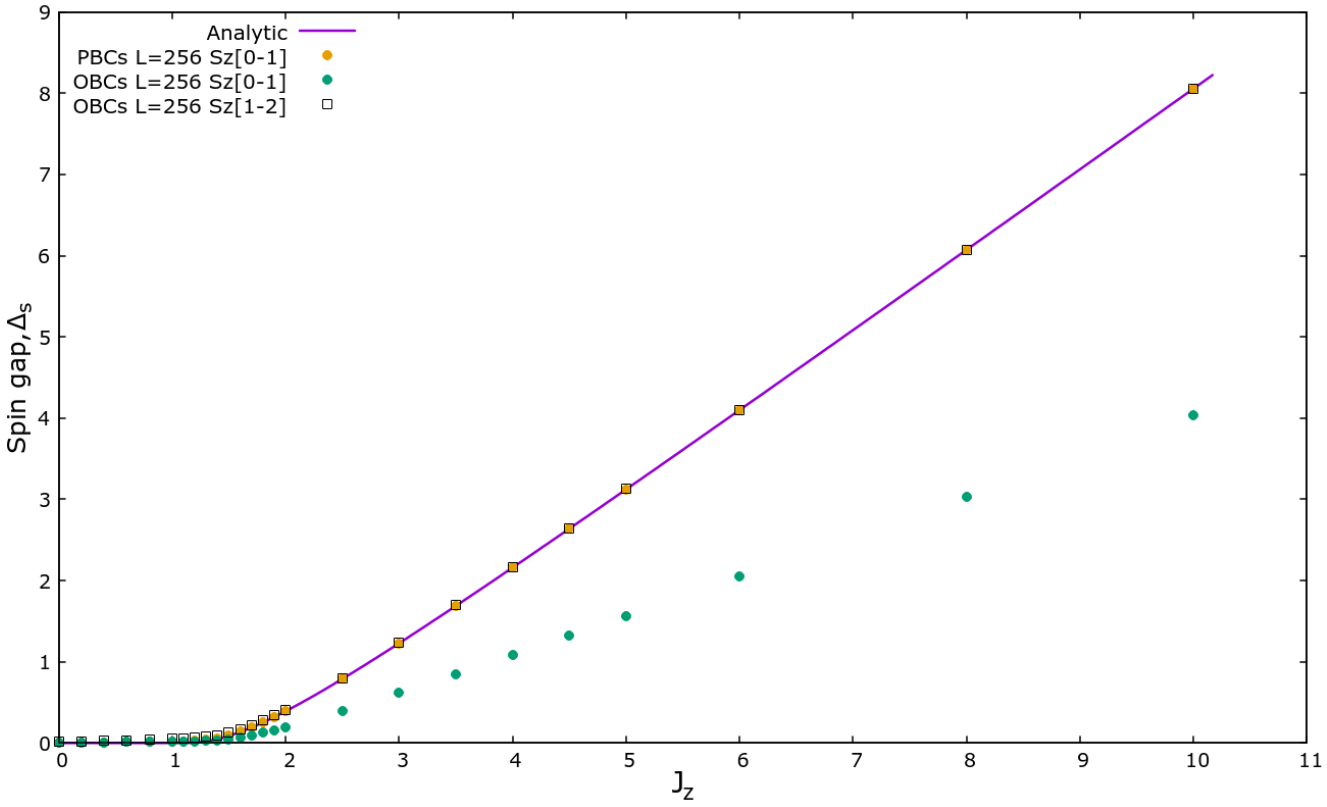


Figure 4.1: Graph of the spin gap $\Delta_s$ as a function of $\Delta$ for $L = 256$ sites with open (OBCs-green dots,black squares) and periodic boundary conditions (PBCs-yellow dots). The analytical solution (blue line) for this model has also been plotted.

must be effects occuring at the boundaries resulting in a different energy gap between the lowest two magnetization sectors. Calculating the gap between the first and second sectors shows a very good match with the periodic and analytic data. This boundary effect only seems to occur for the first excitation and doesn't carry into the higher excitation states. This suggests that introducing two excitations into the OBC chain is the equivalent to a single excitation in the PBC chain.

The next step is to understand this phenomenon mathematically by calculating the energy of the ground state and the first excited state for each boundary type. Since the deviation is most drastic for $\Delta >> 0$ (AFM), the calculation is done in this limit. Therefore the ground state of the system is the Néel state, an alternating pattern of up and down spins. Such a ground state (i.e. lowest energy state) has two possible configurations, each with the same energy:

$$\begin{matrix} \uparrow\downarrow\uparrow\downarrow\uparrow\downarrow \\ \downarrow\uparrow\downarrow\uparrow\downarrow\uparrow \end{matrix} \tag{4.1.0.3}$$

An excitation is introduced by flipping one of the spins has at an energy cost that clearly depends on the boundary type, per the results in figure 4.1.

To understand this conclusion better we start with a pure Néel ground state with energy $E = 0$, see Table 4.1. A single excitation is introduced in the system by flipping a single spin in the bulk of the system. The energy of the excitation is calculated in both boundary conditions and found to be $\Delta/2$ in both cases. A single excitation consists of 2 spinons, initially next to each other. Since the spinons are not bound together, which would make an spin-1 magnon, they can move through the system separately. This results in two domain walls in the lattice. These spinons can move through the lattice without an energy cost, so we move them such that one domain wall is on the edge and the second one exists between the two edges. Since the two edges interact in the periodic system the energy of the excitation hasn't changed. However as the edges don't interact in the open system, the second domain wall (i.e. spinon) has been rotated out of the system and the energy is now $\Delta/4$. So the lowest energy excitation is OBCs is a single spinon, having half the energy of the two spinons in the periodic system.

Therefore the change in energy between the ground state and the first excitation state is $\Delta$ and $\Delta/2$ for periodic and open boundary systems, respectively, when accounting for all of the spins. Interestingly this single site of additional energy in OBC can exist anywhere in the system not only at the edges due to the rotation of spins at no energy cost. However due to PBC technically this edge excitation is the same energetically as an excitation in the bulk. Physically these excitations act as 'domain walls' which are interfaces between different magnetic moments or domains. The 'edge' excitation seen in the OBC system is a single domain wall. The 'bulk' excitation however has two walls. The difference being that because the two spins are the same on the edges, the periodic boundary creates what is the second wall.

## 4.2 Magnetization

We can then ask the question, why is there a difference in the energy gap? From a different but equal viewpoint if we have a very long material that is subjected to a transverse magnetic field, what is happening on the edges should be negligible compared to the bulk, yet these edge effects are changing

| | | Energy | |
|---|---|---|---|
| States | Physical | PBCs | OBCs |
| G.S. (Néel) | ↑↓↑↓↑↓ | 0 | 0 |
| 2 excs. (PBC,OBC) | ↑↓↑↑↑↓ | $\frac{\Delta}{2}$ | $\frac{\Delta}{2}$ |
| 2 excs. (PBC), 1 exc. (OBC) | ↑↓↑↓↑↑ | $\frac{\Delta}{2}$ | $\frac{\Delta}{4}$ |

Table 4.1: Table detailing the energies of the ground state and bulk/edge excitations, in the large $\Delta$ limits for PBCs and OBCs. The PBCs calculations is for 3 spins. The OBCs calculations is for 2 and 3 spins, reasoned in the text.

| | Spin Gap, $\Delta_s$ | |
|---|---|---|
| Sectors | PBCs | OBCs |
| M=[0,1] | $\Delta$ | $\frac{\Delta}{2}$ |
| M=[1,2] | $\Delta$ | $\Delta$ |

Table 4.2: Table detailing the Spin gap, $\Delta_s$, for PBCs and OBCs for different excitations.

the energy of the system. Calculating the average magnetization at each site, Figure 4.2, illustrates the emergence of these effects in the $M = 1$ magnetization sector. It also demonstrates the null magnetization in the ground state sector which lies on the $x$-axis, as well as the bulk magnetization in the $M = 2$ sector where the total spin of the system is 2 The first magnetization sector reveals non-zero magnetization, maximized near the edges, decreasing towards the middle of the chain. While it is known that open boundary conditions on a spin-½ chain causes effects at the edges there is little rigorous material on the subject. As shown in Figure 4.2, the local average magnetization shows peaks at the chain ends for the non-zero sectors. In the following paragraphs we show that these experimental results can be derived analytically.

### 4.2.1 Local average magnetization

In this section the local average magnetization will be derived analytically. Firstly an equal probability of states solution is proposed then a more accurate probabilistic solution is derived. The initial derivation gives equal weight to the excitation states while the latter solution factors in the probabilistic nature of quantum states. The local average magnetization, $\langle S_j \rangle$, is the average value that a spin will have at any given site for a set of states. A single spinon can be created in a system with open boundary conditions by rotating all of the spins to the right of the initial excitation, eliminating the second domain wall.

$$\uparrow\uparrow\downarrow\uparrow\downarrow\uparrow \quad \Longrightarrow \quad \uparrow\downarrow\uparrow\uparrow\downarrow\uparrow \quad \Longrightarrow \quad \cdots \quad \Longrightarrow \quad \uparrow\downarrow\uparrow\downarrow\uparrow\uparrow \tag{4.2.1.1}$$

The rotation of all spins to the right of the initial excitation is allowed because there is no energy cost. This essentially moves to the second domain wall 'between' the ends of the chain. There is no cost because all of the spins are being rotated, in essenece we are simply moving one of the spinons to a different location, see equation (4.2.1.1). There is no favorable lower energy when the two spinons are next to each other. This type of rotation only works for open boundary conditions since a second domain wall would still occur with periodic boundary conditions, it has just been moved to a different site.

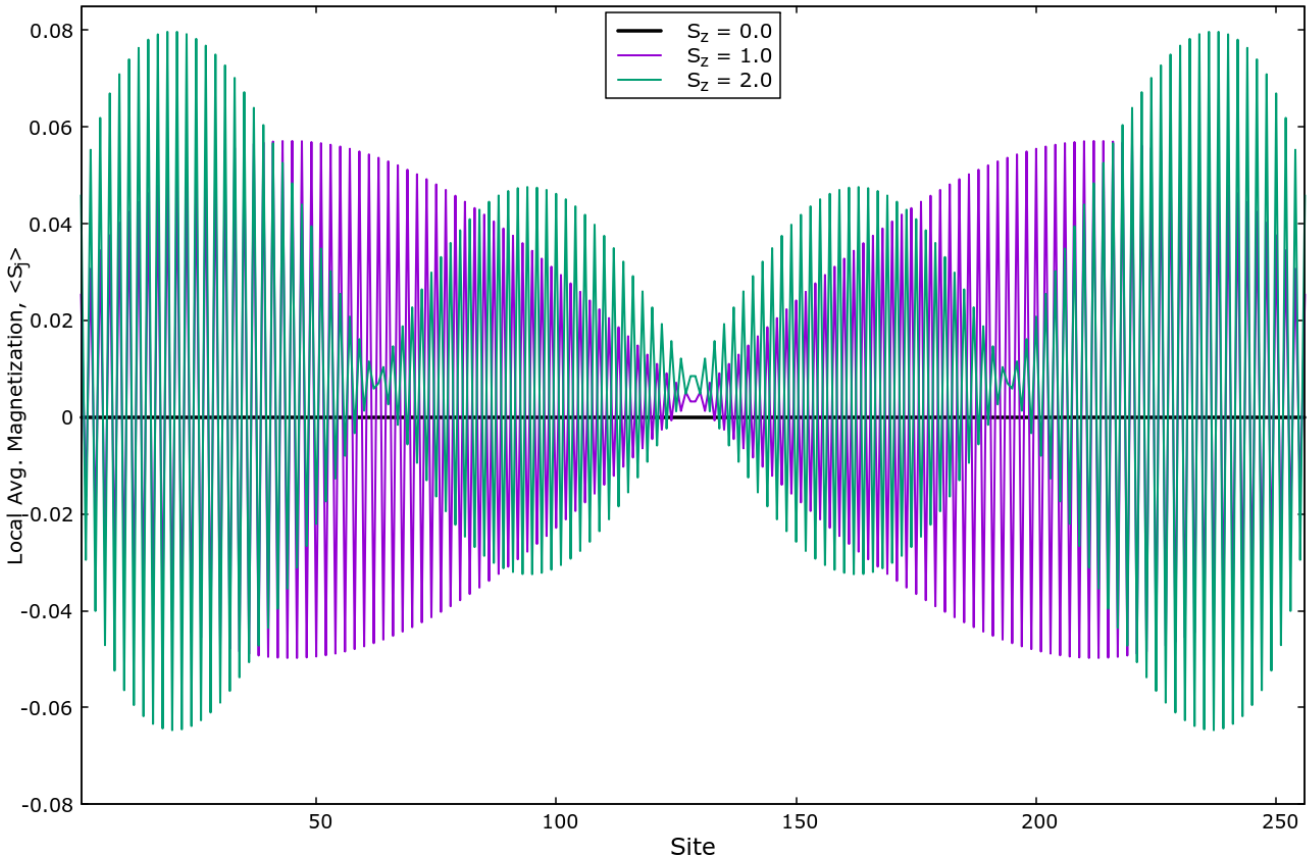


Figure 4.2: Graph of the local average magnetization $\langle S_j \rangle$ for antiferromagnetic Heisenberg XXZ spin-½ chain magnetization sectors $M = [0, 1, 2]$. $M = 0$ (black, on the $x$-axis), $M = 1$ (blue), $M = 2$ (green). $L = 256$ $J_{xy} = 1$ $J_z = 10$. DMRG data.

For the purpose of this magnetization calculation the excitations in table 4.3 are labeled accordingly. These states are for an $L = 6$ site chain in a large $\Delta$ limit.

Note that these states are not eigenstates of the Hamiltonian, unless the system is in the Ising limit in which case these states have the same energy. Moving just off the Ising limit causes this degeneracy to be lifted resulting in different energies for each state. This calculation will start by assuming the full Ising limit so they all states have the same energy and there is equal probability of the system being in any of the states.

| $\rho$ | exc. state |
|---|---|
| 1 | $\uparrow\uparrow\downarrow\uparrow\downarrow\uparrow$ |
| 2 | $\uparrow\downarrow\uparrow\uparrow\downarrow\uparrow$ |
| 3 | $\uparrow\downarrow\uparrow\downarrow\uparrow\uparrow$ |

Table 4.3: Table of excitation states of an $L = 6$ site chain.

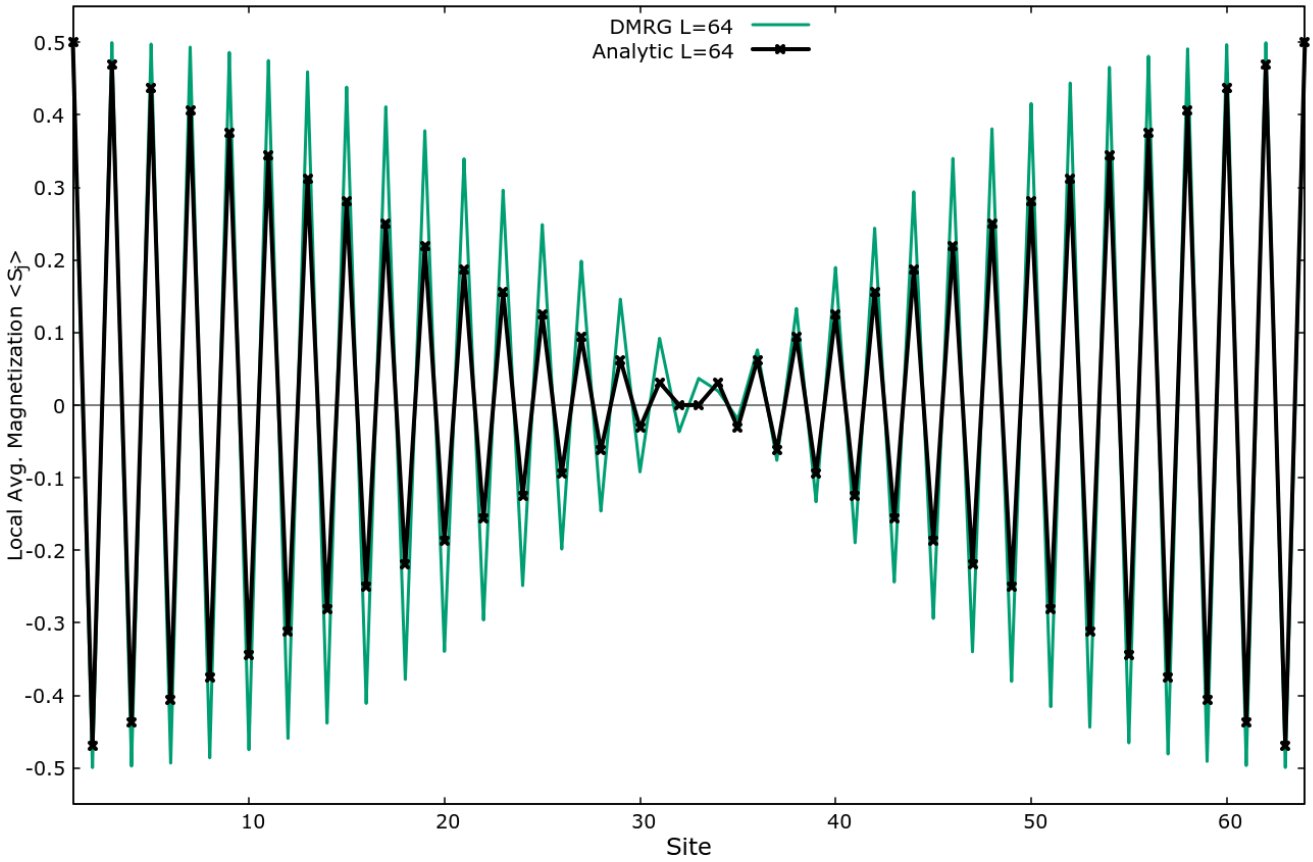


Figure 4.3: Graph of the non-probabilistic analytical solution (black) and DMRG (green), Eq. (4.2.1.5), for local average magnetization $\langle S_j \rangle$ for a Heisenberg XXZ spin-½ chain. $M = 1$. $L = 64$, $J_{xy} = 1$, $J_z = 10$.

**Equal Probability solution**

In the perfrect Ising limit the number of possible excitation states is half the number of sites, ½. We define, quite simply then, the total number of possible states as $N$ and any given state within this discrete set as $\rho$. So the average magnetization of site $j$ where $1 \geq j \geq L$, summed over each state $\rho$ in the set of states $N$, with spin $S$, is given by equation (4.2.1.2).

$$\langle S_j \rangle = \frac{1}{2N} \sum_{\rho=1}^{N} S_j^{(\rho)} \tag{4.2.1.2}$$

The current spin value for any site $j$ in any of the states can be described,

$$S_j = \frac{1}{2} \begin{cases} -(-1)^j & \text{if } j < 2\rho \\ (-1)^j & \text{if } j \geq 2\rho \end{cases} \tag{4.2.1.3}$$

Using the cases in Eq. (4.2.1.3), the summation in Eq. (4.2.1.2) can be expanded for all states in $N$

to give,

$$\langle S_j \rangle = \frac{1}{L}(-1)^j \begin{cases} \frac{j}{2} - [\frac{L}{2} - (\frac{j}{2}+1) + 1] & \text{if } j_{even} \\ \frac{j-1}{2} - [\frac{L}{2} - \frac{j+1}{2} + 1] & \text{if } j_{odd} \end{cases} \tag{4.2.1.4}$$

Which simplifies to,

$$\langle S_j \rangle = (-1)^j [\frac{j}{L} - \frac{1}{2}] - \delta$$
$$\delta = \begin{cases} 0 & \text{if } j_{even} \\ \frac{1}{L} & \text{if } j_{odd} \end{cases} \tag{4.2.1.5}$$

For a given system size of $L$, Equation (4.2.1.5) produces the plot in Figure 4.3 for local average magnetization $\langle S_j \rangle$ as a function of lattice site $j$.

This approximation however, doesn't match well with the experimental data, Fig. 4.3. A more accurate analytic process accounts for the calculated probabilities of the system being in a given excitation state. That is to say that the system has a higher probability of being in certain states than others.

**Probabilistic Solution**

In context, this means the model is no longer perfectly Ising. Not all of the excitation states have the same energy. Thus a new sum is evaluated that factors in the probability density of each excitation state. Quantum mechanics defines the probability density of a given state as the absolute square of that state wavefuntion, $|\psi_\rho|^2$. So the local average magnetization becomes,

$$\langle S_j \rangle = \sum_{\rho=1}^{\frac{L}{2}} S_j^{(\rho)} |\psi_\rho|^2 \tag{4.2.1.6}$$

Reiterating the current spin value for a given site $j$ from Eq. 4.2.1.3,

$$S_j^{(\rho)} = \frac{1}{2} \begin{cases} (-1)^j & j \geq 2\rho \\ -(-1)^j & j < 2\rho \end{cases} \tag{4.2.1.7}$$

Starting again with the excitation states as defined in Table 4.3, described now as kets.

$$|\psi_1\rangle = \uparrow\uparrow\downarrow\uparrow\downarrow\uparrow$$
$$|\psi_2\rangle = \uparrow\downarrow\uparrow\uparrow\downarrow\uparrow \tag{4.2.1.8}$$
$$|\psi_3\rangle = \uparrow\downarrow\uparrow\downarrow\uparrow\uparrow$$

A given system state can be described as a 1D vector of $P$ dimensions where $P = 2^L$, and $L$ is the number of sites. There are $N = {}^L/_2$ first excitation states for such a system where each excitation state is given by $|n\rangle$ and $n$ has the condition $n = 1, 2...N$. The objective now is to find the excitation eigenfunctions, $\psi_i$, of this system. They are found by solving the eigenvalue equation 4.2.1.9.

$$\hat{H}\,|\psi_n\rangle = E_n\,|\psi_n\rangle \tag{4.2.1.9}$$

A good approximation for this system in the large $\Delta$ limit is a tight binding model. In this model the electrons are tightly bound to their constituent atoms with limited interaction to surrounding electrons. The calculation uses an approximate set of superpositioned wave functions to solve the system.
This approximation provides a good starting Hamiltonian to begin the derivation. Additionally, by confining this mapping to the lattice, i.e. an infinite well where the potentials are placed at the ends of the lattice, boundary conditions can be established. The tight binding Hamiltonian is given by,

$$\begin{aligned} \hat{H} &= -t \sum_{\langle i,j\rangle\sigma} (c^+_{i,\sigma} c_{j,\sigma} + c_{i,\sigma} c^+_{j,\sigma}) \\ t &= \left\langle \psi_i | \hat{H}^{xy} | \psi_j \right\rangle \\ \hat{H}^{xy} &= \frac{1}{2} \sum_{\langle i,j\rangle} (S^+_i S^-_j + S^-_i S^+_j) \end{aligned} \tag{4.2.1.10}$$

where $t$ is the hopping term for the excitations moving between adjacent sites and the second quantization operators act on these excitations. Here $i$ and $j$ represent lattice sites always adjacent to each other, signified by the brackets $\langle\rangle$. The $\sigma$ term represents the polarization of the spin, in this case $\uparrow$ or $\downarrow$. The $S^z$ operator does not factor in as it doesn't exchange spins.
A solution for the tight-binding model is the Bloch wave function [31], which describes electronic states on a periodic lattice. This function has the form,

$$\left|\psi^{(k)}_j\right\rangle = \frac{1}{\sqrt{L}} \sum_{j=1}^{L} (Ae^{ikaj} + Be^{-ikaj})\,|j\rangle \tag{4.2.1.11}$$

Boundary conditions dictate that the wavefunction must be 0 at the chain ends such that,

$$\psi^{(k)}_0 = \psi^{(k)}_L = 0 \tag{4.2.1.12}$$

and therefore $A = -B$ which reduces equation (4.2.1.11) to,

$$\left|\psi_j^{(k)}\right\rangle = \sum_j^L A(e^{ikaj} - e^{-ikaj}) \left|j\right\rangle \tag{4.2.1.13}$$

Euler and trigonometric formulae transform this sum (eq. (4.2.1.13)) from exponential terms to sinusoidal terms. As the excitations are constrained to the confines of the lattice (i.e. an infinite potential well) it becomes more convenient to use sinusoidal functions rather than exponentiation anyway. So we use,

$$\left|\psi_j^{(k)}\right\rangle = A\sum_{j=1}^L \sin kaj \left|j\right\rangle \tag{4.2.1.14}$$

Using boundary conditions again to solve for $k$ where $m = 1, 2, 3, 4 \ldots$,

$$k = \frac{m\pi}{(N+1)}, N = La \tag{4.2.1.15}$$

A better visualization of this sum is as a vector,

$$\left|\psi_j^{(k)}\right\rangle = A \begin{pmatrix} \sin k \\ \sin 2k \\ \sin 3k \\ \vdots \\ \sin Lk \end{pmatrix} \tag{4.2.1.16}$$

Now that we've established the excitation wavefunction the next step is to solve for the normalization constant $A$ by squaring or taking the inner product of the states, $\left\langle\psi_j^{(k)}\middle|\psi_j^{(k)}\right\rangle$. The constant $A$, which is a function of $k$, is then,

$$A_k = \sqrt{\frac{1}{\frac{L}{2} - \frac{1}{2}\csc k \sin kL \cos\left(k(L+1)\right)}} \tag{4.2.1.17}$$

Such that the full wavefunction is,

$$\left|\psi_j^{(k)}\right\rangle = \sqrt{\frac{1}{\frac{L}{2} - \frac{1}{2}\csc k \sin kL \cos\left(k(L+1)\right)}} \sum_{n=1}^L sin(kj) \left|j\right\rangle \tag{4.2.1.18}$$

Equation (4.2.1.18) gives the final normalized wavefunction for the system. Returning to equations

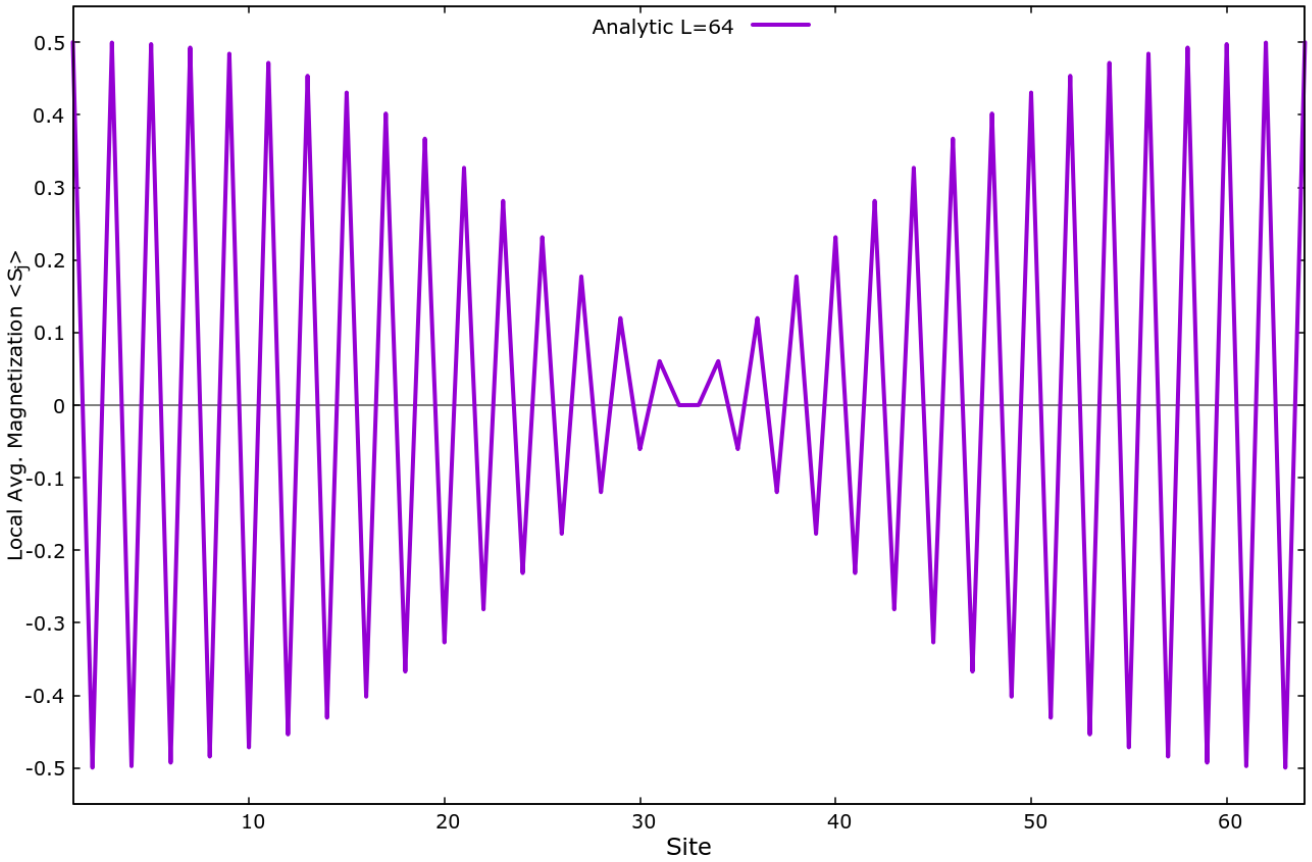


Figure 4.4: Graph of the probabilistic analytical solution (green) of the local average magnetization $\langle S_j \rangle$ for a Heisenberg XXZ spin-½ chain. $M = 1$. $L = 64$.

(4.2.1.6) and (4.2.1.7) to put all of the pieces back together gives,

$$\langle S_j \rangle = \frac{(-1)^j}{2} A^2 [\sum_{j \leq \frac{i}{2}}^{L} \sin^2 kj - \sum_{j > \frac{i}{2}}^{L} \sin^2 kj] \tag{4.2.1.19}$$

Eq. (4.2.1.19) gives a probabilistic approximation of the local average magnetization of a spin-½ linear chain in the first ($M = 1$) magnetization sector, the conclusion to the derivation. We can see in Figure 4.4 that the magnetization oscillations are now curved, very similar to the experimental data.

In the $M = 1$ magnetization sector the parameter $k$ has a value $k = \frac{\pi}{(N+1)}$ which results in a good match between this analytical analysis and the experimental data, for a given system size, Fig. 4.5.

### 4.2.2 Magnetization

What has so far been shown in this chapter is a seeming paradox. How can a measureable thermodynamic quantity be independent of system size but dependent on boundary conditions? The resolution to this

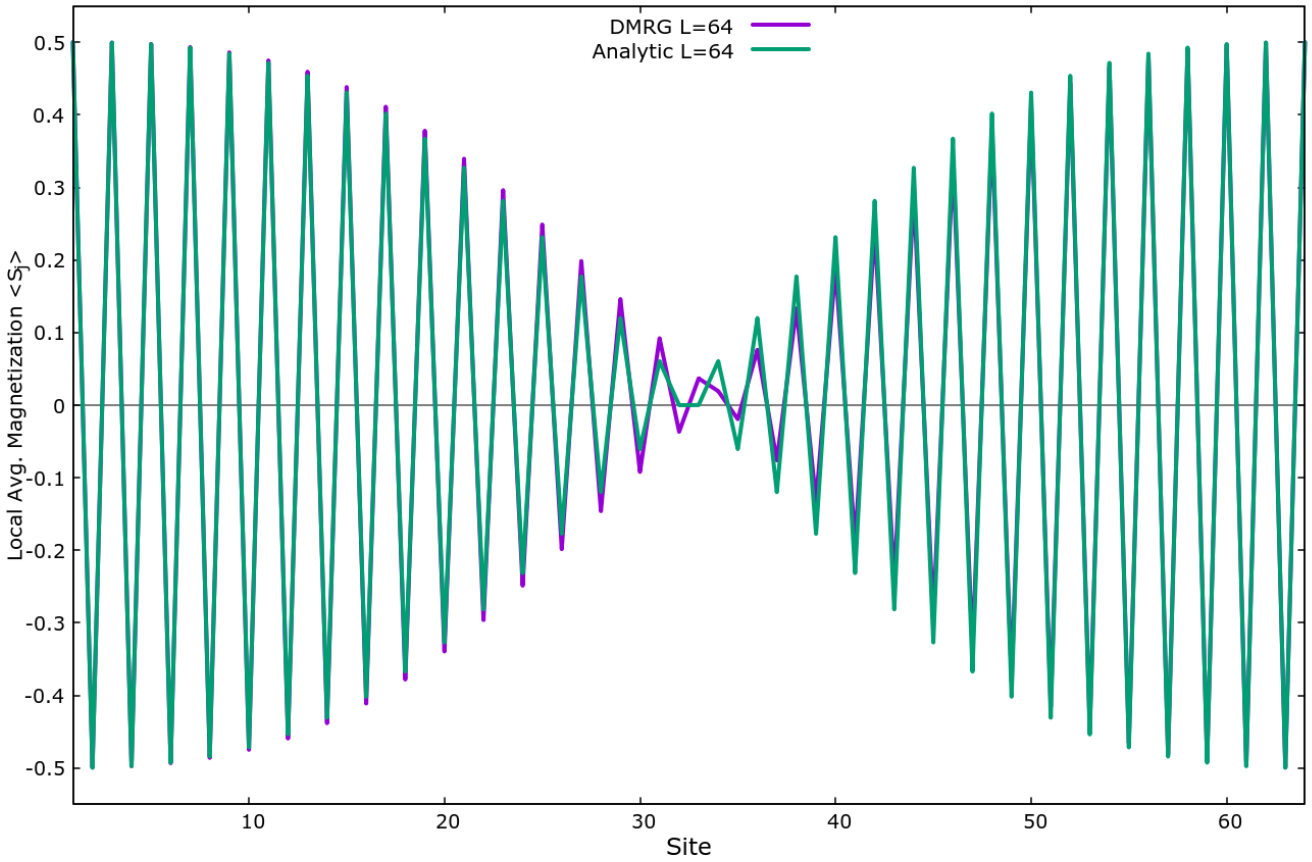


Figure 4.5: Graph comparing the experimental (DMRG OBCs blue) and analytical (green) solutions for local average magnetization $\langle S_j \rangle$ of an Heisenberg XXZ spin-½ chain. $M = 1$. $L = 64$ $J_{xy} = 1$ $J_z = 10$.

paradox will be presented in this subsection by examining the magnetization of the system[1]

Now that the edge effects have been described analytically, it is necessary to demonstrate experimentally the difference in energy required to induce a singular excitation in each boundary type. This will be done by applying an external magnetic field to the chain and calculating the strength of the field required to change the magnetization of the system. The equation for the total energy of the system with an applied magnetic field is given by,

$$E(H) = E_m - HM \tag{4.2.2.1}$$

where *E(H)* is the energy of the system as a function of $H$, $E_m$ is the energy of the system in the *Mth* magnetization sector (the energy of spin interactions when $H = 0$), and $M$ is the magnetization sector. The factor $-HM$ is the energy of the interaction of the spins with the external magnetic field $H$.

[1]I reiterate, again, that this is a known phenomenon but this investigation was a key part of this thesis project and provides an explanation that is seemingly lacking in the literature.

The magnetization sector is the total spin $S$ of the system.

$$M = \sum_{i=0}^{N} S = 0, 1, 2, 3...N \tag{4.2.2.2}$$

This calculation shows the energy required to induce a system from one magnetization sector to another. The essence of the physics here is to apply an external magnetic field and measure the energy of the system in a given magnetization sector. The field strength for the first sector should noticeably differ between boundary types because, as was shown in section 4.1, a single excitation in PBCs is two spinons while in OBCs this is only one spinon. In the full Ising limit the energy of the system with an applied magnetic field $H$ in periodic and open boundary conditions are,

$$\begin{aligned} E(H)_{PBC} &= \Delta M - HM \\ E(H)_{OBC} &= \Delta(M - \frac{1}{2}) - HM \end{aligned} \tag{4.2.2.3}$$

The $-1/2$ in the OBC equation (4.2.2.3) recounts the results from section 4.1 stating that the gap in OBCs is half the gap for PBCs. It is simple to show then the point (i.e. magnetic field strength) at which two given sectors have the same energy. More clearly, how much energy is required to introduce an excitation is in essence the field strength $H$.

$$H = E_M - E_{M-1} \tag{4.2.2.4}$$

For all M in PBCs,

$$H_{PBC} = \Delta \tag{4.2.2.5}$$

However for OBCs,

$$\begin{aligned} M[0-1] \qquad & H = \frac{\Delta}{2} \\ M[p-q] \qquad & H = \Delta \end{aligned} \tag{4.2.2.6}$$

where $p \geq 1$, $q = p + 1$.

This demonstrates quite clearly the effect of the boundary conditions. In PBCs a field strength of $H_{PBC} = \Delta$ is needed to introduce a single excitation (two domain walls) for each magnetization sector. For OBCs the field strength to energetically align (i.e. make degenerate) the ground and first sectors ($M = 0$ and $M = 1$) is half the PBC value at $H_{OBC} = \Delta/2$. However the field strength realigns with the PBC value for any adjacent sector gap greater than $M = 1$.

However the real system isn't in the perfect Ising limit so the field strength won't be the same for

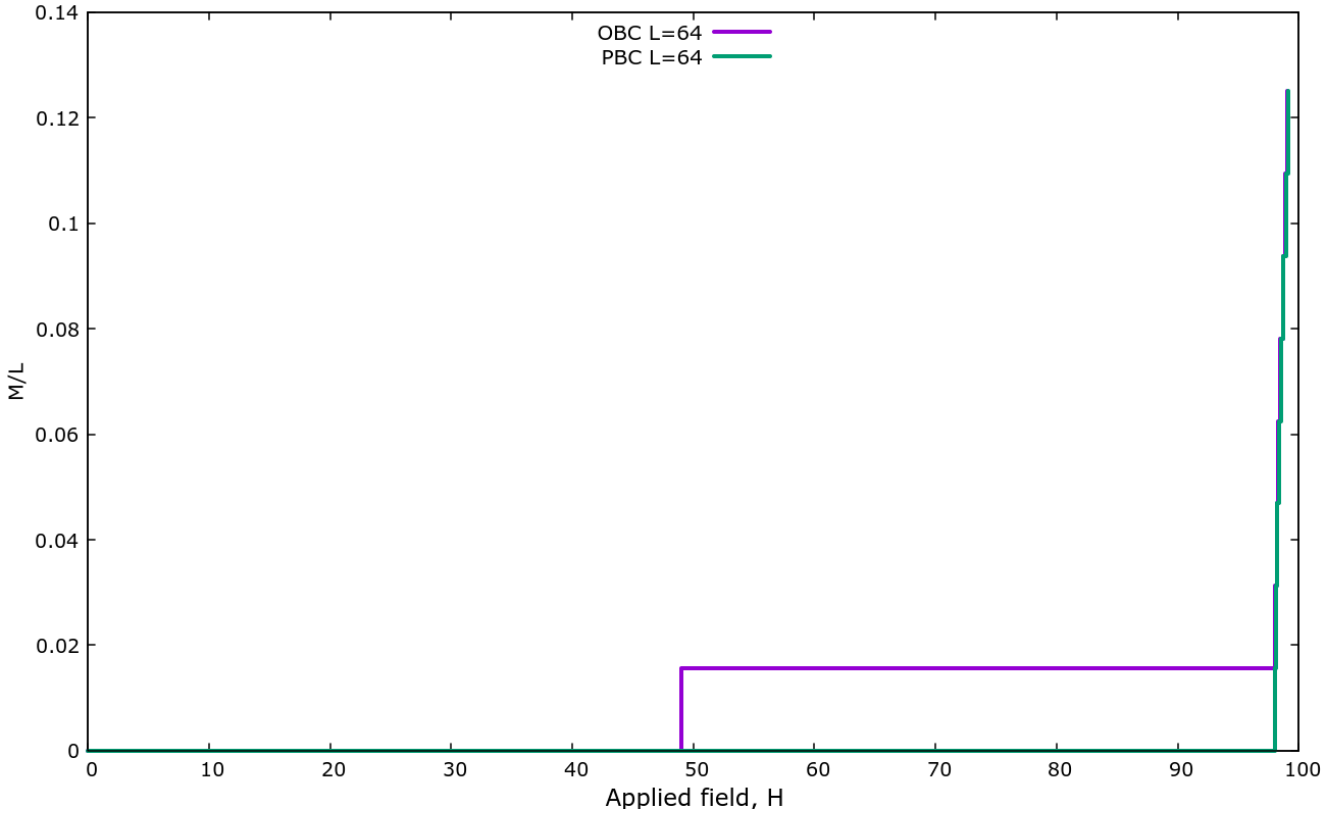


Figure 4.6: Graph of the magnetization per site $^{M}/_{L}$ as a function of applied field $H$. PBCs and OBCs of a Heisenberg XXZ spin-½ chain. $L = 64$. $J_{xy} = 1$, $J_z >> 1$.

every gap (i.e. $H = \Delta$). More importantly it shows that the edge effects allow for the introduction of a single spinon in an OBC system. Figure 4.6 shows a DMRG calculation for a near Ising limit system (strong $\Delta$ limit). By graphing the magnetization $M$ against applied field $H$ it is easy to see that the magnetization "jumps" in steps to the next sector.

As predicted we see a marked difference in the field strength for the initial excitations between the boundary types. The data shows that the field strength is about half for the first excitation for open boundary conditions compared to periodic boundary conditions. This result is also seen in the spin gap plot Fig. 4.1. For macroscopic magnetization, large $M$, these curves join up in the perfect Ising limit. However away from this limit they don't match exactly, a result which can be seen in figure 4.7. The reason for this is the additional effects from the other couplings when the system is not fully Ising.

As stated the field strength to magnetize an OBC chain to the first sector is half that required for a PBC chain. This is an interesting result because it is independent of system size. However it does appear to depend on boundary conditions which goes against the basic idea of thermodynamics, in that as the system size tends to infinity the measureable quantities should become independent of the conditions at the boundaries. So it seems naive to find these results to be correct, especially since these are only

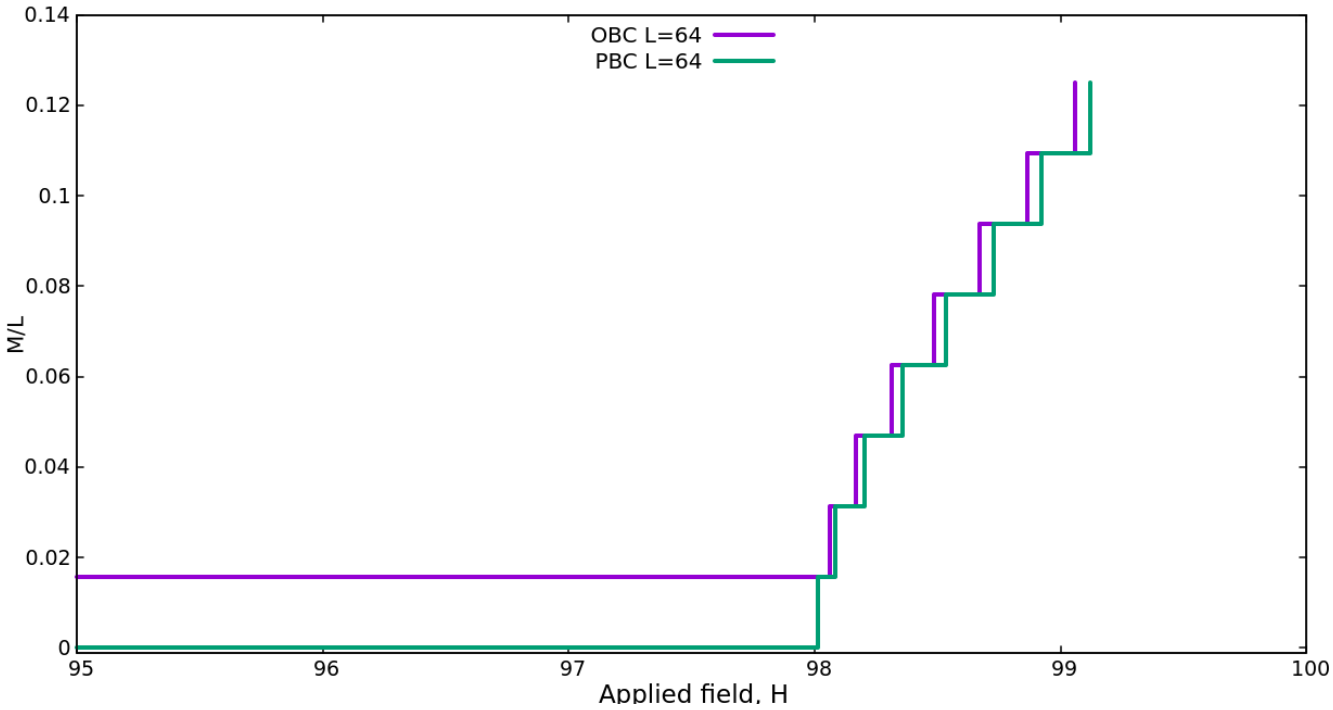


Figure 4.7: Graph of the magnetization per site $^{M}/_{L}$ as a function of applied field $H$. PBCs and OBCs of a Heisenberg XXZ spin-½ chain. $L = 64$. $J_{xy} = 1$, $J_z >> 1$. Zoomed to show inexact alignment.

effects occuring at the edges and not edge states which is an important point. However the reason this is not necessarily a curious result is because this deviation in spin gap is only for a single excitation, a well known result and conclusion, see [2]. Creating a macroscopic number of excitations, magnetizing the sample, reveals the boundary conditions to be irrelevant again. And therefore the resolution to this seeming paradox is as shown in equation (4.2.2.3) and figure 4.6, that although the critical field $H$ depends on the boundary conditions, the magnetization ($^{M}/_{L}$) does not.

# Chapter 5

# Isotropic Heisenberg Ladder

Now we turn to the main topic of the thesis, the Heisenberg spin ladder. Firstly we will examine the isotropic case for which there are known results. Some of these results will be reproduced here. The primary subject matter of this investigation is the phase diagram of the ladder. This examination will be done by looking at the spin gap because certain phase boundaries occur when specified gaps go to zero.

Initially we just consider the full isotropic Heisenberg exchange on the rungs ($J_\perp^{xy} = J_\perp^z = J_\perp$). This 2-leg ladder model acts as a good medium to study the crossover between a gapless spin-½ chain regime and a gapped spin-1 chain. This crossover is one of the most studied and discussed phase transitions in condensed matter, occuring at $J_\perp = 0$. At this point the system becomes 2 decoupled spin-½ chains. When $J_\perp$ is large and antiferromagnetic ($>> 0$) the system mimics a set of gapped spin-½ rung-singlets. In the opposite limit, $J_\perp$ is large and ferromagnetic ($<< 0$), the rungs form spin-1 triplets giving an effective spin-1 chain which should exhibit an excitation gap, more commonly refered to as the Haldane gap. An effective model will be constructed to better understand this phase and its properties. A strong rung coupling analysis will be discussed here. A weak coupling analysis will be discussed in the next section in a more general anisotropic model, building on work done be Shelton, Nersesyan and Tsevlik [8].

The isotropic 2-leg ladder Hamiltonian is given by,

$$\begin{aligned}\hat{H} = J_\parallel \sum_{j,n=1,2}^{L} (S^+_{j,n}S^-_{j+1,n} + S^-_{j,n}S^+_{j+1,n} + S^z_{j,n}S^z_{j+1,n}) \\ + J_\perp \sum_{j}^{L} (S^+_{j,1}S^-_{j,2} + S^-_{j,1}S^+_{j,2} + S^z_{j,1}S^z_{j,2})\end{aligned} \tag{5.0.0.1}$$

The top line in Eq. (5.0.0.1) describes the intra-leg contribution with couplings $J_\parallel$ and the bottom line

| explicit form | Energy | Degeneracy |
|---|---|---|
| $\|\uparrow\uparrow\rangle$ | | |
| $\frac{1}{\sqrt{2}}(\|\uparrow\downarrow\rangle + \|\downarrow\uparrow\rangle)$ | $\frac{J_\perp}{4}$ | Triplet |
| $\|\downarrow\downarrow\rangle$ | | |
| $\frac{1}{\sqrt{2}}(\|\uparrow\downarrow\rangle - \|\downarrow\uparrow\rangle)$ | $-\frac{3J_\perp}{4}$ | Singlet |

Table 5.1: State space of 2-spin system.

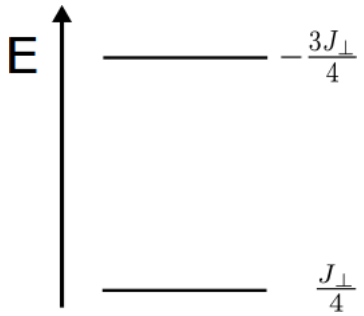


Figure 5.1: Energy levels of 2-spin system with triplet ground state.

calculates the inter-leg (rungs) contribution with couplings $J_\perp$. Antiferromagnetic interaction is favored for positive coupling strengths ($J_\alpha > 0$) and ferromagnetic interactions are favored for negative couplings ($J_\alpha < 0$). Setting the leg coupling $J_\parallel$ to 1 fixes the energy scale. Varying the rung coupling from positive to negative then allows access to the rung-singlet and effective spin-1 chain (Haldane) phases respectively.

We will first start by examining the ferromagnetic case, which can be modeled as an effective spin-1 chain, by constructing the effective spin-1 operators and computing the consequences of the effective Hamiltonian. Since we will be working in the strong coupling regime examining a series of 2-spin systems, the states for this system are reiterated here, table 5.1.

## 5.1 Ferromagnetic regime

In the strong ferromagnetic rung regime ($J_\perp < 0$) the rungs form a triplet ground state. The ground state is, naturally, a series of rung-triplets. These triplet states have a total spin of 1, see table 5.1, in essence making them spin-1 particles. The system is then a rung-triplet ground state with a higher energy singlet state, figure 5.1.

In effect the ferromagnetic case creates an integer spin chain which will show different properties than the spin-½ chain, more specifically the emergence of the Haldane excitation gap. This phase has been shown to occur using Monte Carlo methods [32, 33] and numerical diagonlizations [34]. As we are not dealing with true spin-1 particles, an effective representation needs to be built to further understand the

$$\begin{array}{lcl} |\uparrow\uparrow\rangle & \rightarrow & |\Uparrow\rangle \\ \frac{|\uparrow\downarrow\rangle+|\downarrow\uparrow\rangle}{\sqrt{2}} & \rightarrow & |0\rangle \\ |\downarrow\downarrow\rangle & \rightarrow & |\Downarrow\rangle \end{array}$$

Table 5.2: Table showing effective transformation of rung-triplet states to spin-1 states.

physics of the strong ferromagnetic regime. In the following subsection we will briefly discuss integer (Haldane) spin physics in the context of this thesis and construct the effective Hamiltonian that will provide a theoretical basis to check against later results.

### 5.1.1 Effective Hamiltonian

Given a strongly ferromagnetic rung coupling, more precisely $J_\perp > J_\parallel$, the system becomes a series of weakly coupled rungs. The rungs can be then handled individually, each consisting of 2 spins forming a triplet ground state. In essence this creates a single site with spin-1 degrees of freedom, forming an 'effective' antiferromagnetic spin-1 chain. Haldane [7] proposed integer-spin antiferromagnetic Heisenberg spin chains have a finite spin gap ($\Delta_H = 0.41052$), later confirmed rigorously [11]. It is the mapping to this spin-1 chain that makes it Haldane physics which we use to understand the properties of the ladder in this phase.

Firstly, the rung sites are coupled together in the triplet states and transformed to a single particle kets, table 5.2.

The arrows in the kets on the left hand side represent the spin on each leg for a given rung. For clarity the first arrow corresponds to the the spin on leg-1 and the second arrow to leg-2. So then the Hamiltonian for the $S^z$ operator becomes a sum of nearest neighboring rungs such that,

$$\hat{H}_z = (S^z_{1,i} S^z_{1,i+1} + S^z_{2,i} S^z_{2,i+1}) \tag{5.1.1.1}$$

$$\begin{aligned} \hat{H}_z \,|\Uparrow\Uparrow\rangle &= \frac{1}{2}\,|\Uparrow\Uparrow\rangle \\ |\Downarrow\Downarrow\rangle &= \frac{1}{2}\,|\Downarrow\Downarrow\rangle \\ |\Uparrow\Downarrow\rangle &= -\frac{1}{2}\,|\Uparrow\Downarrow\rangle \\ |\Uparrow 0\rangle &= (|\Uparrow s\rangle - |\Uparrow s\rangle) = 0 \\ \vdots \qquad & \qquad \vdots \end{aligned} \tag{5.1.1.2}$$

Using this set of results the effective $z$-component coupling is derived for the effective Hamiltonian.

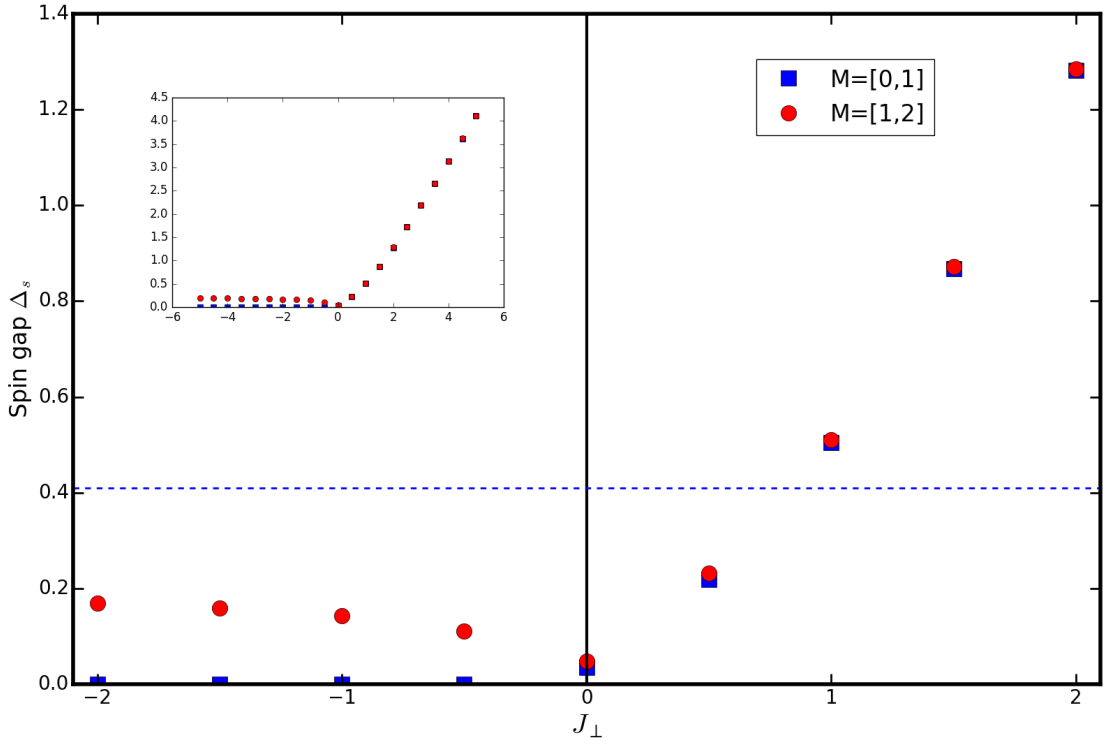


Figure 5.2: Graph of the spin gap $\Delta_s$ as a function of the isotropic rung coupling $J_\perp$. Inset shows the same data over a larger coupling space. The data shows DMRG data for $M = [0, 1]$ sector gap (blue squares) and $M = [1, 2]$ sector gap (red circles). For reference the full Haldane gap is included (blue dashed). $L = 100$, $J_\parallel = 1$.

Here the ket $|s\rangle$ represents the singlet state which is a part of the high energy manifold. Comparing the spin-½ and spin-1 $S^z$ operators to see the changes,

$$\begin{aligned} S = \frac{1}{2} \qquad S^z|\uparrow\rangle &= \frac{1}{2} & S = 1 \qquad \tilde{S}^z|\Uparrow\rangle &= |\Uparrow\rangle \\ |\downarrow\rangle &= -\frac{1}{2} & |0\rangle &= 0 \\ & & |\Downarrow\rangle &= |\Downarrow\rangle \end{aligned} \tag{5.1.1.3}$$

The effective spin-1 chain model suggests that to first order there is a coefficient of ½ in the effective $z$-component of the Hamiltonian such that,

$$H^z_{eff} = \frac{J^z}{2}\tilde{S}^z_i\tilde{S}^z_{i+1} \tag{5.1.1.4}$$

Since this system is rotationally symmetric, meaning this derivation works for $S^z$ to produce a contribution $H^z_{eff}$ (eq. (5.1.1.4)) then the same process must work for $S^x$ and $S^y$. Without explicitly checking, we know this. So of course the excitation gap of this effective spin-1 chain will be $\approx J_\parallel/2$ rather than just

$J_{\|}$. The DMRG spin gap data should then show an excitation gap in the first adjacent sector ($M = [0, 1]$).

Examining figure 5.2 shows this theoretical prediction to be partially true. A gap appears but it is in the second adjacent sector ($M = [1, 2]$). That being said the effective system confirms the gap data in the ferromagnetic regime between magnetization sectors $M = 1$ and $M = 2$, showing a gap of roughly half the published value of $\Delta_H \approx 0.41052$ for a spin-1 chain. This effective contribution should also hold for a ladder with periodic boundaries but the gap would open between sectors $M = 0$ and $M = 1$ due to the unique ground state, a prediction discussed in a later section using the AKLT model.

### 5.1.2 Emergent edge states

As already discussed the excitation gap is opening in the second adjacent sector rather than the first. The reason for this is the boundary conditions. The excitation spectrum of the OBC system is being altered by the boundaries. In this case the gap is being prevented from opening in the first adjacent sector due to the emergence of edge states resulting from the open boundaries. It is important to understand the edge states and how they affect the gap. To do these we examine the magnetization of a spin-1 chain with and without edge states. Then we turn to the AKLT model, a model adiabatically connected to the spin-1 chain, to provide a nice method to understand these states.

Similar to the emergence of edge effects discussed in Chapter 4, these edge states will show up in magnetization calculations, so we again examine the local average magnetization. Figure 5.3 shows the local average magnetization for a spin-1 chain with open boundary conditions and it shows there is increased magnetization on the edges of the chain. This is clear evidence of the existence of edge states. And we state explicitely that these are actual states and not effects localized at the edges as seen with the spin-½ chain.

The emergence of these edge states can be stopped by simply placing a spin-½ site at each end of the chain, resulting in a clean gapped excitation, seen clearly in figure 5.3. It is precisely the fact that the emergent edge states can be mitigated by placing actual spin-½ particles at each end that tells us the these are edge states and not effects.

The oscillatory nature of the pure open chain is due to the effective spin-½ edge states, similar to the local average magnetization graphs in the previous chapter. The $+1/2$ magnetization on the edges of the spin-1 chain is not the result of a deliberately set positive polarizing field but appears to be a result of how the ALPS DMRG algorithm calculates local magnetization per site.

A good model to understand how these edge states are emerging is the AKLT model which uses

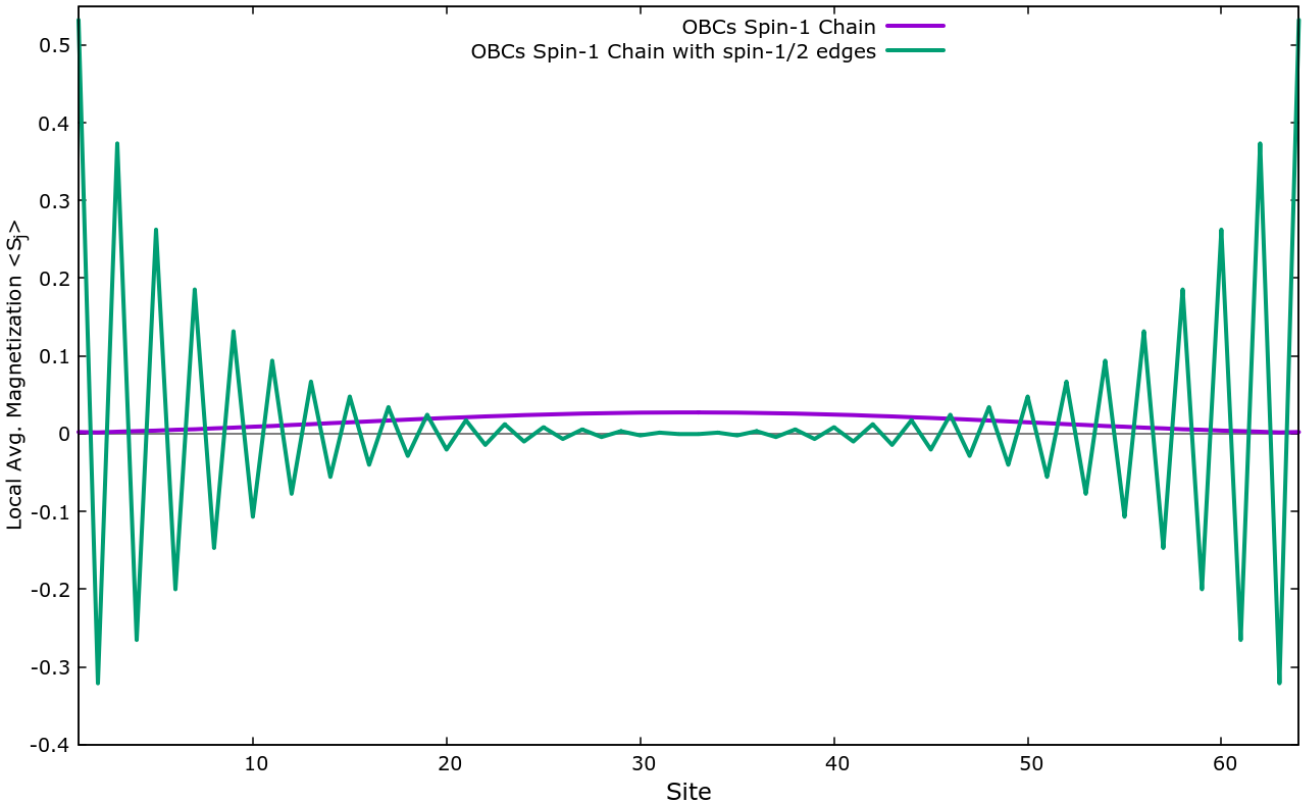


Figure 5.3: Graph of the local average magnetization $\langle S_j \rangle$ of a isotropic spin-1 chain with (blue) and without (green) spin-½ edge sites in OBCs using DMRG. $J = 1$.

coupled spin-½ sites to construct the wavefunction of a 1D spin-1 chain system. In the next section we will use this model to demonstrate the physics behind the emergence of the edge states and show how it affects our model.

### AKLT

In the ferromagnetic limit the system takes on the nature of a spin-1 wavefunction which allows it to be mapped to the AKLT model [35]. While the AKLT model is only adiabatically connected to our model, it provides a convenient construction to interpret the edge states. In a 1D model each "spin-1" site is made up of two spin-½ particles that are in a triplet state of either $|\uparrow\uparrow\rangle$, $|\downarrow\downarrow\rangle$ or $|\uparrow\downarrow\rangle + |\downarrow\uparrow\rangle$. Figure 5.4 demonstrates these model specifics diagrammatically. Each spin-1 is then coupled to the next site via a valence bond, creating a chain of "spin-1" sites. The valence bond connects adjacent spin-½ particles in a singlet state $|\uparrow\downarrow\rangle - |\downarrow\uparrow\rangle$.

As such, the 4-particles on two sites can only take a total spin of 1 or 0, which allows the higher energy spin-2 state to be projected out.

With periodic boundary conditions such a chain model has a unique groundstate, allowing for the

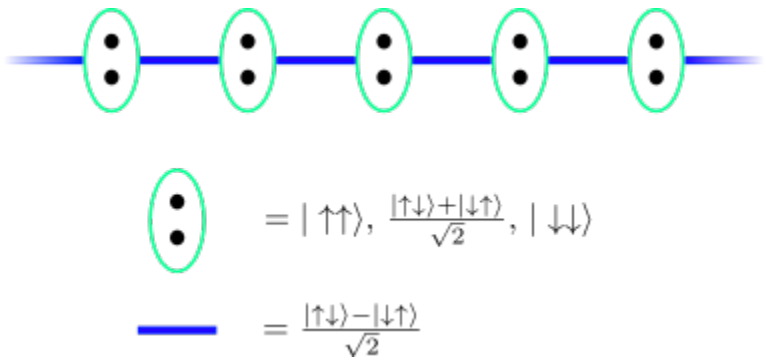


Figure 5.4: Diagram of AKLT model.

Haldane gap to open, Fig. 5.2. However an open chain creates a state with unpaired spin-½ particles on the first and last sites. The ends therefore act as free spin-½ moments even though the system is made up of effective spin-1s. The degeneracy of the ground state changes as a function of its length. For short chains, interactions result in a system with a triple degenerate or unique ground state. As the chain increases towards the thermodynamic limit these end states decouple exponentially as a function of chain length resulting in a 4-fold degenerate groundstate. In this case the length of the leg is sufficient to demonstrate this 4-fold degeneracy, giving the gapless result.

So far in this section an effective Hamiltonian was constructed to better understand the ferromagnetic regime who's consequences matched well with the DMRG results, i.e. the Haldane gap was half its known value. Additionally the existence of edge states was confirmed, an explanation for their emergence and the subsequent reason for the gapless ground state excitation was presented in the ALKT model. The discussion for the antiferromagnetic is more straight-forward and is presented in the next section.

## 5.2 Antiferromagnetic regime

In the strong antiferromagnetic rung regime ($J_\perp > 0$) the rungs form the singlet ground state of a 2-spin system, see table 5.1 and figure 5.5. In the strong limit of this regime the system becomes a series of rung-singlets, essential a bunch of 2-site chains. Interestingly the boundary conditions have no affect on the spin energy gap in this regime, as was shown in XXZ chain (see Chapter 4).

Since the ground state consists of a series of rung-singlets, to create an excitation in the system one of the rung-singlets needs to be promoted to a rung-triplet, figure 5.5. This promotion has the energy cost of $J_\perp$, hence the gap. It is easy to see this direct proportionality ($\Delta_s = J_\perp$) in figure 5.2. In this instance the origin of the gap is clear.

There is interesting evidence according to White [36] and Kim et al [37], to suggest that the antifer-

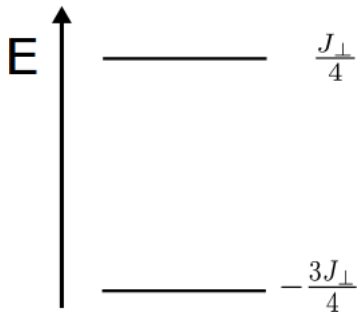


Figure 5.5: Energy levels of 2-spin system with singlet ground state.

romagnetic regime, which is not associated with any Haldane nature, does in fact exhibit features of a Haldane like phase. By adding diagonal *next-nearest-neighbor* couplings a continuous phase transition is shown between the spin-½ ladder and spin-1 chain. Features common to spin-1 systems including hidden topological order and string parameters are shown to arise in these conditions, presenting compelling evidence for distinct topological classes between the separate regimes. While it is important to note this relationship here, no additional research was done on this topic in this thesis and is therefore left for future work.

The results in this chapter have demonstrated that there are clear indications of phase transitions when examining the spin gaps of a system. However there are also 'pitfalls', meaning that having a degenerate ground state or emerging edge states can cause the spin gap to appear different than expected and that we may have to look in different sectors to find the right signal. This signal may be the gapless nature of a phase transition when the degeneracy changes or, similar to this case, the Haldane gap indicative of an integer-chain.

# Chapter 6

# Anisotropic Heisenberg Ladder

Here we examine the spin energy gap results for spin-½ anisotropic Heisenberg ladders. In the previous chapter the isotropic case was discussed, showing a gapped singlet phase as well as a Haldane like phase with emergent edge states. This chapter will build on these results by introducting anisotropies on both the legs and rungs. The first set of results examines an XXZ anisotropy introduced along the legs while keeping the rungs isotropic such that $J_{\parallel}^{xy} \neq J_{\parallel}^{z}, J_{\perp}^{xy} = J_{\perp}^{z} = J_{\perp}$. This discussion will set up the next section which introduces the XXZ anisotropy on the rungs and examines the strong rung coupling limits. The discussion continues on to building a phase diagram and examining 2D phase maps for our spin ladder model. The final section presents the weak rung coupling limits, introducing a field theory approximation for the phase transition lines, and then comparing these lines to the DMRG spin gap maps.

The XXZ anisotropic ladder Hamiltonian is,

$$\begin{aligned}\hat{H} = \sum_{j,n=1,2} J_{\parallel}^{xy}(S_{j,n}^{+}S_{j+1,n}^{-} + S_{j,n}^{-}S_{j+1,n}^{+}) + J_{\parallel}^{z}\sum_{j,n=1,2} S_{j,n}^{z}S_{j+1,n}^{z} \\ + \sum_{j} J_{\perp}^{xy}(S_{j,1}^{+}S_{j,2}^{-} + S_{j,1}^{-}S_{j,2}^{+}) + J_{\perp}^{z}\sum_{j} S_{j,1}^{z}S_{j,2}^{z}\end{aligned} \tag{6.0.0.1}$$

The fully isotropic case is seen clearly in Fig. 6.1 with a gapless ferromagnetic phase and gapped antiferromagnetic phase, as explained in the previous chapter. Introducing an XXZ anistropy along the legs such that $J_{\parallel}^{xy} = 1, J_{\parallel}^{z} \neq J_{\parallel}^{xy}$ creates two cases. The first, for $J_{\parallel}^{z} = [0.0, 0.5]$, the gap matches the isotropic case in both regimes, with slight variance in the weaker coupling ranges.

The second case, for $J_{\parallel}^{z} = 2.0$, is similar to the other cases in the antiferromagnetic regime but deviates in the ferromagnetic regime, going from a gapless to gapped phase. This indicates a change in the degeneracy, and subsequently the phase, moving away from the edge state degeneracy. At this coupling the system is in a striped-Néel phase [15] (ferromagnetically aligned rungs alternating direction).

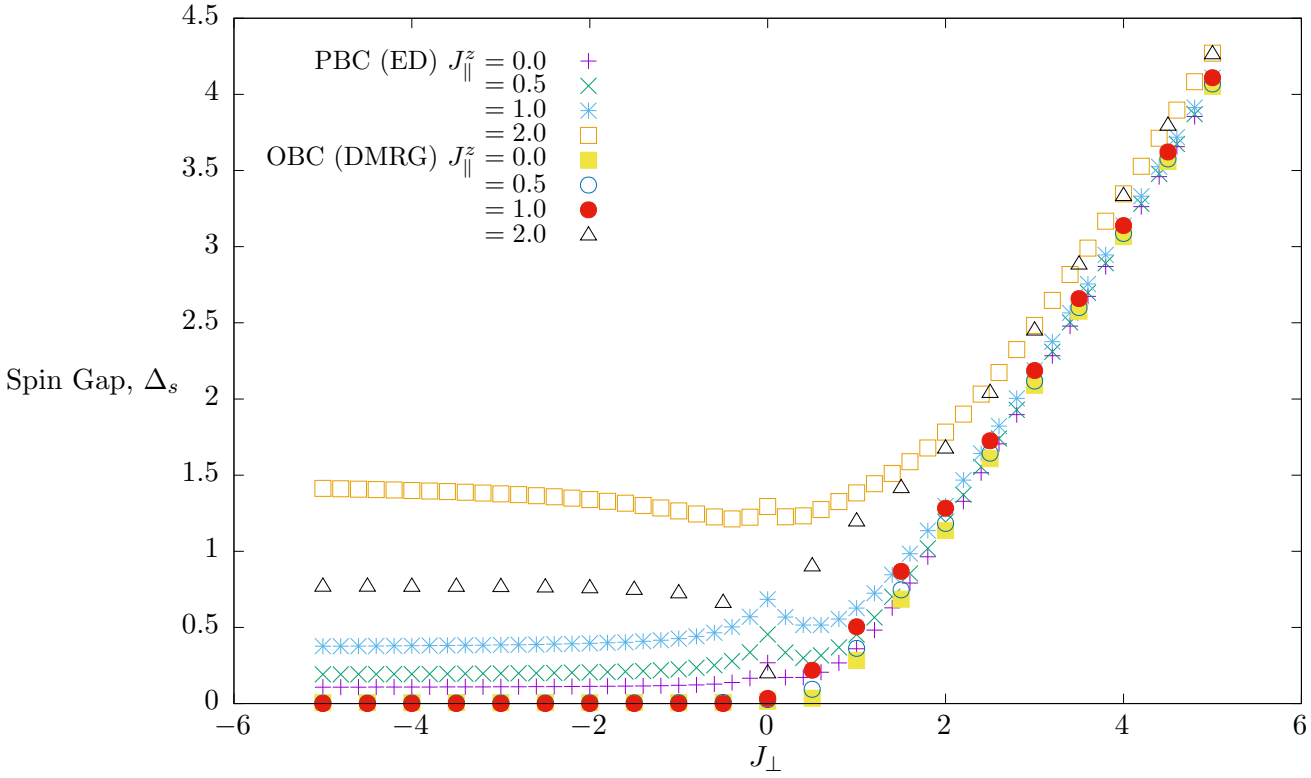


Figure 6.1: Graph of the spin gap $\Delta_s$ for spin-½ XXZ Heisenberg ladders as a function of the isotropic rung coupling $J_\perp$ for DMRG (OBCs) and exact diagonlization (PBCs). DMRG L=100, ED 12 PBC. $J_\parallel^{xy} = 1.0$, $J_\parallel^z = [0.0, 0.5, 1.0, 2.0]$.

Similar to the full Néel phase ($J_\perp >\sim 1$), the striped phase also exhibits a gap between the lowest sectors.

Exact diagonalization results, Fig. 6.1, present similar behaviour however there are obvious finite size effects due to the small system size ($L = 6$). Despite periodic boundary conditions for this calculation there would still be effective spin-1 operators similar to the OBC case presented in the previous chapter such that the gap would be diminished compared to the full Haldane gap. Additionally the ED data also displays the striped-Néel phase for $J_\parallel^z = 2.0$.

All of the curves in Fig. 6.1 merge in the strong antiferromagnetic limit, despite anisotropy and boundary conditions. This is due to the nature of a single excitation in the rung-singlet phase discussed previously.

## 6.1 Strong rung coupling limit

The coupling parameter space of this ladder model (Eq. (6.0.0.1)) is 4-dimensional. However, we fix the energy scale along the legs such that $J_\parallel^{xy} = 1$, reducing the space to 3-dimensions. A convenient method for examining the phase diagram is to fix the $J_\parallel^z$ value giving a discrete anisotropic ratio and then scanning the $J_\perp$ coupling space for $J_\perp^{xy}$ and $J_\perp^z$, taking a 'slice' from the phase space. This creates a

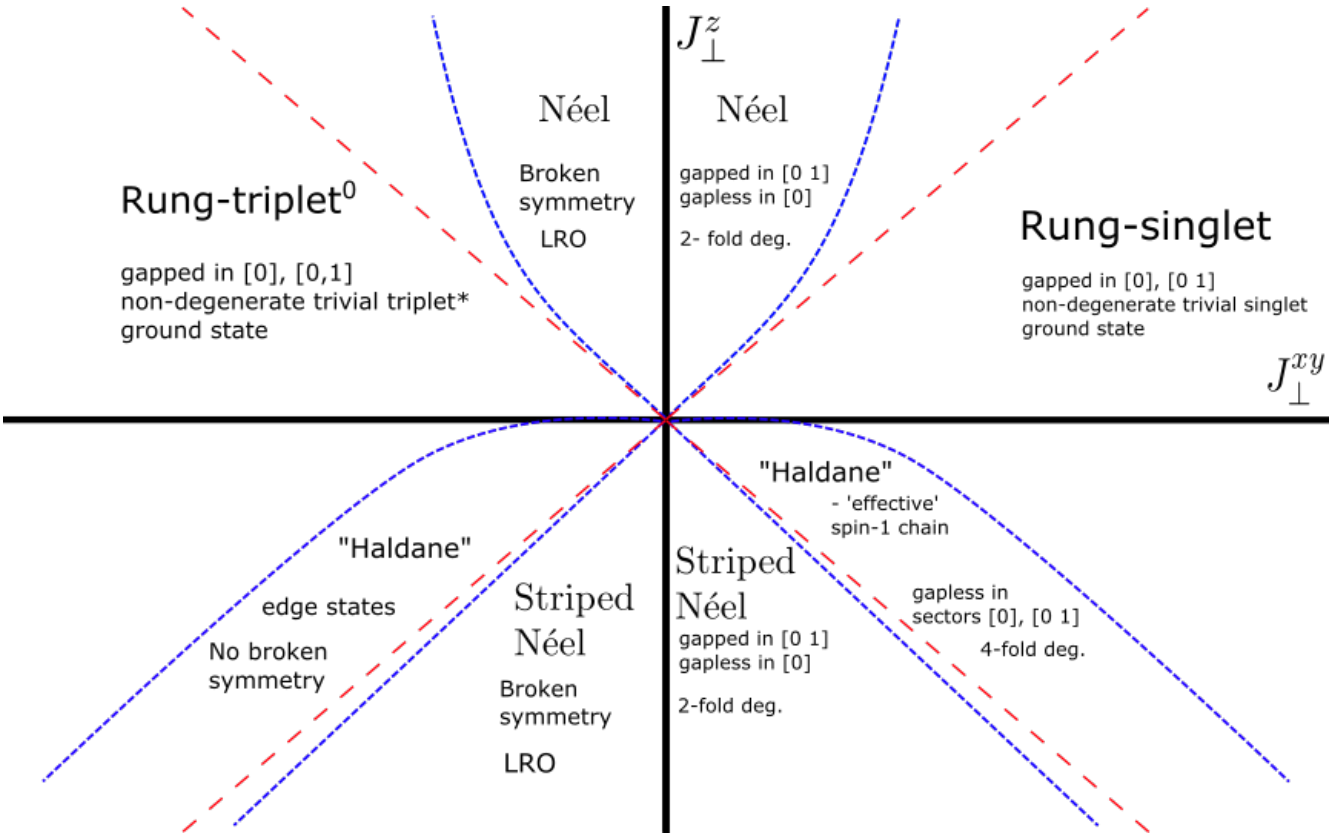


Figure 6.2: Schematic phase diagram for Heisenberg spin ladder spanning the strong rung coupling space ($J_\perp^{xy}$ and $J_\perp^z$) in the isotropic leg coupling case ($J_\parallel = 1$). Note that areas labeled Néel are the same phase across the vertical axis. The same goes for the striped-Néel and Haldane areas.

2-dimensional map of spin gap known as a density map. The following section will introduce and establish the descriptive phase diagram and discuss a series of strong rung coupling density maps for the $J_\parallel^z$ values of 0.0, 0.5, 1.0, 2.0.

### 6.1.1 Phase diagram

A schematic phase diagram was constructed by examining the states of a simple 2-spin rung system, and extracting locations of changes in degeneracy, indicative of a phase transition. The fruits of which are shown in figure 6.2. A phase boundary occurs where the energies of the lowest lying states meet and the degeneracy of the system changes. In the strong rung limit, $J_\perp^\alpha >> J_\parallel^\alpha$, the phases are well defined.

This diagram is formed in the isotropic leg coupling and strong rung coupling limits. Two phases are already known from the discussion on the isotropic case in Chapter 5, the rung-singlet and Haldane phases. There are three additional phases here, the pure antiferromagnetic (Néel) phase, the antiferromagnetic-leg/ferromagnetic-rung (striped-Néel phase) and another rung-singlet phase. This other rung-singlet phase is a non-degenerate ground state phase but unlike the true singlet phase which has the singlet ground state, this phase has the $S^z = 0$ component of the triplet state as the non-degenerate ground

state. The other components of the triplet are gapped. To avoid confusion this phase will be refered to as rung-triplet$^0$. This phase appears in the $J_\perp^{xy} < 0$ regime, mirror opposite the rung-singlet region. In the weak leg coupling there also exists the $xy\pm$ phase which occurs between the Haldane and striped-Néel phases. This phase will be examined more closely in the weak coupling subsection.

The results from the isotropic ladder discussion have shown preliminarily that due to degeneracies and emergent properties some transitions are found by looking at different sectors. In some cases calculations will also have to be made within a given sector to find the transition. So the phase diagram will have to be constructed by looking at a lot of different information. Building the phase diagram in this way will tell us the degeneracies of a phase and where to look for the gapless signal of a phase transition.

Each phase has a distinct ground state degeneracy, distinguishing it from the other phases. Thus as the system crosses a phase boundary the ground state(s) will change. A transition of phases presents with a change in the ground state degeneracy. In order for a non-topological phase transition to occur the gap must close before the system recovers a different ground state degeneracy representing a different quantum phase. This is quite a general statement, but as will be detailed later it explains the types of phases and the transitions between them. The gaps seen in the following results are taken within the ground sector ($M = 0$) and between the ground sector and the first excited sector ($M = 1$).

The phase diagram, figure 6.2, shows some transitions occur between sectors while others appear when the gap is calculated within a given sector. Thus, to gather a complete set of results we calculate energy data for several eigenvalues in each sector. We define $M = 0$ as the ground state sector in a non-excited system. By introducing a spin-1 excitation into the system, that is a total change in the $S^z$ quantum number, the $S^z_{total}$ quantum number changes by 1. The system is then in the $M = 1$ magnetization sector. Another spin-1 excitation gives the $M = 2$ sector and with each additional excitation the system enters a higher energy sector. A similar procedure is done to calculate additional eigenvalues within each sector except the $S^z_{total}$ quantum number is conserved, it remains fixed. The excitations are introduced such that their total change is 0

The phases are named for the ground states in the strong coupling limits. The Néel phase has a doubly degenerate antiferromagnetic ground state due to the AFM couplings along both the legs and rungs. This phase will be gapped between the ground and first sector but gapless within the ground sector. The rung-singlet consists of a fully gapped single unique ground state. A phase transition between the Néel and rung-singlet state will appear when the ground sector data is examined since the system is flowing from gapless to gapped. The same results are expected for the rung-triplet$^0$ state and the transition between to the Néel phase.

The Haldane phase has a fully gapless 4-fold degenerate ground state with spin-1 chain like properties. A transition line will be seen between the rung-singlet and the Haldane phase for all relevant calculations. The same is true with the rung-triplet$^0$ phase.

The striped-Néel phase has AFM interactions along the legs with FM interactions on the rungs resulting in a doubly degenerate ground state similar to the pure Néel phase. This phase will show a gapless nature both in the ground ($M = 0$) sector and the first adjacent sector ($M = [0, 1]$) calculation. A transition line will be seen with the Haldane phase in the first adjacent sector calculation. Throughout this thesis the phrase 'adjacent sector(s)' is used to mean the gap between magnetization sectors that are next to each other, i.e. $M = 0$ and $M = 1$ or $M = 1$ and $M = 2$. The boundaries between phases are not always clean and acute. We will see that the edges of the Haldane phase are smoother in the maps because the edge states are not as well defined in these areas.

### 6.1.2 Density maps

In this section a series of strong rung coupling spin gap density maps will be presented. Collectively these maps will show all of the phases. The adjacent sector maps, figure 6.3, show the rung-singlet, rung-triplet$^0$ and striped-Néel phases and their transitions. The ground sector maps, figure 6.4, show the Néel and Haldane phases along with the Néel-singlet, Néel-singlet* and singlet-Haldane boundaries. The maps will be presented in increasing leg anisotropy order, specifically in the order $J^z_{\parallel} = 0.0, 0.5, 1.0, 2.0$.

The maps represent 2D slices through our 3D phase space, spanning the parameter space of both $J^{xy}_{\perp}$ and $J^z_{\perp}$. The slices correspond to the discrete list of $J^z_{\parallel}$ values. A color gradient is applied to the values of the spin energy gap so that these maps become color coded representations of the phases of the ladder. The gradient is normalized to that given map or set of maps.

An interesting feature of the maps is the 'mirror' effect seen in the density maps, across the $J^z{}_{\perp}$ axis, and the theory diagrams. This feature is not unique to this particular model or couplings but is a known result arising from the invariance of the Hamiltonian to a specific class of rotations. This phenomena is described more fully in Appendix A.

Due to the large interval between couplings in the parameter space, the boundaries between phases are relatively smooth. Taking the logarithm of the gap calculation (right column in figures 6.3 and 6.4) sharpens these boundaries by saturating the high gap values and spreading the smaller gaps.

The transition line seen in the adjacent sector maps is the line separating the Haldane and rung-singlet phases. The Haldane phase is a 4-fold degenerate phase while the rung-singlet has a single ground state, thus making them gapless and gapped, respectively. There will be a phase line separating these

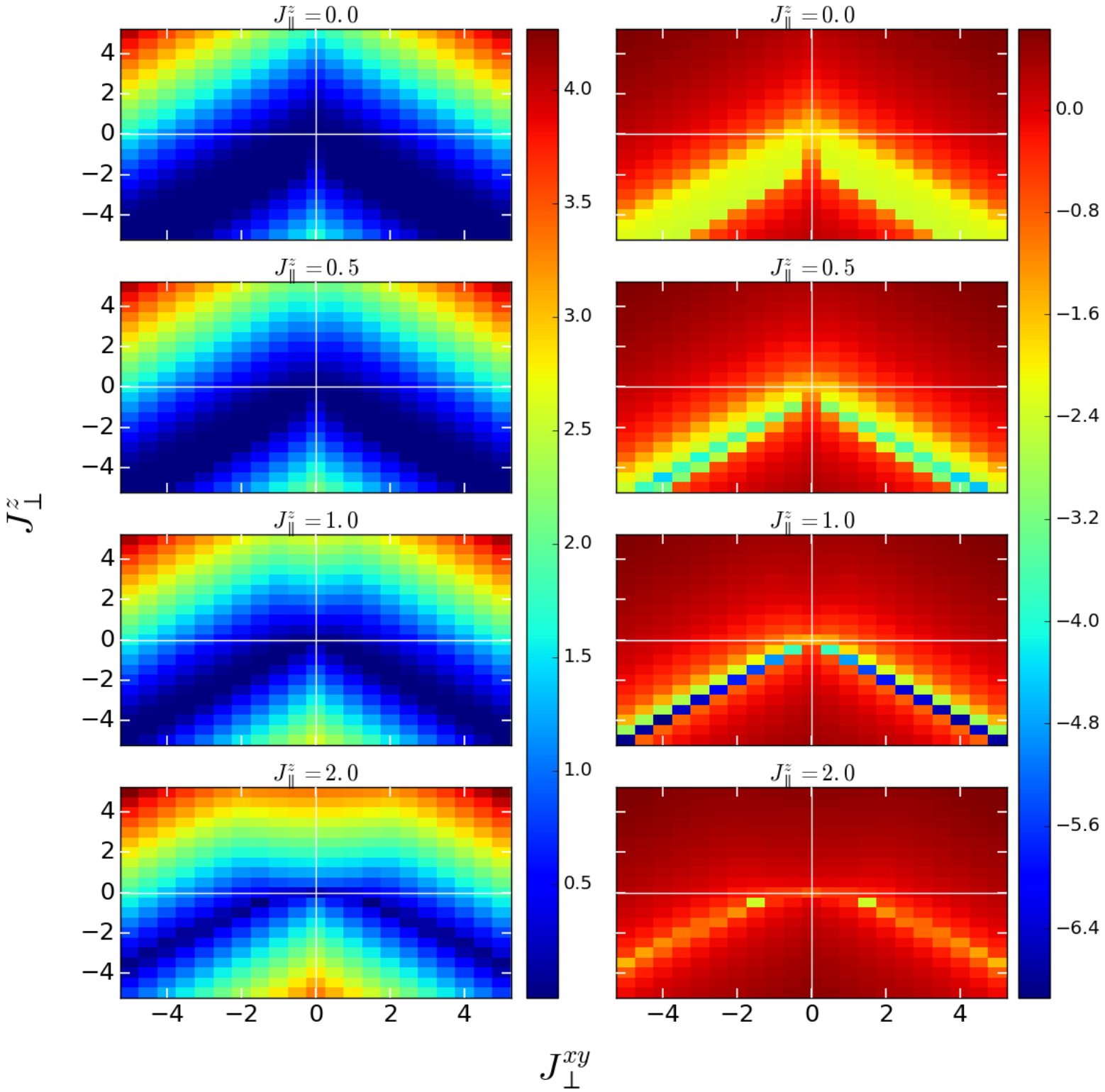


Figure 6.3: Density maps of spin gap as a function of rung couplings $J_{\perp}^{xy}$ and $J_{\perp}^{z}$ in the strong regime. DMRG $L = 100$, $J_{\parallel} = [0.0, 0.5, 1.0, 2.0]$, Sector gap $M = (0 - 1)$ Normalized linear gradient left, logarithmic gradient right.

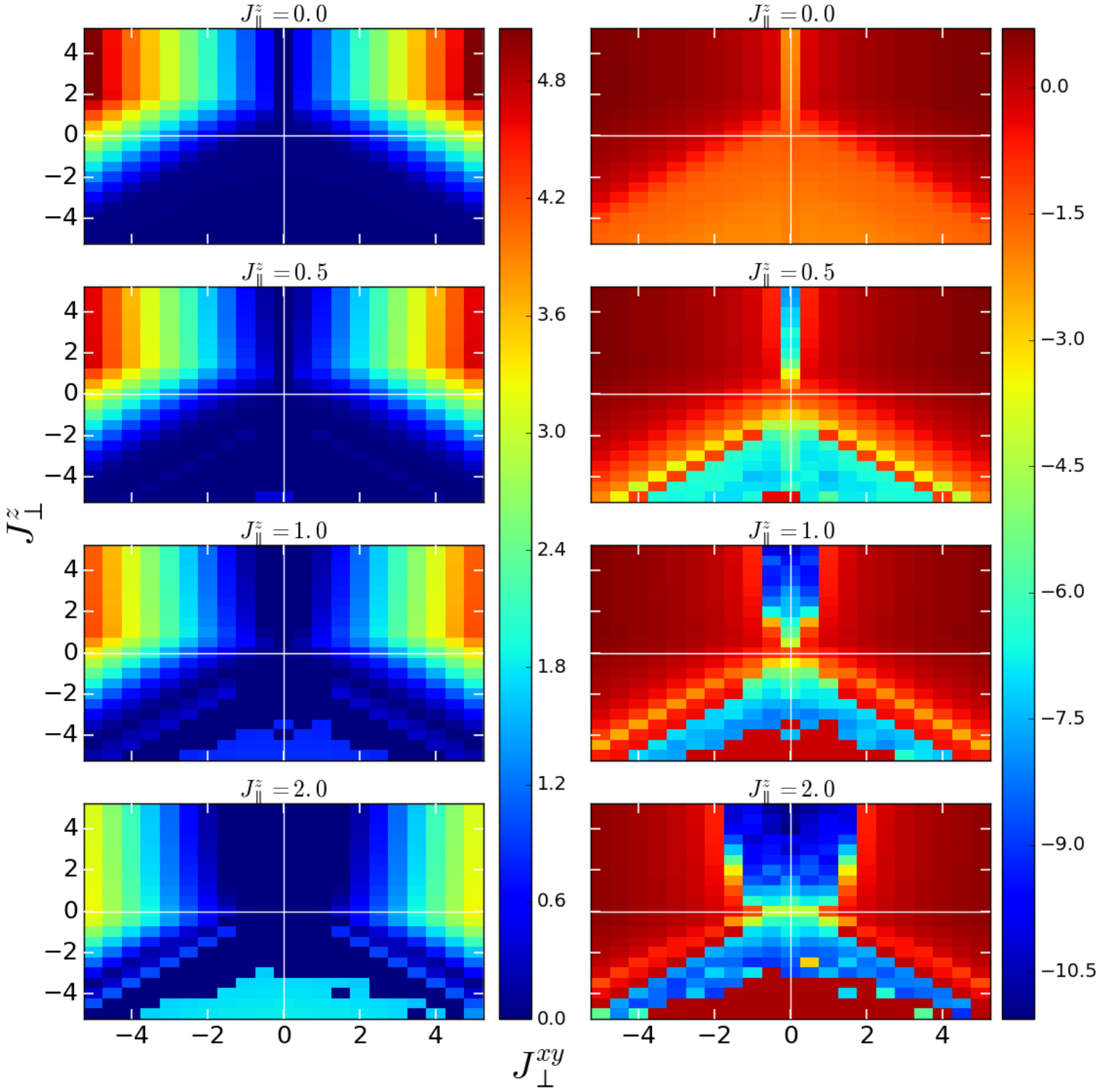


Figure 6.4: Density maps of spin gap as a function of rung couplings $J_{\perp}^{xy}$ and $J_{\perp}^{z}$ in the strong regime. DMRG $L = 100$, $J_{\parallel} = [0.0, 0.5, 1.0, 2.0]$, Sector gap $M = (0 - 1)$ Normalized linear gradient left, logarithmic gradient right. Ground sector ($M = [0]$), eigenvalue gap (1-2). Normalized linear gradient left, logarithmic gradient right.

since there is a change in the ground state degeneracy. The maps should also show a line separating the Haldane and striped-Néel phases since they are also gapless and gapped, respectively. Both the pure Néel and striped-Néel phases are doubly degenerate ground states, making them gapped for $M = 0, 1$ calculations.

As the leg coupling ($J^z_\parallel$) becomes increasingly antiferromagnetic the Haldane region thins. This change becomes most apparent when comparing the $J^z_\parallel = 2.0$ map to the $J^z_\parallel = [0.0, 0.5, 1.0]$ maps. The reduction of the Haldane region appears to come solely from the Haldane-(striped-Néel) transition line as it sweeps upwards. The Haldane-singlet line appears to maintain its position, suggesting the singlet is a much more stable phase.

The pure Néel phase region is shown to expand as $J^z_\parallel$ increases. This suggests a stronger $J^{xy}_\perp$ coupling is needed to lift the degeneracy and transition the system to a singlet phase. The line that appears in the positive $J^z_\perp$ regime in the ground state maps arises from the symmetric mode, so is not applicable to the theory lines derived in the previous section. This is as expected since the Haldane phase is degenerate in the ground state sector and the rung-singlet phase is fully gapped so there will be a transition between the two phases. Spin gap calculations within the ground state sector reveals expansion of the gapless Néel phase regions and subsequent movement of the phase line. However the striped-Néel area diminishes significantly as $J^z_\parallel$ increases. Similar to the adjacent sector case this line moves upward towards the $J^{xy}_\perp$ axis showing a diminishing Haldane region. In the last panel ($J^z_\parallel = 2.0$) this region nearly disappears. However this disappearance could be due to the resolution of the data. A more refined calculation would reveal the phase to still exist.

### 6.1.3 Strong coupling perturbations

Examining the maps in figure 6.4 along the $J^{xy}_\perp = 0.0$ origin line for $J^z_\perp > 0$ shows an increasing gap as $J^z_\perp$ increases, similar to the behaviour of an antiferromagnetic spin-½ chain. This gap behaviour can be seen more clearly in the logarithmic maps in figure 6.3. We can then ask the question, can this ladder model be mapped to a spin-½ chain and demonstrate the same behaviour seen in the map. To examine this we build an effective spin-½ model.

Using strong coupling expansion, the spin ladder is mapped to an effective spin-½ chain. In this expansion the strong coupling occurs on the rungs, which is taken as an unperturbed system. A perturbation is added to account for the interaction along the legs, which is weaker than the rung couplings. Together these form an effective Hamiltonian, approximating a spin-½ chain system.

Working in the AFM limit and with $J^{xy}_\perp = 0.0$, the ground states of a rung is the Néel alignment

| | Lower energy | | Higher energy | |
|---|---|---|---|---|
| $\|\uparrow\downarrow\rangle \equiv \left\|\tilde{\uparrow}\right\rangle$ | $E = -J_\perp^z$ | | $\|\uparrow\uparrow\rangle$ | $E = J_\perp^z$ |
| $\|\downarrow\uparrow\rangle \equiv \left\|\tilde{\downarrow}\right\rangle$ | | | $\|\downarrow\downarrow\rangle$ | |

Table 6.1: Table of 2-spin states, their energies and transformations for effective Hamiltonian derivation.

with a 2-fold degeneracy and energy $E_0 = -\frac{J_\perp^z}{4}$. The higher energy states are in FM alignment and are also doubly degenerate with energy $E_1 = \frac{J_\perp^z}{4}$. This is an examination of the low-energy physics so this procedure is in essence a Schrieffer-Wolff transformation [38, 39].

Treating the Hamiltonian as two separate components $H_\parallel^{xy}$ and $H_\parallel^z$ that are applied to the states in table 6.1 gives the effective contributions of these components. From here basic degenerate perturbation theory is employed to find the effective couplings that account for the leg interactions such that,

$$\begin{aligned} J_{eff}^{xy} &= \frac{(J_\parallel^{xy})^2}{2J_\perp^z} \\ J_{eff}^{z} &= \frac{(J_\parallel^{xy})^2}{2J_\perp^z} - J_\parallel^z \end{aligned} \tag{6.1.3.1}$$

The squared $J_\parallel^{xy}$ coupling term in equations (6.1.3.1) comes from the notion that a single application of the $xy$-Hamiltonian takes the state into the high energy manifold so a second operation is necessary to bring it back to the low energy regime. So $J_{eff}^{xy}$ always gives an antiferromagnetic contribution. The additional squared term in $J_{eff}^z$ comes about because the second order perturbation returns the same state, giving a diagonal contribution in the Hamiltonian matrix, just like a typical $S^z$ operator.

This gives the effective Hamiltonian,

$$\begin{aligned} H_{eff} &= H_0 + H_1 \\ H_0 &= J_\perp^z \sum_i S_{i,1}^z S_{i,2}^z \\ H_1 &= \frac{J_{eff}^{xy}}{2} \sum_i (S_i^+ S_{i+1}^- + S_i^- S_{i+1}^+) + J_{eff}^z \sum_i S_i^z S_{i+1}^z \end{aligned} \tag{6.1.3.2}$$

Therefore the energy gap from the low energy manifold to the high energy manifold are, respectively,

$$\Delta_s = \frac{J_\perp^z}{2} \tag{6.1.3.3}$$

The gap, equation (6.1.3.3), corresponds well to the data presented in the maps, figs. 6.3, 6.4. The gap increases for the adjacent sector (high energy manifold) as $J_\perp^z$ tends towards the strong limit. This

also coincides with the behavior of a spin-½ chain system, which was the intention.

It is important to note a few things that we have yet to explain. Most notably is the emergence of an unknown phase in the ferromagnetic $J_{\perp}^{z}$ regime in both the adjacent sector maps (Fig. 6.3) and ground state sector maps (Fig. 6.4). The phase is gapped in both calculations. It is suggested that this is a crossover into an effective spin-½ chain. Additional study is needed to lock down and understand this phase.

A brief note on the maps, there are a number of 'artifacts' present. These include errant pixels that have gap values extremely dissimilar to the immediate surrounding values. These artifacts are more apparent in the logarithmic maps. The explanation for these is a miscalculation in the DMRG.

## 6.2 Weak rung coupling limits

This section will present and discuss the weak rung coupling results for the 2-leg anisotropic Heisenberg spin ladder. Initially a brief introduction to a theoretical foundation put down by Mazo et al [12] for the anisotropic Heisenberg ladder will be given. Application of this theory to our model gives the phase transition lines and helps describe the individual phases in each region. Following this the theoretical results will then be compared to the experimental DMRG results. The DMRG results will be presented, analyzed and compared to the theoretical phase diagram for that given set of couplings.

### 6.2.1 Theoretical

Using quantum field theory Mazo et al [12] established a theoretical basis for the phase diagram of the anisotropic Heisenberg spin ladder. The field theory is adapted to calculate the symmetric and antisymmetric modes of the model leading to the placement of the transition lines in the weak coupling limits. Starting with the ladder Hamiltonian (6.0.0.1) we employ standard bosonization which expresses the spin operators as Bosonic fields[1]. This procedure decouples the Hamiltonian into symmetric and antisymmetric modes such that,

$$H_h = H_s^h + H_a^h \tag{6.2.1.1}$$

Here $h$ refers to the helicity of the ladder, this is based on the model developed by Mazo et al [12], $s$ and $a$ refer to the symmetric and antisymmetric modes, respectively. Following additional splitting of

[1]This derivation also uses non-canonical field rotations, see [12] for full explanation

the Hamiltonian into intra- and interchain parts and then a rotation of the fields gives,

$$\begin{aligned} H_{\epsilon}^{(h)} &= H_0^{\epsilon_h} + H_{int}^{\epsilon_h} \\ H_0^{\epsilon_h} &= \frac{\epsilon_v}{2\pi}\int dy[K_\epsilon(\delta_y\theta_{\epsilon_h})^2 + \frac{1}{K_\epsilon}(\delta_y\Phi_{\epsilon_h})^2] \\ H_{int}^{s_h} &= J_\perp^z \int \frac{dy}{2\pi a} cos(4\Phi_{s_h}) \\ H_{int}^{a_h} &= J_\perp^{xy}\int \frac{dy}{2\pi a} cos(2\theta_{a_h}) + J_\perp^z \int dy cos(2\Phi_{a_h}) \end{aligned} \tag{6.2.1.2}$$

where $\epsilon$ refers to our modes, *int* is the interacting part of the Hamiltonian, $\theta$ and $\Phi$ are the fields and $K_\epsilon$ are the Luttinger parameters. From here the antisymmetric mode is therefore described by,

$$\begin{aligned} H_a^{(h)} = &\frac{\epsilon_a}{2\pi}\int dy[K_a(\nabla\theta_{a_h})^2 + \frac{1}{K_a}(\nabla\Phi_{a_h})^2] \\ &+ J_\perp^{xy}\int \frac{\epsilon_a dy}{2\pi a^2} cos(2\theta_{a_h}) \\ &+ J_\perp^z \int \frac{\epsilon_a dy}{2\pi a^2} cos(2\Phi_{a_h}) \end{aligned} \tag{6.2.1.3}$$

We only examine the case when both fields in the antisymmetric mode are present because then we can calculate the phase boundary between the two possible states. In this case the boundaries between the antisymmetric mode phases is given when the terms are roughly equal,

$$\left|J_\perp^{xy}\right|^{\frac{1}{2-\frac{1}{K_a}}} \sim \left|J_\perp^z\right|^{\frac{1}{2-K_a}} \tag{6.2.1.4}$$

Rearranging gives,

$$J_\perp^z \sim \pm\left|J_\perp^{xy}\right|^{\frac{K_a(2-K_a)}{2K_a-1}} \tag{6.2.1.5}$$

With the respective Luttinger parameters,

$$\begin{aligned} K_a \approx 2K(1+\frac{KJ_\perp^z\alpha}{2\pi\upsilon}) \quad K = \frac{\pi}{2arccos(-\frac{J_n^z}{J_n^{xy}})} \\ \alpha = lattice spacing \qquad \upsilon = \frac{J_n^{xy}\alpha}{K} \end{aligned} \tag{6.2.1.6}$$

The antisymmetric mode lines are mapped using equation (6.2.1.5). For $K_a = 1$ the generated map for the phase boundaries is shown in figure 6.5. In this case $|J_\perp^z| \sim \left|J_\perp^{xy}\right|$ such that the phase boundaries follow isotropic lines. Figure 6.5 gives a schematic diagram of the transition lines calculated from Eq. (6.2.1.4) for this case.

A change in the leg anisotropy produces a change in the curvature of the transition lines. For

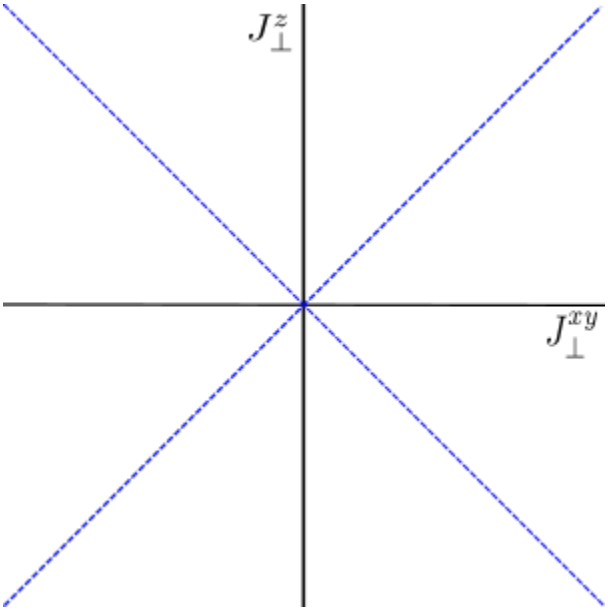


Figure 6.5: Schematic theoretical phase diagram with antisymmetric transition lines for $K \approx 1$ for 2-leg anisotropic Heisenberg spin ladder.

$1 < K_a < 2$ the transition lines move away from the isotropic lines, becoming curved, Fig. 6.6.

The symmetric mode lies along the $x$-axis because only one of the fields is described in the symmetric mode Hamiltonian, see [12] and [2], so there is no competition between the fields. This leads to $J_\perp^z \approx 0$, such that this line shouldn't show up in the weak coupling.

As we are working in the weak coupling limits we expand these equations for small $J_n^z/J_n^{xy}$, giving,

$$K_a \approx 2[1 + \frac{J_\perp^z - J_n^z}{2\pi J_n^{xy}}] \tag{6.2.1.7}$$

Similarly for the symmetric mode,

$$K_s \approx \frac{K}{2}(1 - \frac{K J_\perp^z \alpha}{2\pi \upsilon}) \approx \frac{1}{2}[1 - \frac{J_n^z + J_\perp^z}{2\pi J_n^{xy}}] \tag{6.2.1.8}$$

Using these expansions, we can better understand the phase diagram at weak couplings. These equations make up the foundation of determining the locations of the transition lines for our phase diagram. Additionally these factors tell us the separation between different orders and whether they will occur.

The symmetric mode has a dividing line at $K_s = 1/2$ such that the mode will have different characteristics on either side of this value. For $K_s > 1/2$ the mode is a gapless Luttinger liquid whose properties depend on $J_\perp^z$ and the strength of the intra-leg anisotropy ($J_n^z/J_n^{xy}$). This case is also accompanied by quasi-long range order (QLRO). When $|J_\perp^z| > \left|J_\perp^{xy}\right|$ the QLRO is seen in the $z\pm$ axes. Conversely, when

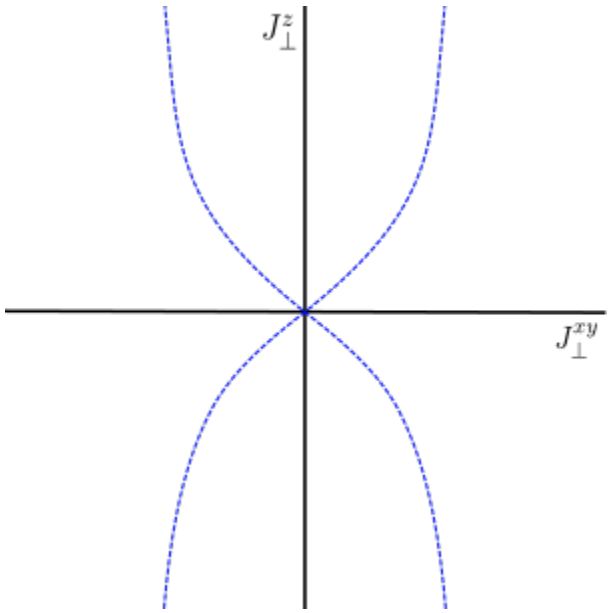


Figure 6.6: Schematic theoretical phase diagram with antisymmetric transition lines for $1 < K_a < 2$ for 2-leg anisotropic Heisenberg spin ladder.

$\left|J_\perp^{xy}\right| > |J_\perp^z|$ the QLRO occurs in the $xy\pm$ axes.

Equally, $K_s < 1/2$ indicates a mode in which the elementary excitations have acquired a spectral gap and has long range order or is in the Haldane phase. LRO occurs in the $z\pm$ direction when $|J_\perp^z| > \left|J_\perp^{xy}\right|$. The Haldane phase occurs when $\left|J_\perp^{xy}\right| > |J_\perp^z|$.

The value of $K_a$ will typically always fall between $1 < K_a < 2$. In the instance that $K_a > 2$ the pure AFM phase disappears completely. By rearranging equations (6.2.1.6) and (6.2.1.8) for $J_\perp^z$ we can find where these phase separations are.

### 6.2.2 Density maps - Isotropic Legs $J_\parallel^{xy} = J_\parallel^z$

The first model we examine is the XXX-leg model in which $J_\parallel^{xy} = J_\parallel^z = J_\parallel = 1.0$. This is a well studied and understood model [19, 20]. The anisotropic case is discussed in the next subsection.

Using $J_\parallel^{xy} = J_\parallel^z = 1.0$ gives,

$$K_a \approx 1 + \frac{J_\perp^z}{8\pi}$$
$$J_\perp^z \approx \pm\left|J_\perp^{xy}\right|^{\frac{1-(\frac{J_\perp^z}{8\pi})^2}{1+\frac{J_\perp^z}{4\pi}}} \tag{6.2.2.1}$$

This results in the antisymmetric mode transition lines in Fig. 6.7. We can understand this result

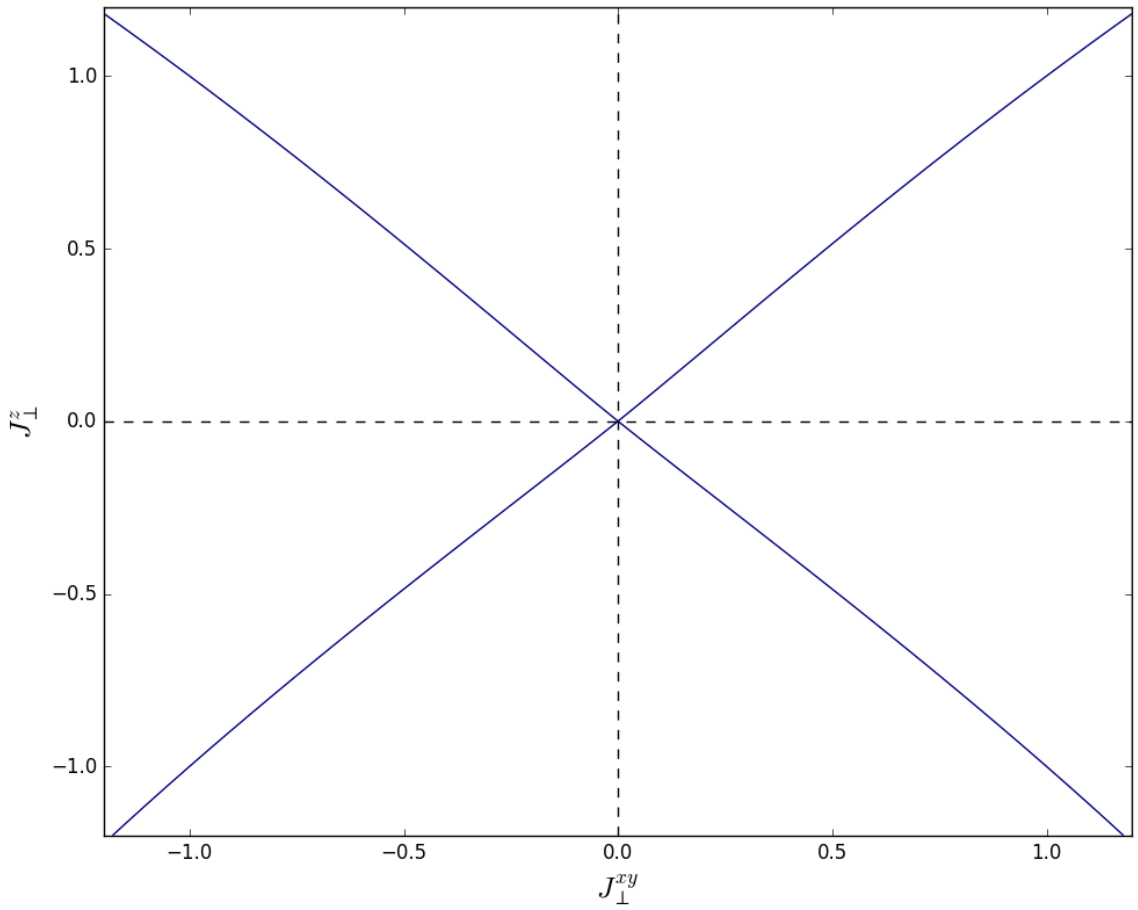


Figure 6.7: Theoretical Phase diagram for isotropic leg case, antisymmectric mode based on (6.2.2.1) with $J_\parallel^z = 1.0$ for 2-leg anisotropic Heisenberg spin ladder.

further by taking the second order term to be small and dropping it from the calculation.

$$\begin{aligned} J_\perp^z &\approx \pm\left|J_\perp^{xy}\right|^{1-\frac{J_\perp^z}{4\pi}} \\ &\approx \pm\left|J_\perp^{xy}\right|(1-\frac{J_\perp^{xy}}{4\pi} ln\left|J_\perp^{xy}\right|) \end{aligned} \tag{6.2.2.2}$$

The derivation continues by dropping terms larger than first order, expanding for small $J_\perp^z$ to first order and using the relations $e^{-x} \approx 1 - x$ and $|a|^x = e^{-xln|a|}$. The value of $K_a$ is very close to 1 for all values of $J_\perp^z$ which will produce a theory graph nearly identical to the $K_a = 1$ case in Fig. 6.5. Since $ln(|J_\perp^z|)$ will dominate the correction term, we can say ${}^{J_\perp^z}/_{4\pi} = {}^{J_\perp^{xy}}/_{4\pi}$ in the correction since this prefactor is small.

Referring back to the descriptive phase diagram, Fig. 6.2, the adjacent sector density map (Fig. 6.8a) clearly shows the emergence of the rung-singlet, Haldane and striped-Néel phases. The boundaries

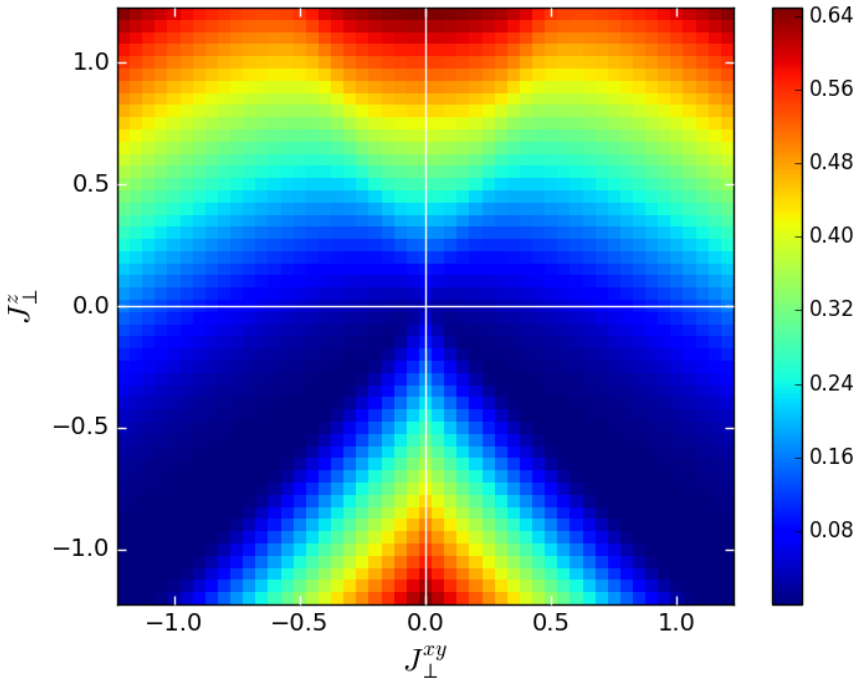


(a) Density map of spin gap as a function of rung couplings $J_\perp^{xy}$ and $J_\perp^z$ in the weak regime. DMRG $L = 100$, Isotropic leg case $J_\parallel = 1.0$, Sector gap $M = (0 - 1)$

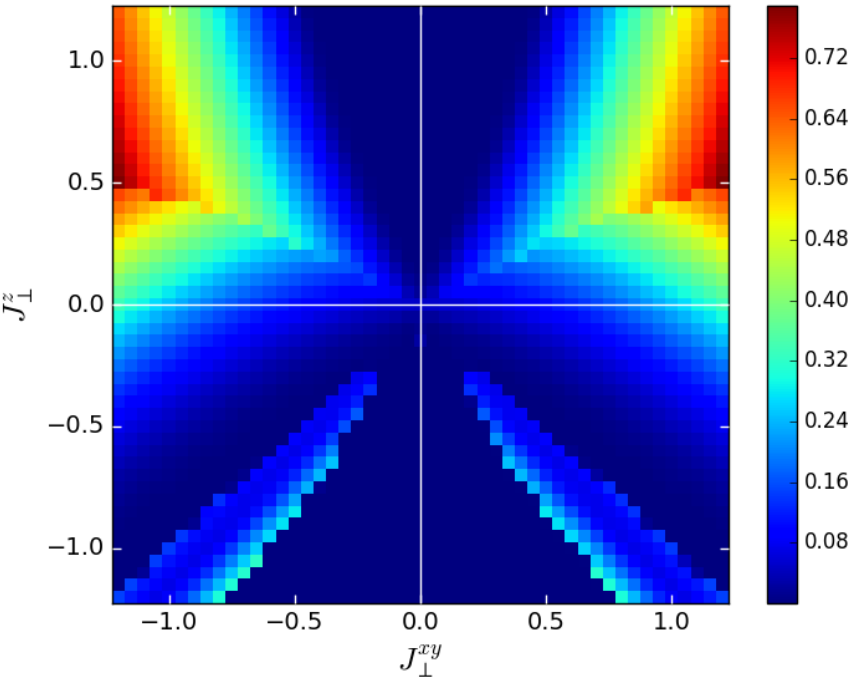


(b) Density map of spin gap as a function of rung couplings $J_\perp^{xy}$ and $J_\perp^z$ in the weak regime. DMRG L=100, Isotropic leg case $J_\parallel = 1.0$, Ground sector ($M = 0$), eigenvalue gap = (1-2)

Figure 6.8: Weak regime maps. Isotropic leg case $J_\parallel = 1.0$

between these phases appear continuous rather than spontaneous. The map shows a clear gapless Haldane region between a gapped rung-singlet region above and a gapless striped-Néel region below. As stated previously the $xy\pm$ phase does not appear in this regime. The ground state sector map, Fig. 6.8b, shows the emergence of the pure Néel phase as well as the Haldane, rung-singlet and striped-Néel phases.

The experimental DMRG results show phase lines that match the theory well for the ferromagnetic ($J_\perp^z < 0$) regime in Fig. 6.8a, showing a transition roughly along the isotropic line. The same figure also shows the emergence of the symmetric mode transition line which isn't predicted to arise until the strong coupling limits. Ground sector calculations, Fig. 6.8b, reveal the remaining transition lines in the positive $J_\perp^z$ regime.

Together the sets of data show a limited but working experimental picture of the emergence of the phase diagram in Fig. 6.2, displaying the pure Néel phase, rung-singlet, rung-triplet$^0$, Haldane and striped-Néel phase. However it can be noted that these regions follow the gapped/gapless descriptors set out in the phase diagram. The striped-Néel phase is shown to be gapped between the $M = 0$ and $M = 1$ sectors while being gapless in the ground state sector. The rung-singlet and rung-triplet$^0$ phases are gapped in both calculations while the pure Néel phase is gapped in adjacent sectors and gapless in the ground state sector, similar to the striped-Néel phase. The Haldane region shows up as well in both maps.

The antisymmetric and symmetric mode boundaries ($K_a = 2.0$ and $K_s = 1/2$ using equations (6.2.1.7), (6.2.1.8)) fall outside the weak coupling parameter space used here so we see the Néel phase along with quasi- and long range order phases. There should then be a strong match between the theory and the experimental data for this space.

### 6.2.3 Density maps - Anisotropic Legs $J_\parallel^{xy} \neq J_\parallel^z$

We now turn to the case when the leg couplings are anisotropic. An interesting result occurs when the isotropy is lifted along the legs such that $J_\parallel^{xy} \neq J_\parallel^z$ where we choose $J_\parallel^{xy} = 1$ and $J_\parallel^z = [0.0, 0.5, 1.0, 2.0]$, the maps change quite drastically. The isotropic case was studied in the previous section. In this section each anisotropy is introduced and discussed separately, starting with the field theory equations and then the experimental DMRG maps to compare to.

$J_\parallel^z = 0.0$

The first case we will look at is $J_\parallel^z = 0.0$ in which there is no interaction in the $z$-axis along the legs. This results in an XX-model in the legs, a model that should theoretically emerge as $J_\perp^z$ and $J_\perp^{xy}$ tend to

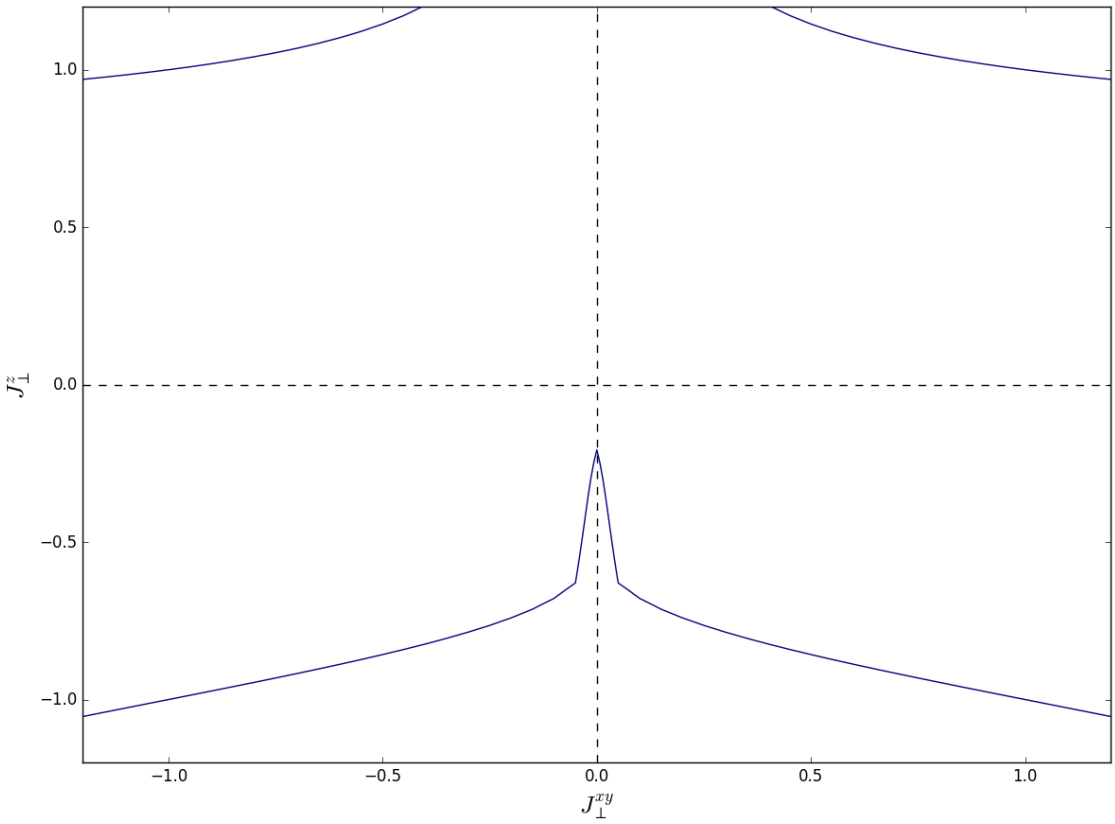


Figure 6.9: Theoretical Phase diagram for XXZ-leg case, antisymmectric mode based on (6.2.2.1) with $J_\parallel^z = 0.0$ for 2-leg anisotropic Heisenberg spin ladder.

0 Additionally the $xy\pm$ phases will emerge in this regime and be present in the maps.

The field theory gives the equations and transition curves for this case,

$$|J_\perp^z| \approx \left|J_\perp^{xy}\right|^{-\frac{2J_\perp^z}{3\pi+2J_\perp^z}} \tag{6.2.3.1}$$

The transition lines given by Eq. 6.2.3.1 only seem to be good up to a given coupling. For small $J_\perp^{xy}$ in the $J_\perp^z < 0$ regime the lines match well with the maps. However the transition lines diverge quickly and don't match either of the maps. Additionally the lines present in the $J_\perp^z > 0$ regime don't appear to exist at all in the maps. This suggests that the theory isn't well suited for small leg anisotropy.

Both the adjacent sector gap and single sector gap, Figs. 6.10a and 6.10b respectively, show vast low-gap/gapless regions in the negative $J_\perp^z$ regime which appears to be the $xy\pm$ phases. There are also the beginnings of the rung-singlet phase, along with the vague presence of the Haldane phase. However the distinction between the $xy\pm$ and Haldane phases is difficult because both phases are gapless so the gapless nature of a phase transition would be 'invisible' on these maps. A different method for examining

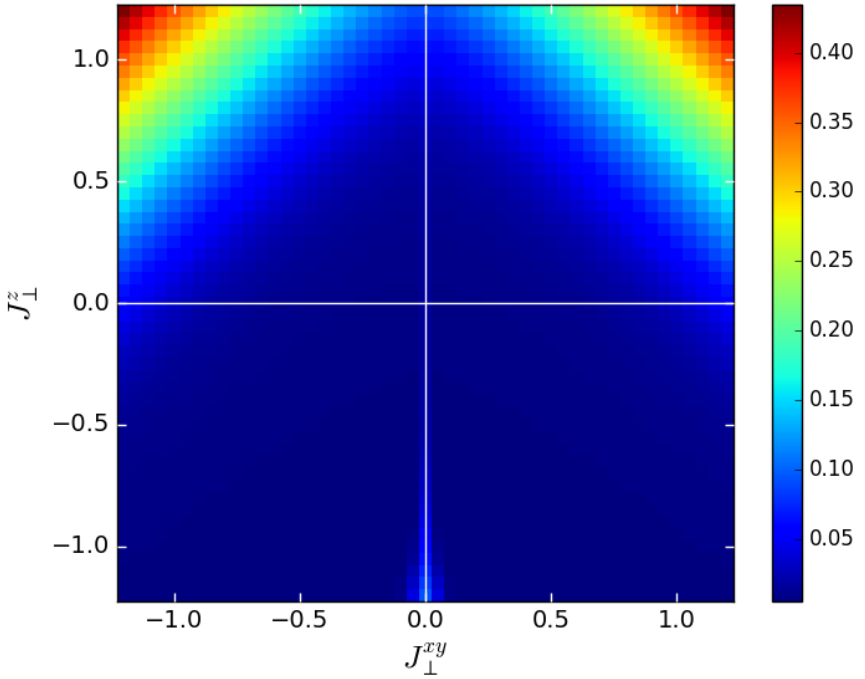


(a) Density map of spin gap as a function of rung couplings $J_\perp^{xy}$ and $J_\perp^z$ in the weak regime. DMRG $L = 100$, anisotropic leg case $J_\parallel^{xy} = 1.0$ $J_\parallel^z = 0.0$, Sector gap $M = (0 - 1)$

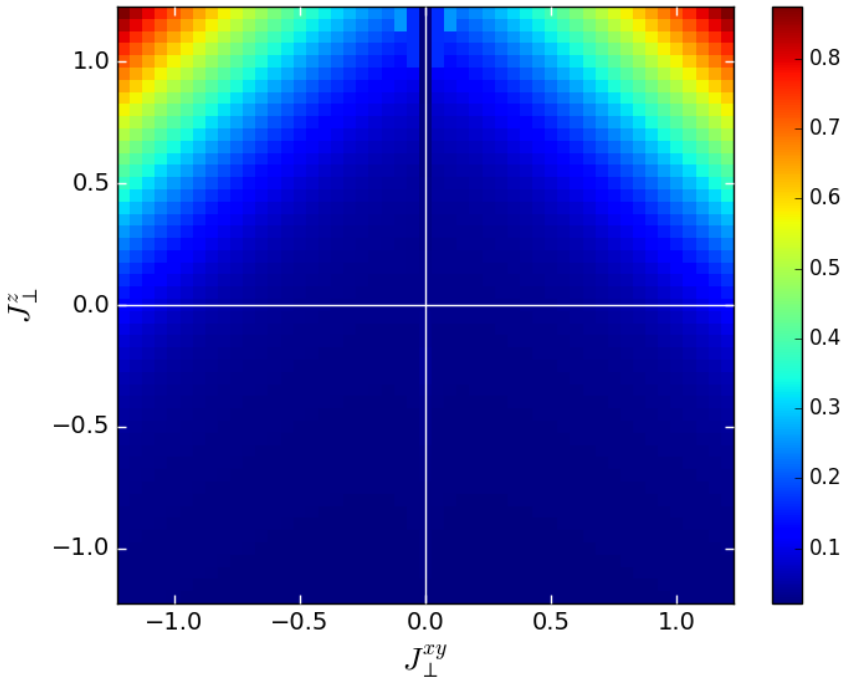


(b) Density map of spin gap as a function of rung couplings $J_\perp^{xy}$ and $J_\perp^z$ in the weak regime. DMRG $L = 100$, anisotropic leg case $J_\parallel^{xy} = 1.0$ $J_\parallel^z = 0.0$, Ground sector $M = 0$, eigenvalue gap = (1-2)

Figure 6.10: Weak regime maps. anisotropic leg case $J_\parallel^z = 0.0$

phase transitions would be able to distinguish between these phases. The effective spin-½ chain discussed in the previous section can be seen emerging along the $y$-axis for $J_{\perp}^{xy} = 0$ in both regimes, presenting with the immediate opening of an excitation gap.

For $J_{\perp}^{z} = 0.0$ the symmetric and antisymmetric mode limits ($K_a = 2$ and $K_s = 1/2$ per equations (6.2.1.7), (6.2.1.8)) are found to be along the $J_{\perp}^{z} = 0.0$ line. Further $K_a > 2$ for $J_{\perp}^{z} > 0$ such that the phase lines close on the $J_{\perp}^{z}$ axis and the Néel phase disappears. Equally $K_s > 1/2$ for $J_{\perp}^{z} > 0.0$ so the present rung-singlet phase has long range order. Since the symmetric mode phase limit and transition line share the same curve the Haldane phase is not present. The existing phases in this regime ($K_s < 1/2$ and $J_{\perp}^{z} < 0.0$), striped-Néel and $xy\pm$ have quasi-long range order. The $xy\pm$ phases are only present in these calculations for the weak coupling limits. As will be seen these phases exist between the Haldane and striped-Néel phases and is 'squeezed out' as the leg coupling strengthens. However since both the Haldane (as will be seen) and $xy\pm$ phases are both gapless there appears to be no distinction between them on the maps.

Interestingly the Néel phase doesn't exist here since there is no interaction for $J_{\parallel}^{z}$. However there appears to be a gapless line along the vertical axis for $J_{\parallel}^{xy} = 0$ in the $J_{\perp}^{z} > 0$ regime. This suggests there is a phase transition between the rung-singlet and rung-triplet$^0$ phases, identifying them as realizations of the same phase in different parameter regimes, despite having distinct ground state degeneracies.

$J_{\parallel}^{z} = 0.5$

Increasing the leg coupling so that $J_{\parallel}^{z} = 0.5$ shows a larger and more present striped-Néel region meaning the introduction of an excitation requires more energy compared to the same region in the $J_{\parallel}^{z} = 0.0$ map. Equally so the rung-singlet phase region has become larger, which together with the striped-Néel region, confines the Haldane region more.

The transition lines from the theory, Eq. 6.2.3.2 and Fig. 6.11, do no match well with the DMRG data, Figs. 6.12a and 6.12b.

$$\begin{aligned} |J_{\perp}^{z}| &\approx \left|J_{\perp}^{xy}\right|^{\frac{2+\frac{27J_{\perp}^{z}}{32\pi}}{0.75-\frac{27J_{\perp}^{z}}{64\pi}}} \\ |J_{\perp}^{z}| &\approx \left|J_{\perp}^{xy}\right|^{\sim 2.666} \end{aligned} \tag{6.2.3.2}$$

The pure Néel region is beginning to emerge in the ground state sector map, Fig. 6.12b. An interesting feature of this map is the gapped phase that opens around the origin which falls to gapless as $|J_{\perp}^{z}|$ becomes larger. This is not something expected since both the striped-Néel and pure Néel phases are gapless. An explanation for this is the confinement of spinons and the transition is between a topological and non-

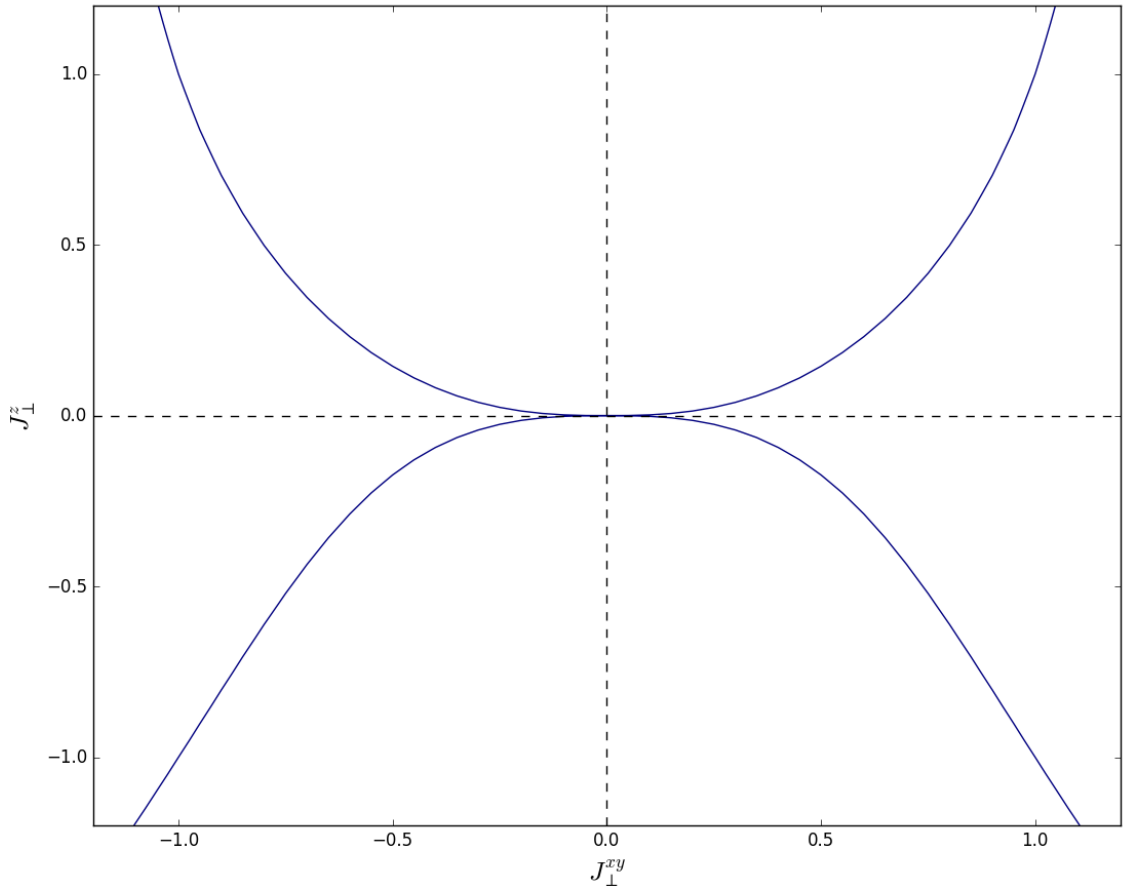


Figure 6.11: Theoretical Phase diagram for XXZ-leg case, antisymmectric mode based on (6.2.2.1) with $J_\parallel^z = 0.5$ for 2-leg anisotropic Heisenberg spin ladder.

topological phase.

Since the range of $K_a$ is $1 < K_a < 2$ the transition lines should be curved, as per figure 6.6, which is seen in figure 6.11. These antisymmetric transition lines don't match well with the corresponding phase boundaries on the maps. This suggests the theory isn't well suited to this calculation.

$J_\parallel^z = 2.0$

Continuing this trend we can ask the question, what happens to the spin gap when the legs are pushed into the fully gapped regime. To examine this we set $J_\parallel^z = 2.0$ and calculate the maps. There is no theory associated with this limit since the $K$ value breaks down for ${}^{J_\parallel^z}/_{J_\parallel^{xy}} > 1.0$.

The maps show significant gapped and gapless regions. The trace of the Haldane region is diminished and has been pushed towards the larger values of $J_\perp^{xy}$. Since the legs are fully gapped the Néel and striped-Néel phases cover large areas suggesting very stable phases. This is shown paricularly in figures

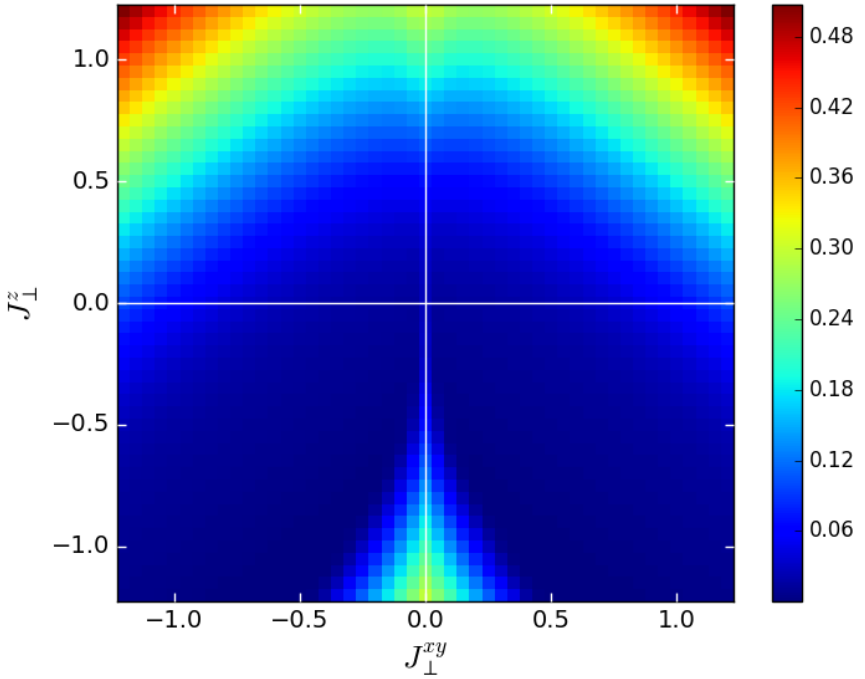


(a) Density map of spin gap as a function of rung couplings $J_\perp^{xy}$ and $J_\perp^z$ in the weak regime. DMRG $L = 100$, anisotropic leg case $J_\parallel^{xy} = 1.0$ $J_\parallel^z = 0.5$, Sector gap $M = (0 - 1)$

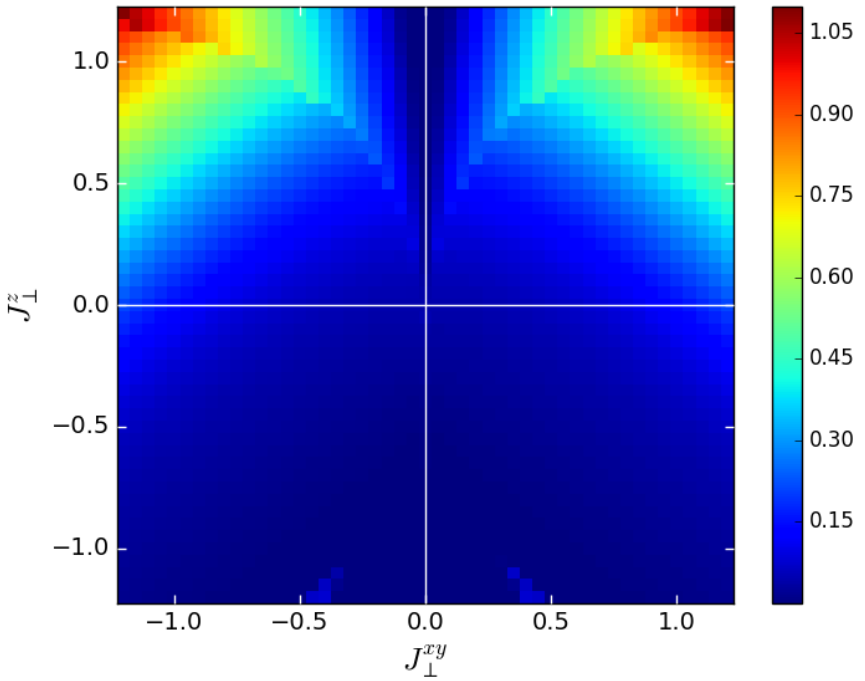


(b) Density map of spin gap as a function of rung couplings $J_\perp^{xy}$ and $J_\perp^z$ in the weak regime. DMRG $L = 100$, anisotropic leg case $J_\parallel^{xy} = 1.0$ $J_\parallel^z = 0.5$, Ground sector $M = 0$, eigenvalue gap = (1-2)

Figure 6.12: Weak regime maps. anisotropic leg case $J_\parallel^z = 0.5$.

6.13a and 6.13b. It requires stronger rung couplings to break this full gap and drop to a gapless system. The ground state sector map, Fig. 6.13b, shows large gapless regions, comparable to those in the adjacent sector maps.

$J_{\perp}^{z} = 2.0$ is an interesting case, but more generally for $J_{\perp}^{z} > 1.0$, in the weak rung coupling limit the legs (i.e. a spin chain) acquire a spin gap. This suggests that the transition lines wouldn't extend from the origin but would rather begin further out where the rung couplings are stronger. This can be seen more clearly in figure 6.14 where the logarithm of the gap has been taken. It shows that the phase boundaries don't extend from the origin but start much further out. Looking at Fig. 6.13b we see this as well.

In this section we have presented the results and analysis for the weak rung coupling limits showing that the field theory matches well for the isotropic leg case but doesn't match as well, to varying degrees, for weak leg anisotropies. The results have also shown the emerging phases that make up the strong coupling phase diagram. The Haldane phase appears to be a sensitive phase that is not well formed in all cases.

The strong coupling analysis in this chapter has shown the spin-½ anisotropic Heisenberg ladder has a very rich phase diagram with a variety of phases. These phases include, specifically, Néel, striped-Néel, rung-triplet$^0$, rung-singlet, and Haldane. These phases emerged and disappeared as the leg anisotropy changed. We have also shown this model is consistent with known results, in the limits of decoupled and effective spin-½ chains.

In the weak coupling limit, the isotropic case ($J_{\parallel}^{xy} = J_{\parallel}^{z} = 1.0$) showed the nearest match between the theoretical transition lines and the maps, see figures 6.7, 6.8a, 6.8b. This is the only case for which there is any match between experiment and theory. However the anisotropic cases ($J_{\parallel}^{xy} = 1.0$, $J_{\parallel}^{z} = [0.0, 0.5, 2.0]$) bear little resemblance to the theoretical lines. This tells us the field theory isn't well suited to anisotropic cases. Additionally it can't calculate cases where $J_{\parallel}^{z}/J_{\parallel}^{xy} > 1.0$. The theory appears limited to the isotropic case and needs more work to better calculate anisotropic cases.

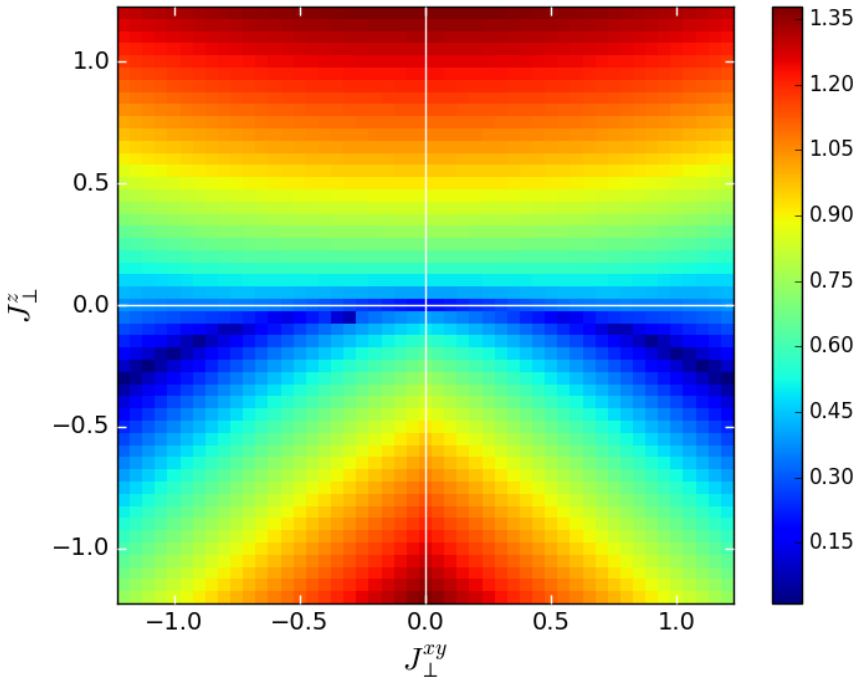


(a) Density map of spin gap as a function of rung couplings $J_\perp^{xy}$ and $J_\perp^z$ in the weak regime. DMRG $L = 100$, anisotropic leg case $J_\parallel^{xy} = 1.0$ $J_\parallel^z = 2.0$, Sector gap $M = (0 - 1)$.

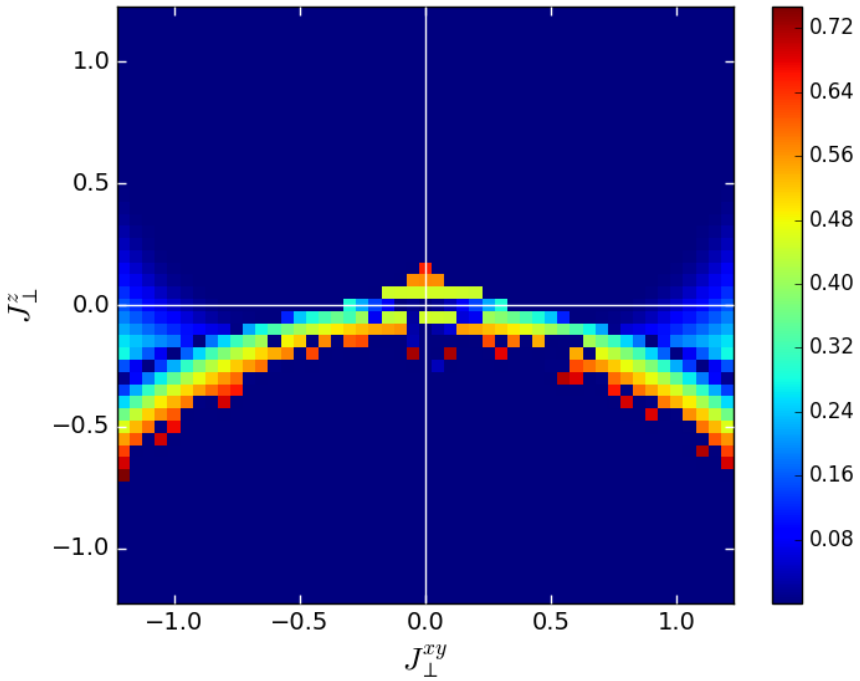


(b) Density map of spin gap as a function of rung couplings $J_\perp^{xy}$ and $J_\perp^z$ in the weak regime. DMRG $L = 100$, anisotropic leg case $J_\parallel^{xy} = 1.0$ $J_\parallel^z = 0.5$, Ground sector $M = 0$, eigenvalue gap = (1-2).

Figure 6.13: Weak regime maps. anisotropic leg case $J_\parallel^z = 2.0$.

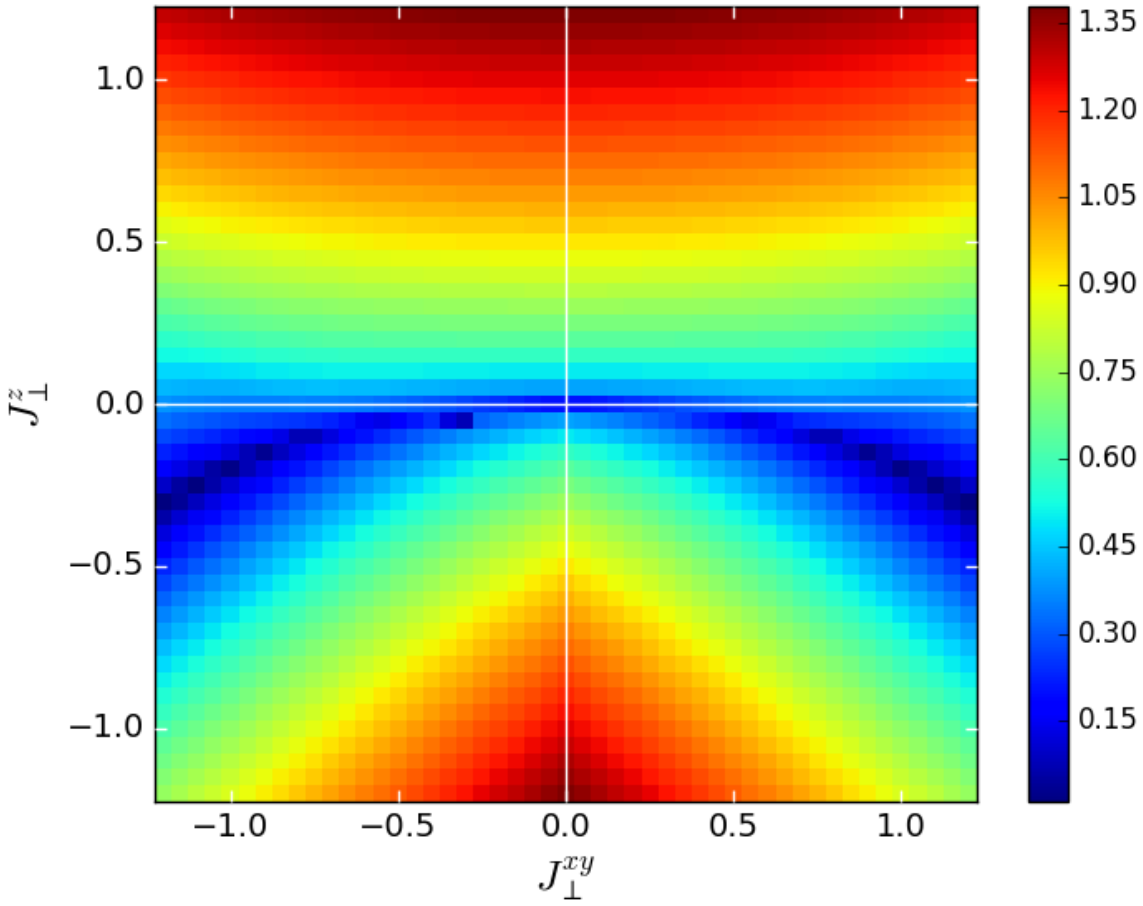


Figure 6.14: Density map of spin gap as a function of rung couplings $J_\perp^{xy}$ and $J_\perp^z$ in the weak regime. DMRG $L = 100$, anisotropic leg case $J_\parallel^{xy} = 1.0$ $J_\parallel^z = 2.0$, Sector gap $M = (0 - 1)$. Logarithmic scaling.

# Chapter 7

# Conclusions

The main aim of this thesis was to examine the phase diagram of the 2-leg spin-½ anisotropic Heisenberg spin ladder with open boundary conditions. This was accomplished by first studying the more basic spin-½ XXZ Heisenberg chain with open boundary conditions. This initial research confirmed known published results on fundamental excitations and also worked to affirm the techniques used in the next stage of the project, study of the 2-leg ladder geometry. The 2-leg spin-½ ladder was studied next, scanning a large rung coupling space to build 2-dimensional density maps of the spin gap. This showed the spin phases of the ladder and the transitions between them. We found the phase diagram of the Heisenberg ladder to be rich and complex.

In Chapter 4 we calculated the spin gap for the spin-½ XXZ anisotropic Heisenberg spin chain with open boundaries. The DMRG spin gap results showed a deviation between the system with open boundaries and the system with periodic boundaries. The difference, occuring in the antiferromagnetic rung-singlet phase, was a consequence of the emergence of edge effects due to the open boundaries. This research clarified a known result that the spin gap is set by the energy to create an excitation in a system. In this case a single domain wall (spinon) in open boundary conditions and two domain walls in periodic conditions, hence the difference in energy between the different system types. The gap in the open boundary system was therefore shown to be half the value of the gap in the periodic boundary system, in the strong coupling limit. In addition the magnetization of the system as a function of an applied magnetic field confirmed this first excitation deviation. Importantly this data also showed that for any macroscopic number of excitations (i.e. to magnetize the sample) the required amount of energy would be the same as for a open boundary system as it would for a periodic boundary system.

Chapter 5 introduced the 2-leg isotropic spin-½ Heisenberg spin ladder and calculated the spin gap of the system in a similar fashion to the XXZ chain in Chapter 4. In this case the leg couplings were held

fixed at 1 ($J_{\parallel} = 1$) and the rung coupling ($J_{\perp}$) was varied across positive (antiferromagnetic) and negative (ferromagnetic) values. The calculations showed, as a function of the rung coupling, the emergence of two gapped phases. The antiferromagnetic regime showed a rung-singlet phase with a direct proportionality between the rung coupling value and gap value.

The ferromagnetic regime was modeled as an effective spin-1 chain system due to the triplet ground state. The effective Hamiltonian, constructed by determining the effective couplings of the effective S=1 degrees of freedom, showed the Haldane phase would have a gap of roughly half the value given by the standard spin-1 chain formulation ($\Delta_s \approx 0.25026$). This result is therefore consistent with known results. Further analysis showed that the emergence of spin-½ edge states due to the open boundary conditions was creating a 4-fold degenerate ground state. This degeneracy led to the gapless phase. In this case the Haldane gap presented in the next highest sector gap, that is between the 1st and 2nd magnetization sectors. The existent of the emergent edge states was confirmed using magnetization results and the consequences of these states was explained using the adiabatically connected AKLT model.

Lastly in Chapter 6 the anisotropic Heisenberg ladder was investigated. Lifting the isotropy on the leg and rung axes vastly expanded the phase space, a description presented in the form of a phase diagram, figure 6.2. In the strong rung coupling limit the phase diagram was shown to be very rich with 5 phases which includes the pure Néel, rung-singlet, rung-triplet$^0$, Haldane and striped-Néel. The rung-singlet and rung-triplet$^0$ phases are the same fully gapped non-degenerate phases but with different ground states. These phases were shown to be quite robust, covering a large portion of the density maps and sharing transitions with the Haldane and pure Néel phases. However they diminish as the leg anisotropy becomes large.

The Néel phase was shown to be a 2-fold degenerate phase, presenting as gapped in the first adjacent sector calculations but gapless within the ground sector. This phase becomes more robust and pushes out into the rung- phases as the leg anisotropy increases ($J_{\parallel}^{z} > J_{\parallel}^{xy}$). The same characteristics are shared with the striped-Néel phase which has antiferromagnetic leg interactions and ferromagnetic rung interactions. The Haldane phase, as discussed in the isotropic section, presents with 4-fold degeneracy due to the emergence of edge states and is a fully gapless phase in the calculated sectors. This appears to be a fragile phase, with less defined states at its edges. It diminishes quickly as the legs enter the gapped antiferromagnetic phase. A weak coupling analysis, using field theory predictions of phase transition lines, showed some matches between the experimental DMRG results and the theoretical lines. This match was better near the isotropic leg limit, with some deviation from the theory for large anisotropy ($J_{\parallel}^{z} = 0.0, 0.5$). Interestingly in the large anisotropy maps there is the emergence of the $xy\pm$ phases,

which disappear for the smaller anisotropy because they fall outside the phase space. Unfortunately these phases fall next to the Haldane phase and share similar spin gap characteristics so could not be distinguished from it. However the theory becomes increasingly inaccurate as the anisotropy increases.

The main points from this project were that the boundary conditions of a 1D system are very important, the consequences of which need to be accounted for when calculating the results of excitations. The results presented here are consistent with known but seemingly unpublished findings.

The phase diagram of the 2-leg spin-$1/2$ anisotropic XXZ Heisenberg ladder in full parameter space was presented, a study no previous source has published, and was shown to be very rich. This richness was not only in phases but in the physics of the system itself. We found many of these phases to be degenerate or having edge effects, and in the case of the Haldane phase having edge states. These aspects of nature were shown to be very important, especially for low energy many-body systems. The theoretical basis put forth by Mazo et al [12] was partially accurate for the isotropic case but did not match experimental results for the anisotropic cases and does not extend to scenarios where the rung anisotropy is large, specifically $\left|J_{\parallel}^{z}/J_{\parallel}^{xy}\right| > 1$. More work is therefore needed on the field theory to better predict experimental results.

Lastly, while spin gap does provide good evidence of the phases and their boundaries it is not the best method to investigate, analyze and build a phase diagram for this model. These transitions and features were measured numerically with spin gap, everything found was compatible with what we would expect but it is very difficult to establish precisely these things due to potentially small gaps and different degeneracies. Other calculations, such as the fidelity of ground states, may be a much better method to hone in on the phase boundaries. Equally, there are limitations to the DMRG algorithm and there may be other numerical methods that provide better results.

**Outlook**

After establishing a working phase diagram for the XXZ ladder there are many new possible paths of research. An initial venture would be to confirm this work by calculating the full phase diagram using other methods and observables.

One of the original objectives of this research project was to look for a theorized phase emerging due to dimerization on the ladder. However it turned out that in fact the XXZ ladder was poorly characterized in the literature so this study needed to be carried out first, which ended up becoming this thesis. Therefore having constructed a full phase diagram of the XXZ ladder it would be interesting to then begin researching dimerizations, using this thesis as a basis to begin. While this is a specific example,

a general study of inequivalent legs (including dimerizations and frustrations) would be an interesting project.

Throughout this project it became quite apparent that many little details that, while may be common knowledge to researchers in this field, have gone unpublished. For example the affect of an open boundary on a spin-½ chain could not be found in the literature despite the fact that the spin chain is thoroughly studied model. So it would be a good bit of research to fill in some of these small gaps and tid bits of knowledge for publication.

# Appendices

# Appendix A

# Rotational Invariance in the Spin Hamiltonian

## A.1 Mirroring in density maps

An interesting feature of the spin gap density maps is the reflection (mirror) symmetry over the $J^z$ axis. The maps show that the spin gap is identical for $J^{xy} = |-J^{xy}|$, indicating that while the value of the $J^{xy}$ coupling is important to the calculation, the sign of the coupling makes no contribution to it.

In the following sections this result is explored further and rigorously by demonstrating the rotation of spins and the invariance of the Hamiltonian to the rotation of spins along the $xy$-axis.

## A.2 Rotation of spins

Physically speaking, changing the sign of the $J^{xy}$ coupling between positive and negative indicates a change in the favored interaction, that is from antiferromagnetic to ferromagnetic, respectively. When $J^{xy} > 0$, the $xy$-interaction favors antiferromagnetic alignment of the spins, for $J^{xy} < 0$ ferromagnetic arrangements. It is easy to think of this change as a rotation of the $xy$-component of the spin about the $z$-axis. We can use this idea of a rotation of the spin to get a more general understanding of this mirroring effect at the operator and state space level, and see why there is an invariance for this model.

Any given quantum system is described by its state vector, no matter how complicated. All of the state vectors that can describe a system make up the Hilbert space of that system. Any change performed on the system will also, in general, result in a change to the state vector, as well as the associated operators. This change should also be reflected in the observables since there has been a change in the operators. Such a change can be said to be a transformation of the system. Rotation is considered such

a transformation. Following the transformation, the original system state will have changed, giving a new state. Rotation transformations belong to the unitary class of transformations. This class preserves the vector relationships within the state space during the transformation, after mapping the space onto itself. Unitary transformations are described by a unitary operator, $U_R$, where the subscript $R$ stands for rotation. The rotated state $\left|\psi^{'}\right\rangle$[1] is given by,

$$\left|\psi^{'}\right\rangle = U_R \left|\psi\right\rangle \tag{A.2.0.1}$$

This transformation must preserve the vector relationships of the state space, which subsequently also means the transformation must preserve the properties of the observables associated with our system. An observable $Q$ taken with respect to the original state $|\psi\rangle$ will be the same as the observable $Q^{'}$ taken with respect for the transformed (i.e. rotated) system,

$$\langle\psi \,|\, Q \,|\, \psi\rangle = \left\langle \psi^{'} \,\middle|\, Q^{'} \,\middle|\, \psi^{'} \right\rangle = \left\langle \psi \,\middle|\, U_R^{\dagger} Q^{'} U_R \,\middle|\, \psi \right\rangle \tag{A.2.0.2}$$

Leading to the conclusion,

$$Q^{'} = U_R Q U_R^{\dagger} \tag{A.2.0.3}$$

An observable in the transformed system is obtained by applying the same unitary operator used to rotate the state space on the appropriate operator. From here the unitary operator $U_{\hat{u}}(\alpha)$ is defined more specifically as a rotation $R_{\hat{u}}(\alpha)$, about an axis $\hat{u}$ through an angle $\alpha$. To add more rigor to this derivation we examine an infinitesimal rotation $\delta\alpha$, on a quantum system. Such a rotation would change the state vector by an infinitesimal amount. The unitary operator now describes a transformation that is only infinitesimally different from the identity operator,

$$U_{\hat{u}}(\delta\alpha) = \mathbb{1} + \delta\alpha \hat{M}_{\hat{u}} \tag{A.2.0.4}$$

Since the angle of rotation is infinitesimal, the unitary operator will include a linear operator rather than a rotational one, since an infinitesimal rotation can be seen as a linear vector transformation. The linear operator $\hat{M}_{\hat{u}}$ now acts on the Hilbert space rather than the $R^3$ cartesian space. Additionally the linear operator depends on $\hat{u}$ (the axis vector) not the rotation $\delta\alpha$.

By computing the inverse, the linear operator $\hat{M}_{\hat{u}}$ is subsequenntly found to be anti-Hermitian, $\hat{M}_{\hat{u}} = -\hat{M}_{\hat{u}}^{\dagger}$. Operators that commute with the Hamiltonian are Hermitian. The $\hat{M}_{\hat{u}}$ is made Hermitian by

[1]The essentials of the following derivation, calculating the rotation operators, is credited to Parris [40]

defining $L_{\hat{u}} = i\hat{M}_{\hat{u}}$ which affects a infinitesimal rotation. The rotation operator becomes,

$$U_{\hat{u}}(\delta\alpha) = \mathbb{1} - i\delta\alpha L_{\hat{u}} \tag{A.2.0.5}$$

The operator $L_{\hat{u}}$ is referred to as the generator of an infinitesimal rotation about the axis $\hat{u}$. $L_{\hat{u}}$ can be expressed as a combination of operators representing the coordinate axes $(L_x, L_y, L_z)$, given that $\hat{u} = (u_x, u_y, u_z)$. This implies the fundamental relations,

$$\begin{aligned} U_{\hat{u}}(\delta\alpha) &= \mathbb{1} - i\delta\alpha(u_x L_x + u_y L_y + u_z L_z) \\ &= (\mathbb{1} - i\delta\alpha u_x L_x)(\mathbb{1} - i\delta\alpha u_y L_y)(\mathbb{1} - i\delta\alpha u_z L_z) \end{aligned} \tag{A.2.0.6}$$

Which gives,

$$U_{\hat{u}}(\delta\alpha) = U_x(u_x\delta\alpha)U_y(u_y\delta\alpha)U_z(u_z\delta\alpha) \tag{A.2.0.7}$$

Equation (A.2.0.7) implies the generator $L_{\hat{u}}$ can be represented as a vector operator, constructed from the Hermitian operator components $L_x, L_y, L_z$. These components are then themselves generators of infinitesimal rotations about their given coordinate axis. For an arbitrary infinitesimal rotation,

$$\begin{aligned} U_{\hat{u}}(\delta\alpha) &= -i\delta\alpha\vec{J}\cdot\hat{u} = \mathbb{1} - i\delta\alpha J_u \\ J_u &= \vec{J}\cdot\hat{u} \end{aligned} \tag{A.2.0.8}$$

Using the infinitesimal operator from Eq. (A.2.0.8) we can now construct the operators for a finite rotation.

$$U_{\hat{u}}(\alpha + \delta\alpha) = U_{\hat{u}}(\delta\alpha)U_\alpha(\alpha) = (\mathbb{1} - i\delta\alpha L_u)U_{\hat{u}}(\alpha) \tag{A.2.0.9}$$

The objective now is to find a formulation for the finite rotation operator $U_{\hat{u}}(\alpha)$. Taking the derivative with respect to the angle $\alpha$ to see how the operator changes as the angle changes,

$$\frac{dU_{\hat{u}}(\alpha)}{d\alpha} = \lim_{\delta\alpha\to\,0}\frac{U_{\hat{u}}(\alpha+\delta\alpha) - U_{\hat{u}}(\alpha)}{\delta\alpha} = -iJ_u U_{\hat{u}}(\alpha) \tag{A.2.0.10}$$

Then defining the boundary conditions such that $U_{\hat{u}}(0) = \mathbb{1}$, results in a solution satisfiying Eqs (A.2.0.9) and (A.2.0.10). The solution that satisfies these condictions is the unitary rotation operator,

$$U_{\hat{u}}(\alpha) = exp(-i\alpha L_u) = exp(-i\alpha\vec{L}\cdot\vec{u}) \tag{A.2.0.11}$$

For completeness,

$$U_{\hat{u}}(\alpha) = exp(-i\frac{\alpha}{\hbar}J_u) = exp(-i\frac{\alpha}{\hbar}\vec{J}\cdot\vec{u}) \tag{A.2.0.12}$$

We now consider the effects of this rotation operator on a spin system. A given spin-½ system is represented in its original state by $|\alpha\rangle$ and the rotated system by $|\alpha\rangle_R$ such that for a finite rotation of angle $\theta$ about the $z$-axis,

$$\begin{aligned} |\alpha\rangle_R &= U_z(\theta)\,|\alpha\rangle \\ U_z(\theta) &= exp(-i\frac{S_z}{\hbar}\theta) \end{aligned} \tag{A.2.0.13}$$

The next step is to calculate the expectation value of each spin operator to determine their value in the rotated state, where $\tilde{S}^x$ is the expectation value of that spin operator in the rotated system.

$$U(z,\theta)S^\alpha U^\dagger(z,\theta) = \tilde{S}^\alpha(\theta) \tag{A.2.0.14}$$

Equation (A.2.0.14) is solved by utilizing known properties of matrices and functions. In general a function can be defined through a power series. Using this idea and the property that any diagonalizable matrix can be raised to a power by simply applying the power to the diagonal elements (eigenvalues) of the matrix, we can state for a function $f$ and given matrix $\mathbf{A}$,

$$f(\mathbf{A}) = \mathbf{M}\begin{pmatrix} f(\lambda_1) & 0 \\ 0 & f(\lambda_2) \end{pmatrix}\mathbf{M}^\dagger \tag{A.2.0.15}$$

Therefore equation (A.2.0.13) becomes,

$$U_z = \begin{pmatrix} e^{-i\frac{\theta}{2}} & 0 \\ 0 & e^{i\frac{\theta}{2}} \end{pmatrix} \tag{A.2.0.16}$$

It is then easy to see how the rotation operator affects the expectation values of the spin components,

$$
\begin{aligned}
U(z,\theta)S_xU^{\dagger}(z,\theta) &= \begin{pmatrix} e^{-i\frac{\theta}{2}} & 0 \\ 0 & e^{i\frac{\theta}{2}} \end{pmatrix} \frac{\hbar}{2} \begin{pmatrix} 0 & 1 \\ 1 & 0 \end{pmatrix} \begin{pmatrix} e^{i\frac{\theta}{2}} & 0 \\ 0 & e^{-i\frac{\theta}{2}} \end{pmatrix} \\
&= \frac{\hbar}{2} \begin{pmatrix} 0 & e^{i\theta} \\ e^{-i\theta} & 0 \end{pmatrix} \\
&= \frac{\hbar}{2} \begin{pmatrix} 0 & cos(\theta) + isin(\theta) \\ cos(\theta) - isin(\theta) & 0 \end{pmatrix} \\
\tilde{S}^x &= S_x cos(\theta) - S_y sin(\theta)
\end{aligned}
\tag{A.2.0.17}
$$

Equally for the other spin operators,

$$
\begin{aligned}
\tilde{S}^y &= S_x sin(\theta) + S_y cos(\theta) \\
\tilde{S}^z &= S_z
\end{aligned}
\tag{A.2.0.18}
$$

The expectation values for $S_x$, in (A.2.0.17), and $S_y$, (A.2.0.18), have changed in the rotated system while the value for $S_z$, (A.2.0.18), is unchanged. This indicates a rotation about the $z$-axis. We move the calculation on to affect a rotation in a system of $n$ spins. The unitary operator for a system of $n$ spins is,

$$
\begin{aligned}
T &= \prod_n (z,\theta) \\
&= U_1(z,\theta)U_2(z,\theta)U_3(z,\theta)\dots U_n(z,\theta)
\end{aligned}
\tag{A.2.0.19}
$$

## A.3 Invariance of the Hamiltonian

The derivation up to this point has been quite general. Here we apply some specificity to satisfy our model. As stated previously the change of sign on a coupling indicates a change in the preferred interaction, ferro- or antiferromagnetic. Therefore a change of sign is the same as rotating every other spin by $\pi$, such that equation (A.2.0.19) becomes,

$$
\begin{aligned}
T &= \prod_{n:odd} U_n(z,\pi) \\
&= U_1(z,\pi)U_3(z,\pi)U_5(z,\pi)\dots U_{n-1}(z,\pi)
\end{aligned}
\tag{A.3.0.1}
$$

Applying the system rotation operator (A.3.0.1) to the spin-½ Heisenberg chain Hamiltonian to calculate the expectation value gives,

$$\begin{aligned} \hat{H} &= J\sum_{i=1}^{N}[\frac{1}{2}(S_i^+ S_{i+1}^1 + S_i^- S_{i+1}^+) + S_i^z S_{i+1}^z] \\ THT^\dagger &= J^{xy}\sum_i (TS_i^x T^\dagger TS_{i+1}^x T^\dagger + TS_i^y T^\dagger TS_{i+1}^y T^\dagger) + J^z \sum_i TS_i^z T^\dagger TS_{i+1}^z T^\dagger \end{aligned} \tag{A.3.0.2}$$

For a rotation of $\theta = \pi$,

$$\begin{aligned} T^\dagger T &= \mathbb{1} \\ TS_i^x T^\dagger &= (-1)^i S_i^x \\ TS_i^y T^\dagger &= (-1)^i S_i^x \\ TS_i^z T^\dagger &= S_i^z \end{aligned} \tag{A.3.0.3}$$

Substituting these into equation (A.3.0.2) gives,

$$\begin{aligned} THT^\dagger &= J^{xy}\sum_i ((-1)^i S_i^x (-1)^{i+1} S_{i+1}^x + (-1)^i S_i^y (-1)^{i+1} S_{i+1}^y) + J^z \sum_i S_i^z S_{i+1}^z \\ &= J^{xy}\sum_i ((-1)^{2i+1} S_i^x S_{i+1}^x + (-1)^{2i+1} S_i^y S_{i+1}^y) + J^z \sum_i S_i^z S_{i+1}^z \\ &= J^{xy}\sum_i (-1)^{2i+1}(S_i^x S_{i+1}^x + S_i^y S_{i+1}^y) + J^z \sum_i S_i^z S_{i+1}^z \\ &= (-1)J^{xy}\sum_i (S_i^x S_{i+1}^x + S_i^y S_{i+1}^y) + J^z \sum_i S_i^z S_{i+1}^z \\ &= -J^{xy}\sum_i (S_i^x S_{i+1}^x + S_i^y S_{i+1}^y) + J^z \sum_i S_i^z S_{i+1}^z \end{aligned} \tag{A.3.0.4}$$

where $(-1)^{2i+1} = -1$ since $2i+1$ is odd for all values of $i$.

Notice here that the sign of the $xy$-coupling has changed, $J^{xy} \to -J^{xy}$. The sign of $J^z$ is unchanged as expected. This transformation, (A.3.0.4) [41], has shown that the unrotated Hamiltonian is the same as the rotated one, the sign of $J^{xy}$ is unessential and merely sets the energy scale. $J^z$ is the important coupling in this calculation. Due to the outcome of the derivation the Hamiltonian is said to be invariant to this rotation transformation. This is an important observation as it represents a symmetry of the system. Symmetries are an essential concept in physics, here it tells us the variance of a system to a transformation.

### A.3.1 Commutation method

The above derivation can be shown equally using commutation relations or simple substitutions. An operator is invariant to a transformation if it obeys the commutation relation,

$$[T, H] = TH - HT = 0 \tag{A.3.1.1}$$

The conclusion is equally true if the generator of the rotation (A.2.0.9) is used in the relation in place of $T$. This is a trivial calculation to show,

$$TH = J^{xy} \sum_i (TS_i^x S_{i+1}^x + TS_i^y S_{i+1}^y) + J^z \sum_i TS_i^z S_{i+1}^z \tag{A.3.1.2}$$

where,

$$\begin{aligned} S^x S^x &= \frac{\hbar}{4} \begin{pmatrix} 0 & 1 \\ 1 & 0 \end{pmatrix} = \frac{\hbar}{4} = \frac{\hbar}{4}\mathbb{1} \\ S^y S^y &= \frac{\hbar}{4}\mathbb{1} \\ S^z S^z &= \frac{\hbar}{4}\mathbb{1} \end{aligned} \tag{A.3.1.3}$$

Which gives,

$$TH = J_{xy}\frac{\hbar}{2} \sum_i T + J_z \frac{\hbar}{4} \sum_i T \tag{A.3.1.4}$$

Similarly

$$HT = J^{xy} \sum_i (S_i^x S_{i+1}^x T + S_i^y S_{i+1}^y T) + J^z \sum_i S_i^z S_{i+1}^z T \tag{A.3.1.5}$$

where,

$$\begin{aligned} S_{i+1}^\alpha T &= S_{i+1}^\alpha \prod_{n:odd} U_n(z, \theta) \\ &= S_{i+1}^\alpha U_1(z,\theta) U_3(z,\theta) U_5(z,\theta) \dots \end{aligned} \tag{A.3.1.6}$$

The $S^\alpha$ operator will commute with $U$ where $n \neq i$ so it is unessential. Therefore,

$$\begin{aligned} HT &= \frac{J^{xy}}{2} \sum_i (S_i^x \frac{\hbar}{2} \begin{pmatrix} 0 & e^{-i\frac{\theta}{2}} \\ e^{i\frac{\theta}{2}} & 0 \end{pmatrix} + S^y \frac{\hbar}{2} \begin{pmatrix} 0 & ie^{-i\frac{\theta}{2}} \\ -ie^{i\frac{\theta}{2}} & 0 \end{pmatrix}) + J^z \sum_i S_i^z \frac{\hbar}{2} \begin{pmatrix} e^{i\frac{\theta}{2}} & 0 \\ 0 & -e^{-i\frac{\theta}{2}} \end{pmatrix} \\ &= J^{xy}\frac{\hbar}{2} \sum_i T + J^z \frac{\hbar}{4} \sum_i T \end{aligned} \tag{A.3.1.7}$$

Now substituting the results (A.3.1.4) and (A.3.1.7) into the commutation relation (A.3.1.1),

$$\begin{aligned}[T,H] &= TH - HT \\ &= [J^{xy}\frac{\hbar}{2}\sum T + J^z\frac{\hbar}{2}\sum T] - [J^{xy}\frac{\hbar}{2}\sum T + J^z\frac{\hbar}{2}\sum T] \\ &= 0\end{aligned} \tag{A.3.1.8}$$

Note simply, this commutation method produces the same result as (A.3.0.4). Alternatively a simple substitution shows the same result.

### A.3.2 Substitution method

Firstly the chain is 'divided' into two sublattices. The $A$-sublattice consists of all the even-labelled spins and the $B$-sublattice the odd-lablled spins. For a rotation around the $z$-axis on every second spin ($B$-sublattice) which is an effective rotation [42],

$$\begin{aligned} S_B^x &\to -S_B^x \\ S_B^y &\to -S_B^x \\ S_B^z &\to S_B^x \end{aligned} \tag{A.3.2.1}$$

$$\begin{aligned} S^+ &= S^x + iS^y & S^- &= S^x - iS^y \\ S^+ &= (-S^x) + i(-S^y) & S^- &= (-S^x) - i(-S^y) \\ &= -S^+ & &= -S^- \end{aligned} \tag{A.3.2.2}$$

Substituting these into the Hamiltonian gives,

$$\begin{aligned} H &= \frac{J^{xy}}{2}(S_A^+S_B^- + S_A^-S_B^+) + J^zS_A^zS_B^z \\ &= \frac{J^{xy}}{2}(S_A^+(-S_B^-) + S_A^-(-S_B^+)) + J^zS_A^z(S_B^z) \\ &= -\frac{J^{xy}}{2}(S_A^+S_B^- + S_A^-S_B^+) + J^zS_A^zS_B^z \end{aligned} \tag{A.3.2.3}$$

It is easy to see that the same result is recovered. For completeness we show that a rotation about the $x$-axis doesn't produce the same result but alters the structure of the Hamiltonian [42].

$$\begin{aligned} S_B^x &\to S_B^x \\ S_B^y &\to -S_B^y \\ S_B^z &\to -S_B^z \end{aligned} \tag{A.3.2.4}$$

$$\begin{aligned} S^+ &= S^x + iS^y & S^- &= S^x - iS^y \\ S^+ &= S^x + i(-S^y) & S^- &= S^x - i(-S^y) \\ &= S^- & &= S^+ \end{aligned} \tag{A.3.2.5}$$

Substituting these into the Hamiltonian gives,

$$\begin{aligned} H &= \frac{J^{xy}}{2}(S_A^+ S_B^- + S_A^- S_B^+) + J^z S_A^z S_B^z \\ &= \frac{J^{xy}}{2}(S_A^+(S_B^+) + S_A^-(S_B^-)) + J^z S_A^z(-S_B^z) \\ &= \frac{J^{xy}}{2}(S_A^+ S_B^+ + S_A^- S_B^-) - J^z S_A^z S_B^z \end{aligned} \tag{A.3.2.6}$$

As is clearly seen, a rotation about the $x$-axis changes the Hamiltonian (A.3.2.6) from its original form (A.3.0.2), demonstrating that it is not invariant to this specific transformation.

We have also demonstrated the concept of symmetry breaking here, which states that a system that obeys a given symmetry law may be forced to transition to an asymmetrical state. That is to say a system that is symmetric in the Hamiltonian, having degenerate energy ground states must choose between these unique ground states. The mirroring effect seen in the density maps show that the states are symmetric with regards to the Hamiltonian, given $J^{xy} = |-J^{xy}|$, but are distinctly different states.

# Appendix B

# ALPS

This chapter will be a reference on using the ALPS package, focusing on the DMRG application. ALPS (Algorithms and Libraries for Physics Simulations) is a free and open source software package that contains various numerical algorithms (e.g. DMRG, ED, Monte Carlo, etc) for running strongly correlated quantum mechanical simulations.

This chapter will, in order, describe the basics of the DMRG application, the parameter set which includes models and lattices as well as the system parameters, how to build the input parameter set and push this to the application. Finally the chapter will briefly go over the output data structure.

## B.1 Density Matrix Renormalization Group

Density Matrix Renormalization Group (DMRG) is an algorithm that allows large quantum systems to be simulated without the cost of a large Hilbert space. The DMRG application provided by ALPS is a high-end simulation code that is simple to set up and run.

Firstly all of the parameters are assembled which include the system parameters and the DMRG parameters. The system parameters establish the type of system that is going to be simulated including the lattice and the model specifications. The DMRG parameters tell the algorithm how many states to keep, the number of sweeps to perform, etc.

### B.1.1 Parameters and input file

The ALPS package provides a large variety of lattices and models to choose from, which are included in the *lattices.xml* and *models.xml* files respectively. The lattice definitions are designed such that unitcells and lattices can be combined to produce more complex geometries. If a given geometry isn't available it is simple to create your own by defining the unitcell and lattice graph. The physical models are described in

the *model.xml* file where the definitions for site bases, operators, parameters and Hamiltonians are coded. To maintain consistency we will use the open ladder geometry and spin Hamiltonian as the example throughout this chapter. These definitions are packaged in *xml* files using simple markup language.

The open ladder lattice defines a ladder geometry with open boundary conditions on both the width and length axes.

```
<LATTICEGRAPH name = "open ladder" vt_name="OpenLadderLattice">
  <FINITELATTICE>
    <LATTICE ref="square lattice"/>
    <PARAMETER name="W" default="2"/>
    <EXTENT dimension="1" size="L"/>
    <EXTENT dimension="2" size="W"/>
    <BOUNDARY dimension="1" type="open"/>
    <BOUNDARY dimension="2" type="open"/>
  </FINITELATTICE>
  <UNITCELL ref="anisotropic2d"/>
</LATTICEGRAPH>
```

Listing 1: Lattice graph for open ladder geometry

```
<UNITCELL name="anisotropic2d" dimension="2">
  <VERTEX/>
  <EDGE type="0"><SOURCE vertex="1" offset="0 0"/><TARGET vertex="1" offset="1
   ↪  0"/></EDGE>
  <EDGE type="1"><SOURCE vertex="1" offset="0 0"/><TARGET vertex="1" offset="0
   ↪  1"/></EDGE>
</UNITCELL>
```

Listing 2: unitcell definition for open ladder geometry

```
<LATTICE name="square lattice" dimension="2">
  <PARAMETER name="a" default="1"/>
  <BASIS><VECTOR>a 0</VECTOR><VECTOR>0 a</VECTOR></BASIS>
  <RECIPROCALBASIS><VECTOR>2*pi/a 0</VECTOR><VECTOR>0 2*pi/a</VECTOR></RECIPROCALBASIS>
</LATTICE>
```

Listing 3: Lattice definition for open ladder geometry

Listings 1, 2, 3 provide the definitions (coded in *xml*) for the open ladder. The unit cell and lattice definitions (listings 2, 3) are the foundational blocks that build the open ladder geometry; this statement is true in general for other geometries. The unit cell is the basic building block for crystal geometries, which describes the vertices (atoms) and their connections. In the open ladder case the unit cell is the *anisotropic2d*. The "square lattice" definition describes the crystal lattice basis vectors. These definitions

build the finite lattice definition, listing 1, which describes the meta-definition of the open ladder. The lattice graph describes the length and width characteristics of the system as well as the boundary type.

The Hamiltonian is constructed in a similar fashion, being made up of the site basis and basis definitions. As we are looking at a spin system, the following definitions are for the spin case. The typical structure for a model as coded in the ALPS libraries is:

```
<MODEL>
  <SITEBASIS Name=...> ... </SITEBASIS>
  <BASIS Name=...> ... </BASIS>
  <HAMILTONIAN Name=...> ... <HAMILTONIAN>
</MODEL>
```

Listing 4: Model definition structure in ALPS

The model structure is made of three elements, the site basis, basis and Hamiltonian. Most of the predefined models follow this structure. The site basis defines the single site Hilbert space and the basis defines this space for the entire lattice. The Hamiltonian command, quite obviously, defines the total energy quantum operator for the given model.

```
<SITEBASIS name="spin">
  <PARAMETER name="local_spin" default="local_S"/>
  <PARAMETER name="local_S" default="1/2"/>
  <QUANTUMNUMBER name="S" min="local_spin" max="local_spin"/>
  <QUANTUMNUMBER name="Sz" min="-S" max="S"/>
  <OPERATOR name="Splus" matrixelement="sqrt(S*(S+1)-Sz*(Sz+1))">
    <CHANGE quantumnumber="Sz" change="1"/>
  </OPERATOR>
  <OPERATOR name="Sminus" matrixelement="sqrt(S*(S+1)-Sz*(Sz-1))">
    <CHANGE quantumnumber="Sz" change="-1"/>
  </OPERATOR>
  <OPERATOR name="Sz" matrixelement="Sz"/>
</SITEBASIS>
```

Listing 5: Site basis definition for a spin-½ site.

The 'Spin' site basis, listing 5, describes the basis for a single spin site including the parameters, quantum numbers and single site operators associated with that site. Since we are dealing with spin-½ particles the spin quantum number ($\mathbf{S}$) is assigned the value 0.5 via the *local_S* parameter. Additionally the quantized axis is defined in the $S^z$ quantum number. The single site quantum operators $S^+$ and $S^-$ and their matrix elements are also defined here along with the change in the corresponding quantum number. These operators will be called on from the Hamiltonian definition.

The basis definition, listing 6, essentially applies the site basis definition for the entire lattice. It

```
<BASIS name="spin">
  <SITEBASIS ref="spin">
    <PARAMETER name="local_spin" value="local_S#"/>
    <PARAMETER name="local_S#" value="local_S"/>
    <PARAMETER name="local_S" value="1/2"/>
  </SITEBASIS>
  <CONSTRAINT quantumnumber="Sz" value="Sz_total"/>
</BASIS>
```

Listing 6: Lattice basis for spin models.

does this by referencing the necessary site basis definition, defining the spin-½ parameter and creating a system constraint. In this case the system constraint is on the sum total of the $S^z$ quantum number, $S^z_{total}$.

Lastly the Hamiltonian definition uses the site basis and basis definitions to build the Hamiltonian operator. The built-in spin Hamiltonian definition, listing 7, has codes for the most well studied parameter configurations. Since our model uses 4 parameters to calculate the leg and rung contributions (2 couplings on each dimension) we will utilize the parameters *Jxy0*, *Jz0*, *Jxy1* and *Jz1* where the trailing *0* denotes the couplings along the legs and the *1* the couplings on the rungs of the ladder.

We also note that ALPS provides the functionality and flexibility to create user generated lattices, graphs and models. If a given lattice or model isn't contained within the stock files, it is fairly simple to create your own as necessary. These functions were utilized to create a periodic chain in order to gather data for a periodic lattice and compare it to open boundary data, the conclusions of which are found in Chapter 4. The instructions to create custom lattices can be found on the ALPS website[1].

From here we construct the system specific parameters (local spin, system size, coupling values, etc) and the DMRG parameters (sweeps, observables, etc). In order to fully demonstrate this, listing 8 shows a small example of a DMRG parameter set for $S = 1/2$ Heisenberg ladder.

This parameter set defines the particle spin (*local_S*), the total $S^z$ quantum number (*Sz_total*), the number of sites on each leg ($L$), the isotropic leg and rung couplings (*J0* and *J1*) and a magnetic field ($h$). By default the DMRG algorithm calculates the energy of the system. In addition to this we can specify more observables for the algorithm to calculate including average magnetizations and correlations on every axis. There is also a setting to define the number of sweeps the finite size algorithm[2] performs.

Once the parameter set has been constructed it is pushed to the input file binary provided by ALPS,

[1] http://alps.comp-phys.org/mediawiki/index.php/Tutorials:LatticeHOWTO
[2] See Chapter 3

```
<HAMILTONIAN name="spin">
  <PARAMETER name="J0" default="0"/>
  <PARAMETER name="J" default="J0"/>
  <PARAMETER name="Jz" default="J"/>
  <PARAMETER name="Jxy" default="J"/>
  <PARAMETER name="Jz0" default="Jz"/>
  <PARAMETER name="Jxy0" default="Jxy"/>
  <PARAMETER name="J1" default="0"/>
  <PARAMETER name="J'" default="J1"/>
  <PARAMETER name="Jz'" default="J'"/>
  <PARAMETER name="Jxy'" default="J'"/>
  <PARAMETER name="Jz1" default="Jz'"/>
  <PARAMETER name="Jxy1" default="Jxy'"/>
  <PARAMETER name="h" default="0"/>
  <PARAMETER name="Gamma" default="0"/>
  <PARAMETER name="D" default="0"/>
  <PARAMETER name="K" default="0"/>
  <BASIS ref="spin"/>
  <SITETERM site="i">
    <PARAMETER name="h#" default="h"/>
    <PARAMETER name="Gamma#" default="Gamma"/>
    <PARAMETER name="D#" default="D"/>
      -h#*Sz(i)-Gamma#*Sx(i)+D#*Sz(i)*Sz(i)
  </SITETERM>
  <BONDTERM source="i" target="j">
    <PARAMETER name="J#" default="0"/>
    <PARAMETER name="Jz#" default="J#"/>
    <PARAMETER name="Jxy#" default="J#"/>
    <PARAMETER name="K#" default="0"/>
      Jz#*Sz(i)*Sz(j)+Jxy#*exchange_xy(i,j)+K#*biquadratic(i,j)
  </BONDTERM>
</HAMILTONIAN>
```

Listing 7: Spin Hamiltonian definition

listing 9 which builds the input file for the DMRG program. This program converts the plain text parameter file to *xml* format.

Listing 8 builds a parameter set for a single run of the algorithm with those parameters. To run the DMRG over a series of sets, say to scan a coupling space, we need to build a series of input files. This can be done in the style of listing 8 or using a python script. Listing 10 shows how this can be done using a parameter file, where the DMRG is run over a series of magnetic field values.

However this method can be cumbersome if several parameter spaces need to be scanned. Another method is to use a python script to generate all of the parameter sets and call the commands to generate the *xml* files. Depending on the computing facility and number of input files, it is often easier to create a separate script to push these files to the DMRG program, either in series or parallel.

```
{
   MODEL="spin"
   LATTICE="open ladder"
   local_S=1/2
   Sz_total=0
   L=10
   J0=1
   J1=1
   h=0
   SWEEPS=4
   MEASURE_AVERAGE[Magnetization]=Sz
   MEASURE_AVERAGE[Exchange]=exchange
   MEASURE_LOCAL[Local magnetization]=Sz
   MEASURE_CORRELATIONS[Diagonal spin correlations]=Sz
   MEASURE_CORRELATIONS[Offdiagonal spin correlations]="Splus:Sminus"
}
```

Listing 8: Example DMRG parameter set

```
parameter2xml parm_file
dmrg parm_file.in.xml
```

Listing 9: Convert parameter file to *xml*. Push input file to dmrg program

Listing 11 is a simple python program that creates 21 separate input files. Each input file is further broken down into a series of task files, one for each parameter configuration. This program spans the parameter spaces of the rung couplings (*Jxy1* and *Jz1*) as well as the $S^z$ quantum number space.

ALPS provides a simple function, `pyalps.writeInputFiles('prefix',python_list)`, that converts python lists containing the parameter sets to *xml* parameter files. As before the DMRG program is called with the parameter files used as arguments in the command.

### B.1.2 Output

The DMRG program packages the output data into a *hdf5* list data structure. Using built in ALPS functions this data is extracted into the python lists. The list data structure is multilayered where each element corresponds to a single run of the DMRG program equating to a parameter set. Similar to the input file assembly functions, ALPS also provides functions to extract the data from the output files. The DMRG outputs the data into *xml* and *hdf5* formats.

Much of the data extraction is done using python programs. Listing 12 shows the function that specifically extracts the eigenstate measurements from the output files. The function also excepts which measurements to be extracted (*what=*) and whether the process is *verbose*. There is an exhaustive list

```
LATTICE="open chain lattice"
SWEEPS=4
MAXSTATES=100
CONSERVED_QUANTUMNUMBERS="Sz"
MODEL="spin", L=10
J=1
MEASURE_AVERAGE[Magnetization]=Sz
{ h=0.0 }
{ h=0.5 }
{ h=1.0 }
{ h=1.5 }
{ h=2.0 }
{ h=2.5 }
{ h=3.0 }
{ h=3.5 }
{ h=4.0 }
{ h=4.5 }
```

Listing 10: Parameter set for multiple runs of DMRG over a range of values.

of data loading functions on the ALPS website. More generally these functions are contained within the ALPS API which contains functions for the running of applications along with the loading and evaluation of data.

Following this simple overview we see the DMRG application is straight forward to implement and use. The results are high-quality, certainly good enough for publication. In addition to this chapter, ALPS also includes a number of tutorials and test scripts/programs to help understand the package and each algorithm. The tutorials can be found on the ALPS website[3].

[3]http://alps.comp-phys.org/mediawiki/index.php/ALPS_2_Tutorials:Overview

```
import pyalps
import numpy as np

# Leg length
L=[100]

# Parameter spaces
coup1=[-5.0,-4.5,-4.0,-3.5,-3.0,-2.5,-2.0,-1.5,-1.0,-0.5,0.0,/
 ↪  0.5,1.0,1.5,2.0,2.5,3.0,3.5,4.0,4.5,5.0]
coup2=[-5.0,-4.5,-4.0,-3.5,-3.0,-2.5,-2.0,-1.5,-1.0,-0.5,0.0,/
 ↪  0.5,1.0,1.5,2.0,2.5,3.0,3.5,4.0,4.5,5.0]
coup3=[0.0,0.5,1.0,2.0]
SZ=[0,1,2]

i=0
ladder_parms = []
for l in L:
        for xy in coup1:
                for z in coup2:
                        for w in coup3:
                                for sz in SZ:
                                        ladder_parms.append({
                                                # lattice parameters
                                                'LATTICE'        : "open ladder",
                                                'L'              : l,
                                                'W'              : 2,
                                                # model parameters
                                                'MODEL'          : "spin",
                                                'local_S'        : 0.5,
                                                'Jxy0'           : 1,
                                                'Jz0'            : w,
                                                'Jxy1'           : xy,
                                                'Jz1'            : z,
                                                'CONSERVED_QUANTUMNUMBERS' : 'Sz',
                                                'Sz_total'       : sz,
                                                # DMRG parameters
                                                'SWEEPS'         : 6,
                                                'MAXSTATES'      : 200,
                                                'NUMBER_EIGENVALUES'    : 3,
                                                'MEASURE_LOCAL[Local magnetization]'    :
                                                 ↪  'Sz',
                                                # Temp. files
                                                'TEMP_DIRECTORY' :
                                                 ↪  '/data/th396/Ladders/TEMP_FILES'
                                        })
                #write the input file and run the simulation
                input_file =
                 ↪  pyalps.writeInputFiles('parms_ladder_100_strong_'+str(i),ladder_parms)
                #res = pyalps.runApplication('dmrg',input_file,writexml=True)
                i+=1
                ladder_parms = []
```

Listing 11: Python program creating a series of input files for the ALPS DMRG program.

```
data=pyalps.loadEigenstateMeasurements(output_files,what=,verbose=)

>>> print data[0][0:2]
  x=[0 1 2]
  y=[-238.94957787 -236.63632793 -236.63076625]
  props={'NUMBER_EIGENVALUES': 3.0, 'MEASURE_LOCAL[Local magnetization]': 'Sz',
   ↪  'local_S': 0.5, 'MAXSTATES': 200.0, 'L': 100.0, 'LATTICE': 'open ladder',
   ↪  'SEED': 326481577.0, 'Jxy1': -5.0, 'Jxy0': 1.0, 'W': 2.0, 'MODEL': 'spin',
   ↪  'Jz1': -1.0, 'Jz0': 0.5, 'TEMP_DIRECTORY':
   ↪  '/data/th396/Ladders/TEMP_FILES', 'observable': 'Energy', 'Sz_total': 0.0,
   ↪  'SWEEPS': 6.0, 'filename':
   ↪  './parms_ladder_100_strong_fullrun_0.task100.out.h5', 'hdf5_path':
   ↪  '/spectrum/results/Energy', 'CONSERVED_QUANTUMNUMBERS': 'Sz'}, x=[0]
  y=[  4.41774968e-13]
  props={'NUMBER_EIGENVALUES': 3.0, 'MEASURE_LOCAL[Local magnetization]': 'Sz',
   ↪  'local_S': 0.5, 'MAXSTATES': 200.0, 'L': 100.0, 'LATTICE': 'open ladder',
   ↪  'SEED': 326481577.0, 'Jxy1': -5.0, 'Jxy0': 1.0, 'W': 2.0, 'MODEL': 'spin',
   ↪  'Jz1': -1.0, 'Jz0': 0.5, 'TEMP_DIRECTORY':
   ↪  '/data/th396/Ladders/TEMP_FILES', 'observable': 'Truncation error',
   ↪  'Sz_total': 0.0, 'SWEEPS': 6.0, 'filename':
   ↪  './parms_ladder_100_strong_fullrun_0.task100.out.h5', 'hdf5_path':
   ↪  '/spectrum/results/Truncation error', 'CONSERVED_QUANTUMNUMBERS': 'Sz'}
```

Listing 12: Example of ALPS output data structure.

# Bibliography


[1] John B. Parkinson and Damian J.J. Farnell. *An Introduction to Quantum Spin Systems*. Springer, 2010.

[2] Thierry Giamarchi. *Quantum Physics in One Dimension*. OXFORD UNIV PR, 2004.

[3] David Griffith. *Introduction to Quantum Mechanics*. Pearson, 2 edition, 2005.

[4] J. J. Sakurai. *Modern Quantum Mechanics*. Addison Wesley Publishing Company, 1994.

[5] Hans Bethe. Zur theorie der metalle. i. eigenwerte und eigenfunktionen der linearen atomkette (english version). *Zeitschrift fur Physik*, 1931.

[6] H. J. Mikeska and W. Pesch. Boundary effects on static spin correlation functions in the isotropicx—y chain at zero temperature. *Zeitschrift für Physik B Condensed Matter*, 26(4):351–353, Dec 1977.

[7] F.D.M. Haldane. Continuum dynamics of the 1-d heisenberg antiferromagnet: Identification with the o(3) nonlinear sigma model. *Physics Letters A*, 93(9):464 – 468, 1983.

[8] D. G. Shelton, A. A. Nersesyan, and A. M. Tsvelik. Antiferromagnetic spin ladders: Crossover between spin s=1/2 and s=1 chains. *Phys. Rev. B*, 53:8521–8532, Apr 1996.

[9] Stephen Blundell. *Magnetism in Condensed Matter*. Oxford University Press, 2001.

[10] P. Lecheminant and E. Orignac. Magnetization and dimerization profiles of the cut two-leg spin ladder. *Phys. Rev. B*, 65:174406, Apr 2002.

[11] Ian Affleck, Tom Kennedy, Elliott H. Lieb, and Hal Tasaki. Valence bond ground states in isotropic quantum antiferromagnets. *Communications in Mathematical Physics*, 115(3):477–528, sep 1988.

[12] Victoria Mazo, Efrat Shimshoni, Chia-Wei Huang, Sam T Carr, and H A Fertig. Helical quantum hall edge modes in bilayer graphene: a realization of quantum spin-ladders. *Physica Scripta*, 2015(T165):014019, 2015.

[13] S.-H. Li, Q.-Q. Shi, M. T. Batchelor, and H.-Q. Zhou. Groundstate fidelity phase diagram of the fully anisotropic two-leg spin-1/2 XXZ ladder. *ArXiv e-prints*, April 2017.

[14] Huan-Qiang Zhou and John Paul Barjaktarevi. Fidelity and quantum phase transitions. *Journal of Physics A: Mathematical and Theoretical*, 41(41):412001, 2008.

[15] Keigo Hijii, Atsuhiro Kitazawa, and Kiyohide Nomura. Phase diagram of S = $\frac{1}{2}$ two-leg $xxz$ spin-ladder systems. *Phys. Rev. B*, 72:014449, Jul 2005.

[16] F. B. Ramos and J. C. Xavier. $n$-leg spin-$s$ heisenberg ladders: A density-matrix renormalization group study. *Phys. Rev. B*, 89:094424, Mar 2014.

[17] D. Sénéchal. Semiclassical description of spin ladders. *Phys. Rev. B*, 52:15319–15326, Dec 1995.

[18] Germn Sierra. The nonlinear sigma model and spin ladders. *Journal of Physics A: Mathematical and General*, 29(12):3299, 1996.

[19] T. Barnes, E. Dagotto, J. Riera, and E. S. Swanson. Excitation spectrum of heisenberg spin ladders. *Phys. Rev. B*, 47:3196–3203, Feb 1993.

[20] Elbio Dagotto and T. M. Rice. Surprises on the way from one- to two-dimensional quantum magnets: The ladder materials. *Science*, 271(5249):618–623, 1996.

[21] T. Nagata, M. Uehara, J. Goto, N. Komiya, J. Akimitsu, N. Motoyama, H. Eisaki, S. Uchida, H. Takahashi, T. Nakanishi, and N. Mri. Superconductivity in the ladder compound sr2.5ca11.5cu24o41 (single crystal). *Physica C: Superconductivity*, 282:153 – 156, 1997.

[22] D. Schmidiger, P. Bouillot, S. Mühlbauer, S. Gvasaliya, C. Kollath, T. Giamarchi, and A. Zheludev. Spectral and thermodynamic properties of a strong-leg quantum spin ladder. *Phys. Rev. Lett.*, 108:167201, Apr 2012.

[23] Steven R. White. Density matrix formulation for quantum renormalization groups. *Phys. Rev. Lett.*, 69:2863–2866, Nov 1992.

[24] Kenneth G. Wilson. The renormalization group: Critical phenomena and the kondo problem. *Rev. Mod. Phys.*, 47:773–840, Oct 1975.

[25] A. L. Malvezzi. An Introduction to Numerical Methods in Low-Dimensional Quantum Systems. *Brazilian Journal of Physics*, 33:55–72, March 2003.

[26] Tai-Kai Ng, Shaojin Qin, and Zhao-Bin Su. Density-matrix renormalization-group study of s=1/2 heisenberg spin chains: Friedel oscillations and marginal system-size effects. *Phys. Rev. B*, 54:9854–9861, Oct 1996.

[27] Hans-Jürgen Mikeska and Alexei K. Kolezhuk. *One-dimensional magnetism*, pages 1–83. Springer Berlin Heidelberg, Berlin, Heidelberg, 2004.

[28] T. Nassar and O. Tirkkonen. Excited states in the twisted XXZ spin chain. *Journal of Physics A Mathematical General*, 31:9983–9996, December 1998.

[29] A V Razumov and Yu G Stroganov. Spin chains and combinatorics: twisted boundary conditions. *Journal of Physics A: Mathematical and General*, 34(26):5335, 2001.

[30] Jacques Des Cloizeaux and Michel Gaudin. Anisotropic linear magnetic chain. *Journal of Mathematical Physics*, 7(8):1384–1400, 1966.

[31] Neil W. Ashcroft and N. Mermin. *Solid State Physics*. Cengage Learning, Inc, 1976.

[32] Kazuo Hida. Haldane gap in the spin-1/2 double chain heisenberg antiferromagnet -numerical diagonalization and projector monte carlo study-. *Journal of the Physical Society of Japan*, 60(4):1347–1354, 1991.

[33] Kazuo Hida. Density matrix renormalization group study of the spin 1/2 heisenberg ladder with antiferromagnetic legs and ferromagnetic rungs. *Journal of the Physical Society of Japan*, 64(12):4896–4900, 1995.

[34] Hiroshi Watanabe. Numerical diagonalization study of an s=1/2 ladder model with open boundary conditions. *Phys. Rev. B*, 50:13442–13448, Nov 1994.

[35] Ian Affleck, Tom Kennedy, Elliott H. Lieb, and Hal Tasaki. Rigorous results on valence-bond ground states in antiferromagnets. *Phys. Rev. Lett.*, 59:799–802, Aug 1987.

[36] Steven R. White. Equivalence of the antiferromagnetic heisenberg ladder to a single s=1 chain. *Phys. Rev. B*, 53:52–55, Jan 1996.

[37] Eugene H. Kim, G. Fáth, J. Sólyom, and D. J. Scalapino. Phase transitions between topologically distinct gapped phases in isotropic spin ladders. *Phys. Rev. B*, 62:14965–14974, Dec 2000.

[38] Daniel Loss Sergey Bravyi, David DiVincenzo. Schrieffer - Wolff transformation for quantum many-body systems. *Annals of Physics*, 326(10):2793–2826, October 2011.

[39] Jens Koch. *Quantum transport through single-molecule devices*. PhD thesis, Freie Universit at Berlin, 2006. Appendix.

[40] Prof. Paul Parris. Lecture notes on angular momentum and rotations. `http://web.mst.edu/~parris/QuantumTwo/Class_Notes/AngularMomentum.pdf`, 2014.

[41] N. Nagaosa. *Quantum Field Theory in Strongly Correlated Electronic Systems*. Springer, 1998.

[42] Ben Simons. Lecture notes on quantum magnetism. `www.tcm.phy.cam.ac.uk/~bds10/tp3.html`, 2005.